TECHNISCHE UNIVERSITÄT DARMSTADT
Physik

Monitoring physiological changes in cells after ionizing radiation using fluorescence lifetime imaging by time resolved single photon counting

Untersuchung physiologischer Veränderungen in Zellen nach ionisierender Strahlung mittels Fluoreszenz-Lebensdauer-Mikroskopie basierend auf zeitaufgelöster Einzelphotonenmessung

Vom Fachbereich Physik
der Technischen Universität Darmstadt

Zur Erlangung des Grades
eines Doktors der Naturwissenschaften
(Dr.rer.nat.)
genehmigte Dissertation von
MSc.-Phys. Elham Abdollahi Mirzanagh aus London

Referent: Prof. Dr. Marco Durante
Korreferent: Prof. Dr. Barbara Drossel

Tag der Einreichung:17.07.2017
Tag der Prüfung:16.10.2017

Darmstadt 2017
D 17

Monitoring physiological changes in cells after ionizing radiation using fluorescence lifetime imaging by time resolved single photon counting

Untersuchung physiologischer Veränderungen in Zellen nach ionisierender Strahlung mittels Fluoreszenz-Lebensdauer-Mikroskopie basierend auf zeitaufgelöster Einzelphotonenmessung

Zur Erlangung des Grades eines Doktors der Naturwissenschaften (Dr. rer. nat) vorgelegte Dissertation von Elham Abdollahi Mirzanagh aus London

1. Gutachten: Prof. Dr. Marco Durante
2. Gutachten: Prof. Dr. Barbara Drossel

Tag der Einreichung: 17.07.2017
Tag der Prüfung: 16.10.2017

Darmstadt- D 17

Declaration of Scientific authorship

I hereby declare that this doctoral thesis contains the results of my research carried out at GSI Helmholzzentrum für Schwerionenforschung GmbH in Darmstadt. Excluding an introductory part the research described in this thesis is original unless an explicit reference is made to work of others. This thesis has not been submitted for any qualification other than the degree Dr. rer. nat. at the Technical University of Darmstadt.

Darmstadt,

.....
Elham Abdollahi Mirzanagh

Abstract

Eukaryotic DNA is packed with histone and non-histone proteins into chromatin fibers. The higher order structure of the chromatin comprises loosely packed euchromatin and more densely packed heterochromatin. Euchromatin mainly consists of active gene regions, whereas repressive DNA is mainly included in heterochromatin. Remodeling of the local chromatin structure is critical for the regulation of gene expression and replication of the DNA, but also for repair, if DNA lesions are induced into chromatin. Exposure of the DNA to chemicals or ionizing radiation as well as natural processes can lead to an interruption of its integrity resulting in the formation of double strand breaks, an especially critical type of DNA damage. The inappropriate repair of double strand breaks may lead to genomic instability and finally to the development of cancer. To get further insight into the maintenance of genomic stability, the understanding of cellular responses to double strand breaks is highly required. The chromatin structure and its dynamics are suspected of playing a significant role in the regulation and facilitation of DNA repair.

The main aim of this thesis has been to establish a chromatin compaction assay which is working in living mammalian cells and can be easily applied to different cell lines without the necessity of using genetic modifications. The major biological goal was to provide additional and independent evidence of a radiation-induced chromatin decondensation exceeding the hitherto proof based on fluorescence depletion. In addition other potential biological applications of the compaction assay should be explored. To achieve these aims, time correlated single photon counting fluorescence lifetime imaging microscopy (FLIM) was inspected and characterized in combination with different organic DNA dyes or fluorescent proteins, which might serve as chromatin compaction sensors. To test the irradiation response, the FLIM setup could be coupled to a beamline microscope or, alternatively combined with a 35 kV X-rays tube. The findings demonstrate that some single organic DNA binding dyes revealed a high dynamic range of chromatin compaction with respect to fluorescent histone FRET pairs. These newly established chromatin compaction probes were capable of detecting structural changes of chromatin induced via enzymatic treatments as well as osmolality changes. Furthermore, using postirradiative fixation, the exposure of murine cells to ion irradiation revealed a significant local enhancement of the lifetime values of dyes like Hoechst 34580 at sites of heterochromatic ion traversals, implying a local radiation- chromatin relaxation. Additionally, a global chromatin decompaction after X-rays irradiation could be detected in living cells proving the applicability of this approach as a live cell assay. Besides radiation induced changes, using the small differences in chromatin densities in different cell cycle phases or in resting versus cycling cells could be shown, demonstrating that the established FLIM-based chromatin compaction assay can also successfully applied to other questions or fields in biological research.

Zusammenfassung

Eukariotische DNA wird mit Hilfe von Histon- und nicht-Histon Proteinen in Chromatin verpackt. Die höher geordnete Chromatinstruktur lässt sich in ehr locker gepacktes Euchromatin und dichter gepacktes Heterochromatin unterteilen. Während das Euchromatin hauptsächlich die aktiv transkribierten Gene beinhaltet, ist die stillgelegte DNA mehr dem Heterochromatin zuzuordnen. Die Regulation der Genexpression und der Replikation der DNA erfordert eine Remodellierung beziehungsweise Öffnung der Chromatinstruktur, deren Notwendigkeit auch für eine Reparatur, die nach der Induktion von DNA Schäden auftritt, postuliert wird. Diese DNA Schäden können durch die Einwirkung von Chemikalien oder ionisierender Bestrahlung, aber auch durch endogene metabolische Prozesse erzeugt werden. Als besonders kritisch wird dabei der DNA Doppelstrangbruch (DSB) angesehen, da dieser die Integrität des Chromatins zerstört. Eine unsachgemäße Reparatur von DSBs kann zu genomischer Instabilität führen und, letzten Endes, zur Krebsentstehung beitragen. Um einen tiefergehenden Einblick in den Erhalt der genomischen Stabilität zu erlangen ist es deshalb nötig die zellulären Antworten auf Doppelstrangbrüche zu verstehen. Die Chromatinstruktur und -dynamik spielt dabei eine wesentliche Rolle in der Regulation und Förderung der Reparatur.

Das Hauptziel der vorliegenden Arbeit war es einen Assay zu etablieren, der es erlauben sollte die Chromatinkompaktierung in lebenden Säugerzellen zu messen. Zudem sollte er sich ohne großen Aufwand auf unterschiedliche Zellllinien übertragen lassen indem er die Notwendigkeit gentechnischer Veränderung vermeidet. Die Hauptanwendung bestand darin, unabhägige Beweise für das Auftreten strahlungsinduzierter Chromatindekondensation zu erhalten, die über die bisherigen, fluoreszenzintensitätsbasierten Messungen hinausgingen. Zusätzlich sollten alternative biologische Anwendungen des Kompaktierungs-Assays getestet werden. Um diese Ziele zu erreichen wurde die Methode der Fluoreszenzlebensdauermikroskopie (FLIM) basierend auf zeitkorrelierten Einzelphotonenmessungen untersucht und in Verbindung mit verschiedenen organischen DNA Farbstoffen oder fluoreszierenden Proteinen, die als Chromatinkompaktierungssensoren dienen sollten, charakterisiert. Um strahlungsbedingte Veränderungen messen zu können, kann der FLIM Aufbau wahlweise an das Strahlplatzmikroskop oder an eine 35kV Röntgenanlage angeschlossen werden. Die gewonnenen Ergebnisse zeigen, dass einige der organischen DNA Farbstoffe im Vergleich zu Histon-FRET Paaren einen höheren dynamischen Umfang der Lebensdauerantwort auf Chromatinveränderungen aufweisen. Die neuetablierten Chromatinkompaktierungssensoren sind in der Lage enzymatisch oder osmotisch induzierte Chromatinstrukturveränderungen anzuzeigen. Darüber hinaus konnte in Mäusezellen, die nach der Bestrahlung fixiert wurden, nach Ionenbestrahlung eine lokal signifikant erhöhte Fluoreszenzlebensdauer von Sensoren wie Hoechst34580 am Ort heterochromatischer Ionendurchgänge gezeigt werden. Neben dieser lokalen Chromatindekondensation konnte nach Röntgenbestrahlung eine globale Dekompaktierung in lebenden Zellen nachgewiesen und damit die Anwendbarkeit für Lebendzelluntersuchungen demonstriert

werden. Neben strahlungsabhängigen Veränderungen konnten Unterschiede in der Chromatindichte in unterschiedlichen Zellzyklusphasen und ruhenden Zellen gezeigt werden. Die Ergebnisse belegen, dass der hier etablierte FLIM basierte Chromatinkompaktierungs-Assay auch erfolgreich für andere biologische Fragestellungen verwendet werden kann.

1. Table of Contents

Publication related to this work

Peer-reviewd article

E. Abdollahi, G. Taucher-Scholz, M. Durante and B. Jakob. Upgrading the GSI beamline microscope with a confocal fluorescence lifetime scanner to monitor charged particle induced chromatin decondensation in living cells. NIMB,365 (2015) 626-630.

Scientific reports

E. Abdollahi, L. Pack, G. Taucher-Scholz, B. Jakob. Inspection of counting loss and pile up effect on fluorescence lifetime recording of radiation-induced chromatin decompaction. GSI Scientific Report, 2017 (in press).

E. Abdollahi, N. Özgün-Korkusuz, M. Durante, G. Taucher-Scholz and B. Jakob. Repositioning and targeting irradiation of offline preselected single decondensation measurements using the heavy ion microprobe. GSI Scientific Report, 2016.

E. Abdollahi, N. Özgün-Korkusuz, M. Durante, G. Taucher-Scholz and B. Jakob. Detection of chromatin decondensation induced by charged particle irradiation using Fluorescence Lifetime Imaging Microscopy. GSI Scientific Report, 2015.

2. Introduction

Research over the past decade has demonstrated that chromosome territories are divided into different domains in which chromosomal compaction levels are correlated to the functional activities (1; 2; 3; 4). These differences in functional activity and compaction are associated with different designation as transcriptionally active and inactive domains or euchromatin (decondensed) and heterochromatin (HC) (tightly packed), respectively (5; 6).

DNA damage and especially DNA- double starnd breaks (DSBs), which can be induced by exogenous agents like ionizing radiation, can threaten the genomic integrity/stability and may ultimately lead to cancer formation, if they are not repaired correctly (7; 8; 9). Since human beings are frequently exposed to environmental or medical radiation, understanding the cellular response to ionizing radiation is critical in radiation biology. As mentioned, DSBs are the most deleterious lesions for human health which introduce a real challenge for repair mechanisms (10). DSB repair might be even more challenging for complex DSBs as produced by high linear energy transfer (LET) radiation such as heavy ions, which produce more critical DNA damages with respect to low LET irradiation (11).

Nowadays, a major aim of current research in biophysics is to understand the potential interaction of nuclear structure and function in order to clarify the mechanistic principles behind spatial organization of chromatin and chromatin rearrangements during intra nuclear processes like DNA repair after exposure to ionizing radiation. Overal, the identification of how cells repair DSBs in the context of chromatin organization are crucial to understand not only the development of cancer but also for improved strategies of cancer therapy (10; 11; 12).

Online microscopy in combination with ion irradiation provides a useful tool to investigate fast biological dynamics since it can be operated without delay and cumbersome repositioning. It has been demonstrated that compacted heterochromatin provides a challenge for the cellular DSB repair system, particularly in combination with the induction of complex lesions or locally multiple damage sites as originate from charged particle irradiation (13; 14; 15). However, the exposure of cells to ionizing radiation revealed a local chromatin decondensation in heterochromatin compartments at sites of ion traversals (9).

Using different radiation qualities, a number of recent studies have addressed the chromatin decompaction which is accompanied by damage relocation to the heterochromatic/euchromatin interface for further processing. Both might have an important impact on the following repair process, as it might be necessary to open up the space for subsequent recruitment of further repair factors (9; 16; 17; 18; 19; 20). However, the DSB movement and its correlation to the radiation-induced chromatin decompaction are unclear. It was speculated that the local decompaction originates in an alternation of the balance of physical forces leading to a driving force for the observed relocation of the heterochromatin damage (9; 18). Attempts undertaken to measure the dynamics of the chromatin decondensation in living mouse cells based on the drop in the intensity of the live-cell DNA- labeled fluorophore revealed a time course of seconds to minutes post-irradiation. The duration of this radiation-induced DNA decondensation point to a (yet undefined) biological process different from a direct radiation induced physico-chemical modification of the molecular structure of the DNA (9; 18). However, in contrast to a robust observation of a local ion induced depletion in DNA staining, intensity based

chromatin decondensation measurements in living cells suffer from only moderate irradiation induced changes. In addition staining variability and the intrinsic problem of discrimination between chromatin decondensation and a reduction of available dye binding sites impede a quantitative analysis. Thus, a more sensitive readout, which is functional in living cells, but independent of the intensity information, is highly desirable.

Advances in the conjugation of fluorescent molecules to antibodies allowed fluorescence to be used for microscopic imaging, providing specific labeling ability and improved signal to background ratio over prior staining methods (21). Many biologically related disciplines rely on the application of specific fluorescent probes which offer a powerful tool to image biological materials and to observe the structure and dynamics of nucleic acids, proteins and other biological micromolecules (22). The characteristics of fluorescence microscopy such as single molecule sensitivity, sub-micron resolution and real-time data collection make it an enabling tool to study either the structure of the sample or the observation of dynamics and functions (23; 24). A few remarkable application are the study of neuronal activity using calcium-sensitive fluorescent dyes (25), intracellular monitoring utilizing fluorescent timers (26), membrane dynamics with fluorescence recovery after photobleaching (FRAP) (27) and biological interactions on small scale via recording the co-localization of molecules through ratiometric fluorescence resonance energy transfer (FRET) (28).

There are several factors that can offer a challenge to capture high quality fluorescence images. For instance: fluctuation in fluorophore concentration within the sample, light soure limitation and filter requirements for excitation, fluorophore photobleaching, autofluorescence, detector sensitivity limits, sample prepration requirements and optical time resolution (29; 30). Various techniques can be utilized to address some of these challenges. Fluorescence lifetime imaging microscopy (FLIM) is one of the fluorescence microscopy techniques that address a subset of aforementioned challenges. FLIM is capable of addressing some of the limitations of fluorescence microscopy that are associated with fluorophore intensity fluctuation, autofluorescence, background (31) and less susceptible to artifact originating from scatter light, photobleaching, non-uniform illumination of the sample, or variations of excitation intensity (24). Image contrast in FLIM is relying on the temporal response of a fluorophore to an excitation source (32). Fluorescence lifetimes can be measuresd either in the time domain using a pulsed laser excitation source and measuring the fluorescence intensity decay over time, or in the frequency domain utilizing modulated continuous wave (CW) excitation source. In time domain, the intensity decay is typically measured employing either a gated-integration technique or time correlated single photon counting (TCSPC). Among distinct fluorescence microscopy techniques, FLIM serves as a promising method to image the local microenvironment and interaction of explicit probes in living cells through monitoring shifts in the measured fluorescence lifetime, which are associated with changes in properties like pH (33), charge concentration (34), metabolic state (35; 36), protein-proteins interaction (37) or chromatin condensation (38). Besides the application of FLIM in biological sciences, FLIM has found potential applications in medicine (39; 40; 41; 42). Various FLIM applications have been described in the review paper of Borest (43). The following sections present a brief overview of radiation biophysics as well as fluorescence lifetime imaging microscopy.

2.1. Radiation biophysics

2.1.1. Biological impact of ionizing radiation

Ionizing radiation is a form of radiation that carries sufficient energy to interact with an atom or molecule and transfers enough energy to release an electron, which gives rise to ionization of the atom. Ionizing radiation can be categorized into: (i) sparsely ionizing radiation, e.g. photon irradiation like X-rays or gamma rays and (ii) densely ionizing radiation, e.g. particle irradiation like neutrons, alpha particles or heavy ions. The absorbed dose corresponds to the mean energy imparted to matter per unit mass by ionizing radiation (given in the units of Gray (Gy)), and can be expressed by (44)

$$D=\Delta E_{abs}/\Delta m, \qquad (1.\ 1)$$

where ΔE_{abs} is defined as the mean absorbed energy in a matter of the mass Δm. The dose distribution of sparsley ionizing radiation is evenly distributed on a macroscopic scale, whereas the dose distribution steeply drops from the center of the ion track and is indirect propotional to the square root of the radius ($1/r^2$) in densely ionizing radiation. As seen in Figure 1, for the same applied dose, the dose distribution pattern varies for photons and charged particles. For the ions, the spreading of dose around the trajectories (and the maximal radius) depends on the specific energy. The specific energy not only defines the radial extension of the dose deposition, but also the path length of the ion in matter.

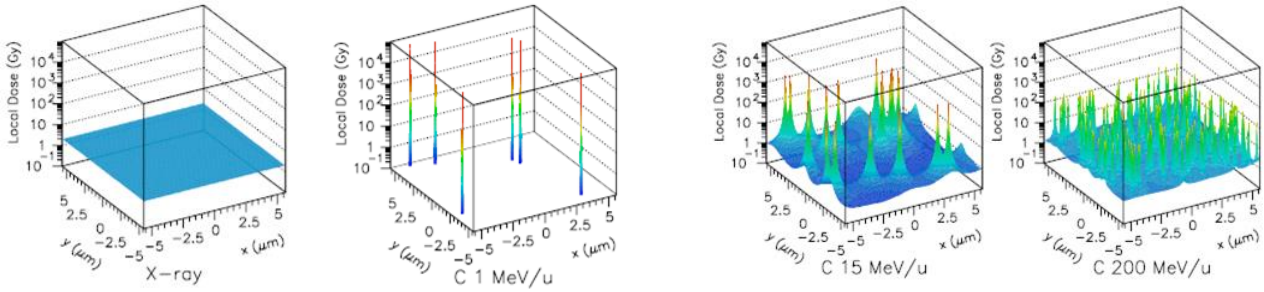

Figure 1. Illustration of the variety of microscopic dose distribution by X-rays and carbon ions with different energies. A mean dose of 2 Gy is deposited in each scheme. A homogenous dose distribution can be seen by X-rays, whereas carbon ions deposit energy locally around the ion track. The dose maximum reduces with raising energy and a higher fluence of the particle is required to acheive the same dose of 2 Gy at higher energies (Figure is reproduced from (45)).

For higher energetic charged particles, many interactions are needed to stop the particle. Each interaction leads to a deposition of energy and decrease in the velocity of the particle. The most relevant interaction processes is the electronic stopping through inelastic Coulomb interactions with the surrounding atoms

giving rise to the production of secondary electrons. Moreover, most of these electrons possess rather low energy which leads to further interactions within a few nanometers surrrounding the primary ion, in turn, creates a highly localized dose deposition along the ion track. The deposited energy (E) per path length (x) (the linear energy transfer (LET)) is described by the Bethe-Bloch fomula and is proportional to square of the effective charge Z_{eff} of the particle

$$LET=dE/dx \propto (1/\beta^2).\ Z_{eff}^2, \qquad (1.\ 2)$$

where β given by v/c represents the relativistic velocity of the particle. According to this formula, the interactions depend on the velocity of the particle. The energy loss is comparably low at high energies and thus velocities. There is a conversion of LET to the macroscopic dose by the particle fluence given by (45)

$$D = 1.602.\ 10^{-9}.\ LET.\ F.\ 1/\rho, \qquad (1.\ 3)$$

where D represents dose (given in units of Gy). LET refers to the linear energy transfer and is given in the units of keV/μm; the fluence (F) is given in units of cm^{-2}. ρ is the density of the target material (g/cm^3). Note, since biological materials such as cells or tissue are mostly composed of water, the density of water is typically used for the calculation.

Research over the past years has demonstrated that the ionization process is able to break covalent bonds and disintegrate a moclecule such as DNA, in turn, leading to create critical biological damage. As stated, the cells mostly are composed of water which gives rise to the production of highly reactive free radicals through a radiative dissociation of water molecule. Free radical species and hydrated electrons are subjected to further reactions with each other and molecules creating a large variety of radical species and byproducts with a longer lifetime like H_2O_2 that can possibly damage DNA. Further, the produced ions and electrons can lead to subsequent interaction process and create further damage.

DNA in eukaryotic is well organized and is associated with histone proteins building a highly structured nucleoprotein complex called chromatin. Chromatin structure and DNA packing regulate a number of vital cellular processes like cell division, transcription, differentiation and DNA repair (46). Chromatin possesses a variable packing density which can be catagorized into two main groups. These included, the densaly packed heterochromatin (the low gene density) and the more open which is transcriptionally active called euchromatin (47). Modifications in the packing density like acetylation, phosporylation or methylation lead to recruitment of chromatin remodeling enzymes that act in nucleosome sliding, ejection and restructuring to regulate chromatin condensation and decondensation (48). Phosphorylation of the histone H2AX at serin 139 generates ϒH2AX that is one of the well known radiation induced chromatin modifications (49). ϒH2AX serves as a reliable DSB marker and functions in the recruitment of repair proteins and checkpoint control (50). Upon radiation-induced DSBs, methylation and acetylation also give rise to alternation in the chromatin structure. A local relaxation of the chromatin after radiation- induced DSBs is the most intense structural

changes of chromatin that was observed and speculated to facilate recruitment and binding of repair factors (9; 18; 51; 52).

The work of this thesis has been aimed to establish a FLIM-based chromatin compaction assay with the main goal to monitor radiation-induced chromatin decompaction in living cells. In addition, the chromatin compaction assay was applied to additional biological questions like the chromatin status during the cell cycle. Following this general introduction, briefly, the theory behind the method of fluorescence lifetime imaging microscopy will be explained.

2.2. Fluorescence lifetime imaging microscopy (FLIM)

It is known that absorption of a photon leads to promoting one of the weakly bound electrons of a fluorophore to a higher energy level and light is emitted when that electron returns to the ground state. Figure 2 showed a common representation of these transitions by the so-called Jablonski diagram. As seen, the fluorescent molecule is excited by a short wavelength. During the vibrational relaxation and internal conversion (IC) processes the electron loses energy as heat. Inter-system crossing (ISC) to the triplet state T_1 might occur ocasionally but this spin conversion and the electron decay from T_1 to S_0 is quantum-mechanically forbidden. Since each energy state consists of several vibrational energy levels between which the electron can make transition, a range of wavelength can be used to excite an electron. Identically, a spectrum of emission wavelength is associated with each fluorescent molecule. The emission energy generally is lower than the excited energy, in turn; the peak of the emission spectrum is at a longer wavelength than the peak of the absorption spectrum. The separation between emission and absorption peaks is known as the Stokes shift.

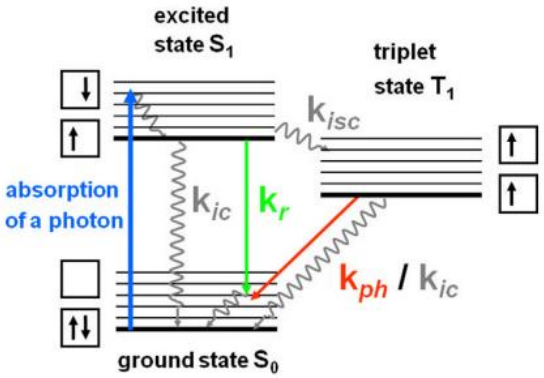

Figure 2. Jablonski diagram represents the energy transitions that can occur within the fluorescent molecule. S_0 and S_1 are the ground state and excited singlet state, respectively. T_1 represents a triplet state. Each state consists of several energy levels which form an energy band. The energy of absorbed and emitted light can be altered based on the energy differences between the levels and creates a spectrum for both excitation and emission. An excited electron can return to the ground state through a number of pathways, containing vibrational relaxation (VR), inter-system crossing (ISC), and internal conversion (IC) or by emitting a photon (r, ph) (Figure is reproduced from (53)).

Besides to the fluorescence intensity, information about the fluorophore can be obtained from the rates associated wih the electron transitions shown in Figure 2. The initial vibrational relaxation process occurs on the order of picoseconds.When the electron reaches the lowest energy level in S_1 which is a metastable state; it decays to S_0 and emits a photon. The fluorescence lifetime (τ) is the average time (in a range of nanoseconds) a fluorophore remains in the electronically excited state (S_1) and can be expressed by (54)

$$\tau = 1/ (k_r + k_{nr}) \qquad (1.4)$$

where k_r is the radiative rate constant giving rise to fluorescence whereas k_{nr} represents the non-radiative rate constant given by the sum of alternative decay channels, $k_{nr} = k_{isc} + k_{ic}$. k_{isc} and k_{ic} represent inter-system crossing and internal conversion rates, respectively. If an electron undergoes a spin conversion to reach the triplet state, T_1, then it can endure in that excited state for milliseconds or longer. Photon emission from the triplet state to the ground singlet state is called phosphorescence which typically occurs at longer wavelength than the fluorescence (31). Most fluorescent molecules show a mono-exponential decay once measured for a given environmental condition. However, many applicants of fluorescence lifetime will inherently have fluorescence species other than the one being of interest. Thus, typical intensity decay for a population of fluorophores will comprise a multi-exponential decay of the form

$$I(t) = I_0 + A_0 e^{-t/\tau_0} + A_1 e^{-t/\tau_1} + \ldots \qquad (1.5)$$

In FLIM the fluorescence lifetime is measured besides the fluorescence intensity (54; 55; 56). Although a fluorophore's lifetime is an intrinsic property of the molecule, it can be affected by external factors that influence its emission rate constant (Eq. (1.4)). Hence, lifetime measurements can be utilized to investigate changes in the microenvironment surrounding a fluorophore. This property makes fluorescence lifetime a powerful technique to direct *in vivo* sensing of alternation in pH because of interaction with hydrogen ions (57), gradient of intercellular viscosity (58), temperature measurement (59; 60; 61), Ca^{2+} imaging (62), and presence of other micromolecules (63). Furthermore, FLIM-FRET measurements provide information of physical protein-protein interactions. FLIM can be used to observe *in vivo* metabolic states. Lifetime imaging has the potential to provide early identification of cancers by distinguishing metabolic states and the favoured metabolic pathway which is known to shift from oxidative phosphorylation to glycolysis during tumor progression (64). FLIM enables monitoring proliferation and cell cycle progression in a cell cycle assay (65). Another example of application is that FLIM can provide a detailed quantitative analysis of all chromosomes in a mamlian cell (66) as well as information of compacted regions of chromatin (38; 66). Due to the fact that FLIM measured the lifetime of a fluorochrome in the order of few nano-seconds, most of the conventional instrumentation used for steady state fluorescence microscopy cannot be utilized (67). Considering these few examples, it is obvious why FLIM has been regarded as a powerful technique.

2.2.1. Modulation of fluorescence lifetime

As mentioned, FRET is the process by which excitation energy of one fluorophore is transferred to a nearby second fluorophore as a result of long-range electrical dipole-dipole interactions between fluorophores. There are different approaches to measure FRET. These include: sensitized emission, photobleaching rate, and fluorescence lifetime changes. In intenstiy-based approaches, the spectral contaminations between the fluorophores due to their broad fluorescence spectra in combination with the nessecity for a significant spectra overlap potentially give rise to errors. Moreover, quantification of FRET in these approaches relies on the concenetration of the fluorophores. However, approches that inspect the changes in the depopulation rates of the excited states of donor fluorophores are capable of providing highly quantitative and robust measurements (54). The FLIM-FRET approach is briefly described in the following.

In FLIM-FRET measurements (Figure 3), the lifetime of the donor is shortened because of the presence of a quenching molecule within the Förster radius. It has been reported that collisional quenching or FRET could have a significant impact on reduction of the lifetime. The rate constants of this process in the terms of the lifetimes can be expressed by (54)

$$\tau_D = 1/\ (k_r+k_{nr}) > \tau_{DA} = 1/\ (k_r+k_{nr}+k_T), \qquad (1.\ 6)$$

where τ_D and τ_{DA} are the lifetimes of donor in the absence and presence of the acceptor, respectively. k_T is the rate of FRET. A strong overlap between the donor emission spectrum and the absorption spectrum of the quencher molecule (acceptor) is one important factor. The excited electron from the donor is directly transferred to the acceptor through a dipole interaction. Since the mechnism of electron transfer is based on dipole interactions, the Förster radius is in the order of only several nanometers.

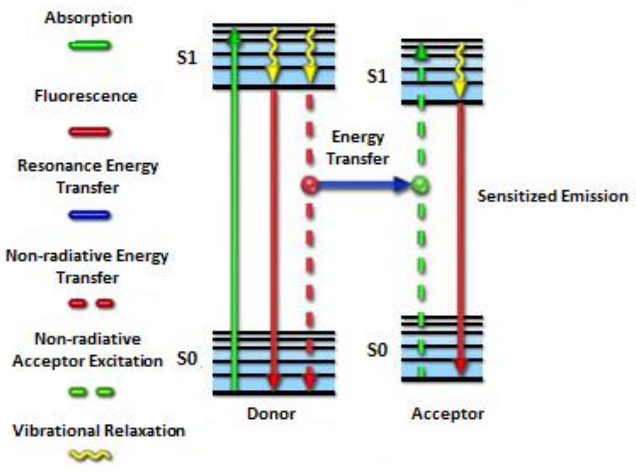

Figure 3. Jablonski diagram representing energy transfer between donor and acceptor. (Figure is modified from (68)).

The ability of FLIM to image intractions between the fluorophores and other molecules is interesting for *in vivo* studies. In addition, FRET is a common tool for detecing binding of molecules (63; 69), conformational changes (70). Furthermore, the close proximity of the donor and acceptor plays a fundamental role in the efficacy of the resonance transfer as it decreases by 1 over the distance to the power of 6. The Föster equation is given by (24)

$$E_{FRET} = R_0^6/(R_0^6+r^6), \qquad (1.\ 7)$$

where R_0 represents Föster distance, i. e. the separation distance between donor and acceptor at which the efficiencey of energy transfer is 50 % (R_0=r). r is the donor and acceptor separation distance. The FRET efficiency (E) can also be expressed by comparing the fluorescence lifetime in absence or presence of the acceptor (24)

$$E=1-\tau_{DA}/\tau_D. \qquad (1.\ 8)$$

Moreover, the orientation of dipoles was observed to be as critical factor for FRET coupling. Figure 4 depicted the aforementioned criteria of FRET in which schematically illusterated by FRET couple eGFP (enhanced green fluorescence protein) as donor and mCherry as acceptor in panel (a), (b) and (c), respectively.

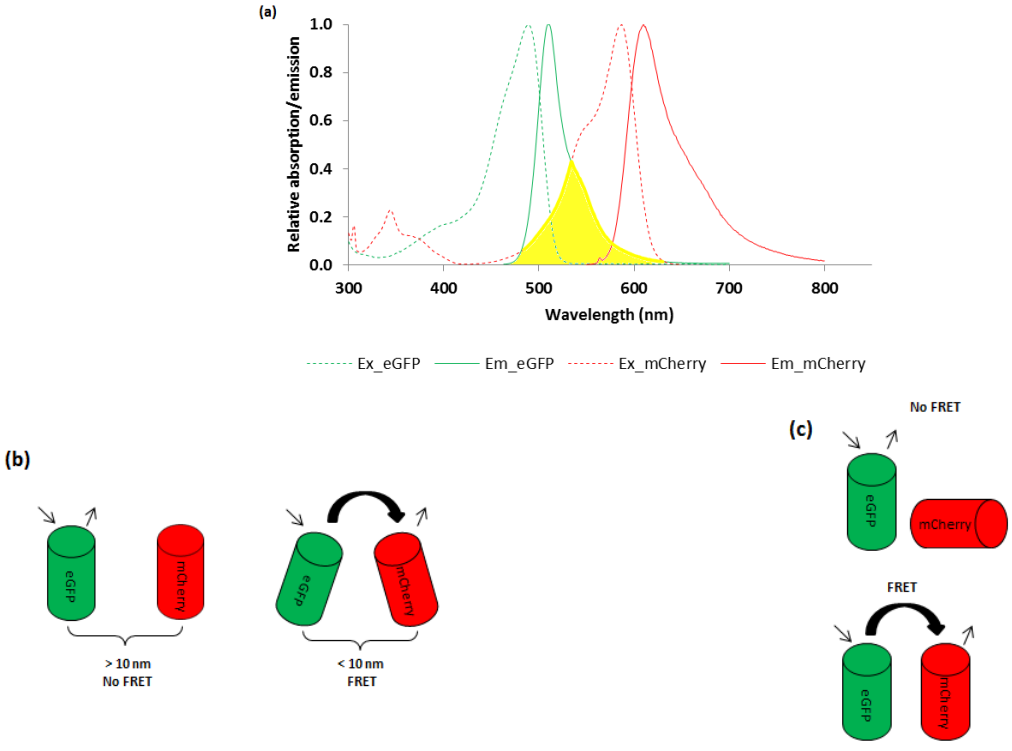

Figure 4. Schematic illustration of different criteria to support FRET. (Spectra (a) were ploted from Tsien labratory, (b) and (c) are reproduced from (71)).

2.2.2. Operation Principles of FLIM

The FLIM technique can be operated either in the frequency or time domain (24; 54; 67). Both methods yield mainly the same information and vary essentially in how the time resolved fluorescence data are acquired (43). In the following, the methods for measuring fluorescence lifetime and the challenges associated with lifetime measurements are briefly discussed.

- Frequency- domain lifetime measurements:

Frequency domain (FD) FLIM technique exploits an intensity modulated light source and measures the temporal response of the fluorescence signal. The amplitude and phase shift of the measured fluorescence signal relative to the modulated source will rely on the lifetime of the fluorophore and the period of the modulated light source. In principle, the excitation light is sinusoidally modulated. Consequencely, the fluorescence signal also appears to be sinusoidally modulated with the same frequency. However, the fluorescence signal is affected by a phase shift and a decrease in modulation depth (Figure 5).

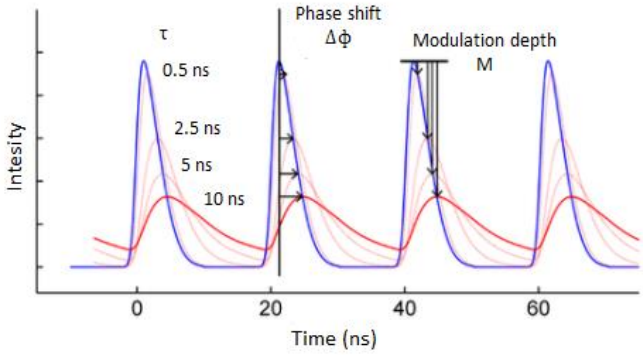

Figure 5. A schematic illustration of FD FLIM. The fluorescence lifetime is derived from the reduction in the modulation degree and the phase shift of the fluorescence with respect to the excitation. The excited light is shown by blue curve and the red curves represent fluorescence emissions (Figure is reproduced from (72)).

With this approach, to extract the phase shift and modulation depth from the fluorescence signal, a homodyne detection method is often employed. The sensitivity of the detector is modulated with the same frequency as the excitation. By shifting the phase of the detector sensitivity with respect to that of the excitation and acquiring images at each phase step, the phase shift ($\Delta\phi$) and the modulation depth (M) can be calculated for each pixel of the image. The phase fluorescence lifetime (τ_p) and the modulation fluorescence lifetime (τ_M) can be determined using (31)

$$\tau_p = (1/\omega)\tan(\Delta\phi) \qquad (1.9)$$

and

$$\tau_M = 1/\omega \left(\sqrt{\frac{1}{m^2} - 1}\right) \qquad (1.\ 10)$$

where ω represents the angular frequency of the modulation. Frequency domain FLIM can be performed using various optical and electronic principles, e. g. wide field excitation, a gain modulated image intensifier camera or a gain modulated point detector (56).

- time- domain lifetime measurements:

An alternative approach to measure fluorescence lifetimes is to measure directly the intensity decay employing time-domain techniques.The time domain FLIM can be classified into two primary approaches, time gating and time correlated single photon counting (TCSPC). These approaches vary from FD FLIM in the instrumentation requirements and the type of data that are recorded. All time domain measurements need a sub nanosecond pulse laser that excites a population of fluorophores in the sample. The intensity decay of that population is measured. A precise time measurement of the decay can be challenging since typical biologically relevant fluorescent lifetimes are on the order of several nanoseconds.The details for each of the time domain approaches to lifetime imaging are presented in the following.

In time gating measurement (Figure 6), the photons are counted in a fixed number of discrete time intervals utilizing gated detection. The advantage of this approach is that it can accept multiple photons after a single pulse which allows higher count rates, thus making it faster. Since it does not require least-square fitting, the lifetime calculation is significantly shortened and becomes mathematically simple. This approach is robust and effective for biological imaging and can provide real-time analysis of the average lifetime of a sample (73). The lifetime with two measurement windows of equal width can be determined using (67)

$$\tau = -\Delta t \,/ \ln\,(D_2/D_1), \qquad (1.\ 11)$$

where τ represent the average mean lifetime of a sample. Δt is the time delay between excitation pulse and the start of detection interval. D_1 and D_2 are two contiguous areas of width Δt.

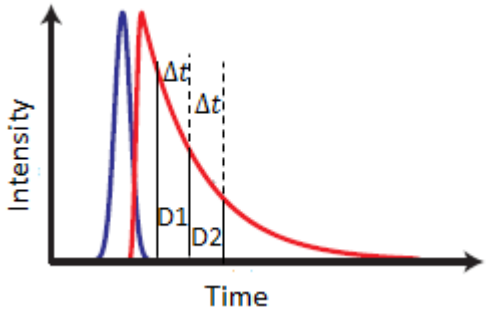

Figure 6. Principle of time-gating FLIM. The fluorescence decay is integrated during two equaly sized time bins. More accurate lifetime measurements can be done by integrating over shorter windows and increasing the number of total windows.

Another technique for time domain lifetime measurements is TCSPC. TCSPC-FLIM approach is widely applied to acquire FLIM images for different biological applications (31; 52; 66; 74; 75; 76). This method measures the time at which individual photons are emitted from the population of fluoropores and extracts the lifetime from the statistical distribution of these events (77). The excited electrons in the fluorophores will return to the ground state with an average time given by its lifetime. Each individual excitation event and corresponding photon emission will give rise to a photon arrival time that is described as a non-homogeneous Poisson process with rate parameter expressed by

$$\lambda(t) = a e^{-t/\tau}, \qquad (1.\ 12)$$

Where λ represents the Poisson rate parameter, a is the intensity of the emission signal and τ is the lifetime of the fluorophore. In principle, after each laser pulse, a single photon emission is deteted and the time interval between laser pulse and detected photon is recorded (Figure 7). By repeating laser pulses a sufficient number of photon arrival times can be collected to rebuild a histogram that corresponds with the distribution given by the non homogenous Poisson process. Then, an exponential decay can be fitted to the histogram from which the lifetime can be estimated. For each pixel in the image, thousands of laser repetitions are accumulated which lead to relative long image collection times compared to time gated FLIM (54; 56; 67; 78). In the study associated with this thesis, FLIM technique based on TCSPC has been performed.

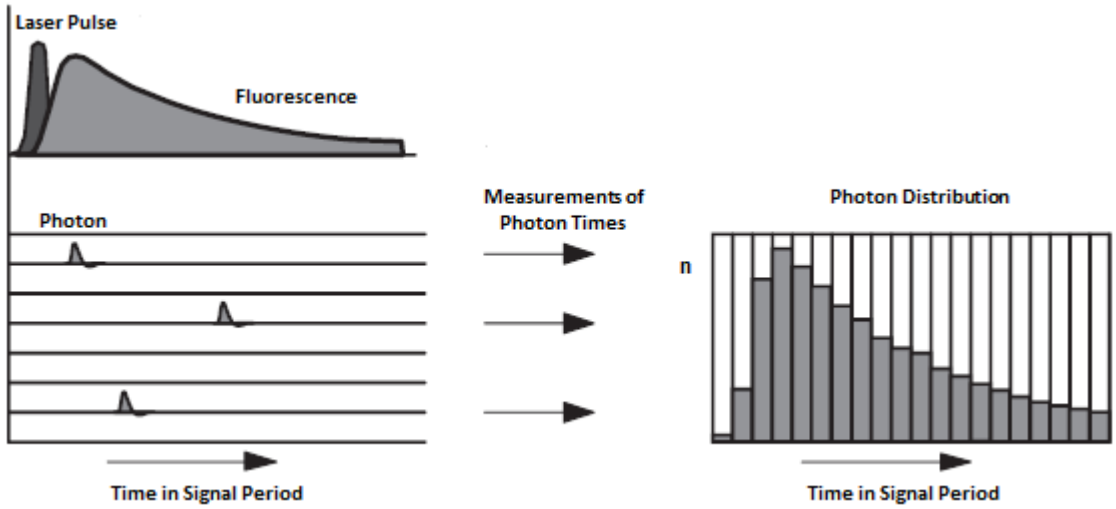

Figure 7. Principle of TCSPC. By laser pulse source with high repetition, a single photon emission is deteted and the time interval between laser pulse and detected photon is measured. The information is used to build up a one dimensional photon distribution over the time in the signal period (Figure is reproduced from (78)).

2.2.3. Analysis of time correlated single photon counting lifetime data

The TCSPC-FLIM system delivers images in which each pixel includes the fluorescence decay data of a fluorophore, e. g. a chromatin compaction probe as used in this lifetime study. By fitting the experimental lifetime data to a mathematical convolution function of a decay model and an instrument response function (IRF), the lifetime of a single or multiexponential decay can be calculated for each image pixel (24)

$$f_m(t) = \int_{\tau=0}^{t} f(\tau) IRF(t-\tau) d\tau \qquad (1.\ 13)$$

$$f(t) = \sum_{i=1}^{3} a_i e^{-t/\tau_i} + a_0 \qquad (1.\ 14)$$

where $f_m(t)$ represents measured fluorescence function. f (t) is the true fluorescence decay function. i is the number of exponential components. a_i and τ_i are the relative amplitude and lifetime of the exponential component, respectively. The constant a_0 refers to the offset correction. The parameters of the model function are modified until the most desirable fit with the measured decay data is achieved (least square fitting) (24). The average lifetime for the measured decay is calculated from the individual exponential components (24)

$$\tau_m = \sum_{i=1}^{3} a_i \tau_i \ / \sum_{i=1}^{3} a_i . \qquad (1.\ 15)$$

Usually, lifetime data are displayed as a pseudocolor coding indicating different lifetimes with different colors. In addition, lifetime distribution of the whole image or region of interests (ROIs) and fitting parameters of individual pixels can be extracted.

3. Materials and methods

3.1. Sample prepration

All cell lines were grown in 75 cm^2 culture flasks under standard conditions as monolayer cultures, 95 % air, 5 % CO_2, 37 °C and 100 % humid atmosphere. In this study following cell lines were used:

- **NIH 3T3 cells (ATCC, Manassas, USA):** Mouse embryonic fibroblasts. These cells were grown in dulbecco's modified eagle's medium (DMEM) supplemented with 10 % fetal calf cerum (FCS) and 4.5 g/l glucose, stable glutamine and Na-pyruvat
- **NIH-53 BP1-mCherry:** Mouse embryonic fibroblasts transiently expressing mCherry tagged 53 BP1. These cells also were grown in DMEM supplemented with 10 % FCS and 4.5 g/l glucose, stable glutamine and Na-pyruvat.
- **NIH - H2B-GFP/RFP-H2B:** Mouse embryonic fibroblasts transiently co-expressing both forms of histon H2B fused to either GFP or RFP. These cells also were grown in DMEM supplemented with 10 % FCS and 4.5 g/l glucose, stable glutamine and Na-pyruvat.
- **HeLa- H2B-GFP:** Human cell line transiently expressing GFP tagged H2B. These cells were grown in DMEM supplemented with 10 % FCS and 2 µg/l blasticidin in 200 µg/ml G418 (kindly provided by Dr. Daniele Zink, München, Germany)
- **HeLa- H2B-GFP/mCherry-H2B:** Human cell line stably expressing GFP tagged H2B and expressing mCherry tagged H2B. These cells were grown in DMEM supplemented with 10 % FCS and 2 µg/l blasticidin in 200 µg/ml G418 (kindly provided by Prof. Angus l. Lamond, university of Dundee, Scotland, UK).
- **AG 1522D (Corriel, USA):** Normal human fibroblasts (kindly provided by Tatyana Syzonenko, GSI, Darmstadt, Germany). These cells were grown in DMEM supplemented with 15 % FCS, 1% glutamin and 1% peniciline/ streptomycin
- **U2OS-G1/S-GFP NBS1-mCherry cells (Amersham, UK):** Human osteosarcoma cells stably expressing a GFP tagged cell cycle marker double transfected with NBS1-mCherry (kindly provided by Dr. Nicole Averbeck, GSI, Darmstadt, Germany). These cells were grown in DMEM supplemented with 10 % FCS and 4.5 g/l glucose Na-pyruvant.

3.2. Cell seeding

For FLIM measurements, cells were seeded one or two day (s) before experiments were carried out. Table 1 summarized information of cell seeding for the differnet approaches in the present study.

Measurement	Number of seeded cells	Selection media	Seeding plate	Provider
FLIM	1.5. 10^5, 3. 10^5	2 ml	Ø 35 mm glass bottom petri dishes	greiner bio-one, Germany
Offline IR (Au)-FLIM	3. 10^4	300 µl	4 µm thickness Polypropylene film	Goodfellow, UK
Offline IR (Xe)-FLIM	3.5. 10^4	300 µl	4 µm thickness Polypropylene film	Goodfellow, UK
IR (U)-FLIM	2.5. 10^5	2 ml	Ø 24 mm coverslip	Roth, Germany
IR (C)-FLIM	5.10^4	2 ml	25 µm thickness Lumox	Sarstedt, USA
X-rays-FLIM	3. 10^5	2 ml	Ø 35 mm glass bottom petri dishes	greiner bio-one, Germany
Cell cycle-FLIM (G_0, G_1)	10^5	2 ml	Ø 35 mm glass bottom petri dishes	greiner bio-one, Germany
Cell cycle-FLIM (G_1, G_2)	2.5. 10^5	2 ml	Ø 35 mm glass bottom petri dishes	greiner bio-one, Germany

Table 1. Cell seeding in different approaches of FLIM experiments.

Note, prior to X-rays irradiation, medium was replaced by 1 ml of the fresh medium.

3.3. Dye staining

- DNA dyes:

For live cells measurements, cells were stained prior to measurements with the listed concentrations and incubation times which were summarized in Table 2. After staining and incubation, DNA dye was washed away with fresh medium and FLIM measurements were carried out. Table 3 listed the concentrations and incubation times for staining of fixed cells.

DNA dye	Concentration (μM)	Incubation time (h)	DNA dye	Concentration (μM)	Incubation time (h)
Hoechst 33342	0.25, 0.5, 1	1	Syto Orange 83	1	1
DAPI*	1.5, 2, 3, 4.5, 6, 12,15	1	Cytrak Orange	0.5, 1	1
Hoechst 34580*	0.25, 0.5, 1	1	Syto Orange 85	1	1
Nuclear Violet*	0.25, 0.5, 1	1	Syto 64	1	1
Syto Blue 41	1	1	Syto 17	0.5, 1	1
Syto Blue 42	1	1	Syto 59	0.5, 1	1
Syto Blue 45	1	1	Syto 60	1	1
BENA 435[1]	1, 5, 10	1	Syto 61	1	1
Syto 13	0.5, 1, 1.5	0.5	Syto 62	1	1
Syto 16	1. 2.5	1	Syto 63	1	1
Oxidize DHE	1	2	Vybrant Ruby	0.5, 1	1
Picogreen	1	1	Draq 5	0.5, 1	1
Vybrant Green	1	1	SirHoechst	0.5, 1	1
Nuclear Green	0.5, 1, 3.1, 6, 12	1			
Syto Orange 81	1	1			
Syto Orange 80	1	1			
Syto Orange 82	1	1			

Table 2. List of DNA dyes which were used for DNA labeling in living cells. [1]BENA was kindly provided by Dr. Chi-Hung Nguyen, UMR 176 CNRS-Institut Curie, Centre Universitaire d'Orsay, France. * These dyes can be used in the fixed cells as well.

DNA dye	Concentration (μM)	Incubation time (h)
Sytox Blue	1	1
BEBO[1]	1	1

Table 3. List of DNA dyes which were used only for DNA labeling in fixed cells. [1] BEBO was kindly provided by Prof. Gunnar Westman, Chalmers University of technology, Goteborg, Sweden.

- Fluorescein

An aqueous solution of fluorescein was prepared and NaOH was added to the medium to reach a pH >9. Table 4 was provided the information for FLIM imaging of the fluorescein solution.

Dye	Conditins for τ measurements	Concentration (μM)	Ex/Em (nm)	λ_{Laser} (nm)	Filter
Fluorescein	NaOH/Water	2	488/490-520	488	534/42 BP/ 520 LP

Table 4. Configuration and concentration information of the FLIM measurements of Fluorescein.

3.4. Immunofluorescence staining

Cells were fixed in 2 % formaldehyde in PBS for 15 min and permeablized for 10 min in 0.5 % triton X-100 in PBS, followed by two washing steps with PBS. Samples were stored in 0.4 % BSA at 4 °C.

Antibody staining was carried out in 0.4 % BSA. The primary and secondary antibodies were incubated for 45 minutes and 30 minutes, respectively. Table 5 and 6 listed the primary and secondary antibodies used in the current study, respectively.

Antibody	Species	Dilution	Provider
XRCC1	Mouse	1:1000	Lab vission
53 BP1	Rabbit	1:500	Abcam
ϒH2AX	Mouse	1:500	Millipore

Table 5. List of primary antibodies used in this study.

Antibody	Antigene	Species	Dilution	Provider
Alexa 514	Mouse	Goat	1:400	Lifetechnology
Atto 647	Rabbit	Goat	1:200	Sigma
Atto 647	Mouse	Goat	1:200	Sigma

Table 6. List of secondary antibodies used in this study.

3.5. Chemical treatment

For modulating the chromatin status, cells were seeded in the glass bottom petri dishes and treated with various chemicals listed in the following.

3.5.1. Histone deacetylation inhibitors

- Valproic acid (VPA)

VPA (Sigma, Germany) was dissolved in PBS and was diluted in DMEM incuding 2 % FCS to a concentration of 1 mM. Then, VPA was added to the cells and incubated for 1 h or 24 h. Cells were washed with fresh medium and DNA dye incubation started as described before.

- Trichostatin A (TSA)

TSA (Sigma, Germany) at a concentration of 0.66 µM was added to cells and incubated for 24 h. Cells were washed using fresh cell medium and DNA staining was performed.

3.5.2. Hypotonic/ Hypertonic treatment

Performing osmolaric changes, first, the DNA staining was done and cells were washed with fresh medium. Cells were treated with 0.5 PBS or 4 fold PBS for 15 minutes and 5 minutes, respectively, directly at the FLIM microscope.

3.6. Experimental setup

3.6.1. FLIM setup

The beamline microscope of the GSI (79) was upgraded with a DCS-120 FLIM system including a scan head, a scan controller, a scan amplifier, TCSPC modules, two hybrid detectors, a detector controller, and several picosecond (ps) diode lasers operating at 80 MHz. The microscope was equipped with a stage top incubator. The components used were listed in Table 7.

Component	Model	Manufacturer
Microscope	IX71	Olympus
Objective	60x water immersion objective lens, NA=1.2	Olympus
Incubation chamber	INUB-PI, GM-8000	Hokai Hit, Japan
Scan head	DCS-120	Becker & Hickl, Germany
Scan controller	GVD-120	Becker & Hickl, Germany
Scan amplifier	GDA-121	Becker & Hickl, Germany
TCSPC modules	SPC-150	Becker & Hickl, Germany
Detector	Hybrid detector (HPM-100-40)	Becker & Hickl, Germany
Detector controller	DCC-100	Becker & Hickl, Germany
Excitation laser	ps diode laser (BDL-405-SMN, BDL-445-SMC, BDL-488-SMN, BDL-515-SMN, BDL-640-SMN)	Becker & Hickl, Germany

Table 7. Detailed information of components used in the FLIM setup at GSI.

Confocal images were recorded at 512 × 512 frame size and an acquisition time of 10-20 s. Taking the advantage of having sufficient memory space in the computer, all imaging experiments were carried out in the FIFO imaging mode the so-called standard FLIM mode of the Becker & Hickl (bh) FLIM system. The scan rate was set to the maximum. The fast moving galvanometers mirrors deflect the laser beams and sent to the microscope beam path for scanning over the focal plane of the sample. The control of the scanner is totally integrated in the instrument software (B&H Galvano Scanner). The fluorescent light returned from the sample and is deflected again by the galvanometers mirrors (descanned detection) before pathing the reflecting mirror (30/70). By the secondary beamsplitter wheel, the fluorescent light split either into two spectral ranges. Thereafter, the fluorescent light is focused on the selectable confocal pinholes. Using appropriate emission filters (listed in Table (A.1) in Appendix), the spectral detection ranges of each detection channels can be determined. Single photons were recorded by the hybrid-detectors and processed in the SPC modules. In the PC- memory the distribution of photon arrival times (t) over x, y built up and the result is an image including of a fluorescenece decay curve in each pixel. A schematic illustration of our FLIM setup and a picture of FLIM setup at GSI were shown in Figure 8 and 9, respectively.

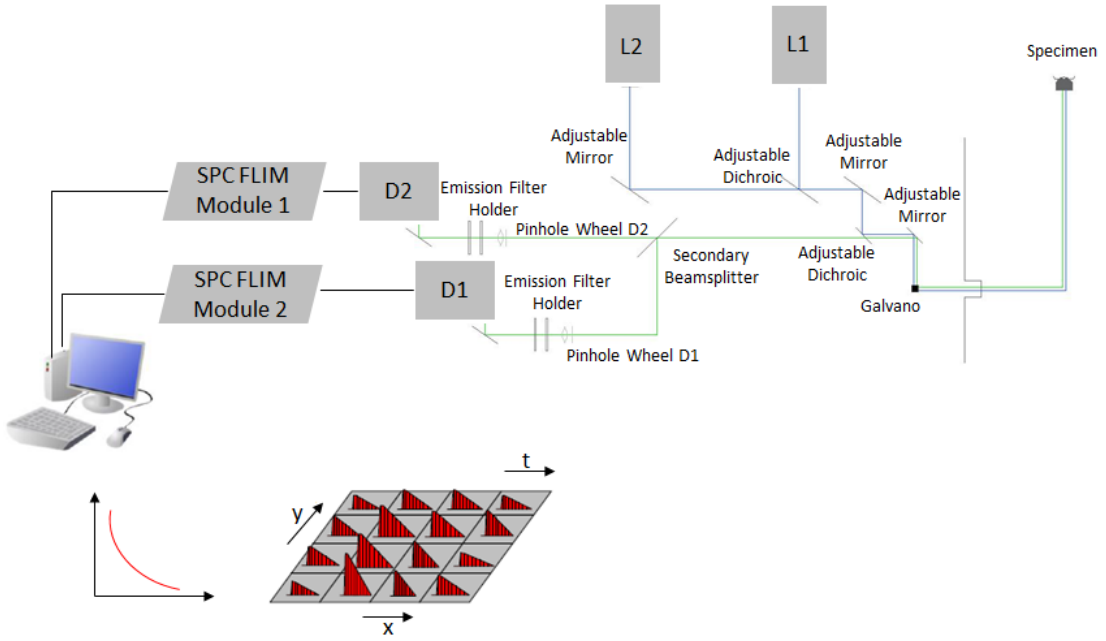

Figure 8. Schematic illustration of the FLIM-TCSPC. L_1 and L_2 stand for ps diode lasers. D_1 and D_2 represent two hybrid detectors.

Figure 9. A photo of the FLIM setup combined with a 35 kV X-rays tube. (a) The microscope, scan head and detectors were located on a TMC breadboard table. The microscope and scan head were covered with a shielding steel box for radiation protection. The laser switch box, the delay switch box, ps diode lasers, scan amplifier and simple Tau system incuding TCSPC modules are shown in the left side of the microscope. A hand control unit is used to manually control position of the pinhole and the joystick is used to manually move the microscope stage. (b) Stage top incubator that was equipped with a gas mixing unit (GM-8000) and a customized lid that was used during the irradiation.

Calibration and alignment of the FLIM setup and microscope was perfomed using commercially available standard slides (SLE-010, Argolight SA, France; FocalCheck fluorescence microscope test slide #1, Molecular probes, USA). To test the image distortion and intensity responses of the FLIM system, the Argolight's slide has been used. The Argolight's slide contains a specific glass substrate which is embedded in a stainless steel carrier with the dimensions 75 mm × 25 mm and thickness of 1.50 mm (Figure 10 panel (a)). It constituted a variety of stable fluorescent patterns at the depth of 180 ± 5 µm from the top surface of the glass (Figure A.15). For example: by using Argolight's slide, the thickness/ distance of the lines can be measured an used to optimize the resolution (x and y by making them as confined as possible via adjusting the scanner. The laser and the pinhole were aligned until a non distorted image was acquired. The FocalCheck fluorescence microscope test slide #1 included 10 sample areas coated with fluorescent microspheres (Table A.16). For instance: UV/ visible wavelenght alignment can be obtained upon aligning of the green ring with blue disc which were located in the area 2 of the row A. Here, also, the laser and the pinhole were aligned until a non distorted image was obtained. Table 8 listed the configurations used for FLIM measurements of the Argolight's slide, e. g. for the 405 nm ps diode laser.

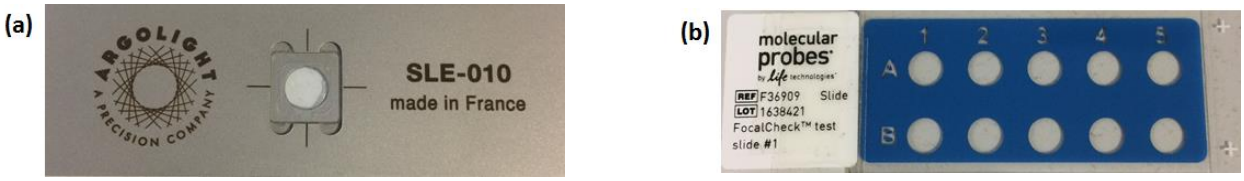

Figure 10. Calibration and alignement of FLIM utilizing standard slides. (a) Argolights slide consisting different fluorescent patterns. (b) FocalCheck fluorescence microscope test slide #1.

Microscope	Olympus IX71
Objective	60 x water immersion lens, NA: 1.2
Filter	435 LP
Laser	100% of total power of 405 nm
FLIM setting	Exposure time: 20 s

Table 8. Configurations used for FLIM measurements of the Argolight's slide using 405 nm ps diode laser.

In order to do spectra measurements, the illumination target aperture was placed centrally on the optical axis of the FLIM microscope stage. The measurement has been done either after the objective lens of the FLIM miscorscope (405 nm ps diode laser) or the lasers were coupled with a remote interlock connector and then the spectra acquired without being attached to the microscope.

3.6.2. FLIM beamline microscopy and irradiation

Charged particle irradiation was carried out at the accelerator facilities of the GSI Helmholzzentrum für Schwerionenforschung GmbH using different ion species which were mainly determined by availability of beamtime at the accelerator. Figure 11 showed the FLIM setup coupled to the beamline (UNILAC accelarator) microscope at GSI. As seen in Figure 9, alternatively, the FLIM setup can be combined with a 35 kV X-rays tube (GE Inspection Technology, Germany) operating at 80 mA that deliveres a dose rate of about 1 Gy/s at a cell layer.

Ion	LET (keV/µm)	Energy on target (MeV/u)	@
Gold (Au)	12290	4.5	Microprobe
Xenon (Xe)	750	600	SIS
Carbon (C)	325	4.0	UNILAC
Uranium (U)	15000	4.7	UNILAC

Table 9. Accelerated ions and corresponding LET and energy values.

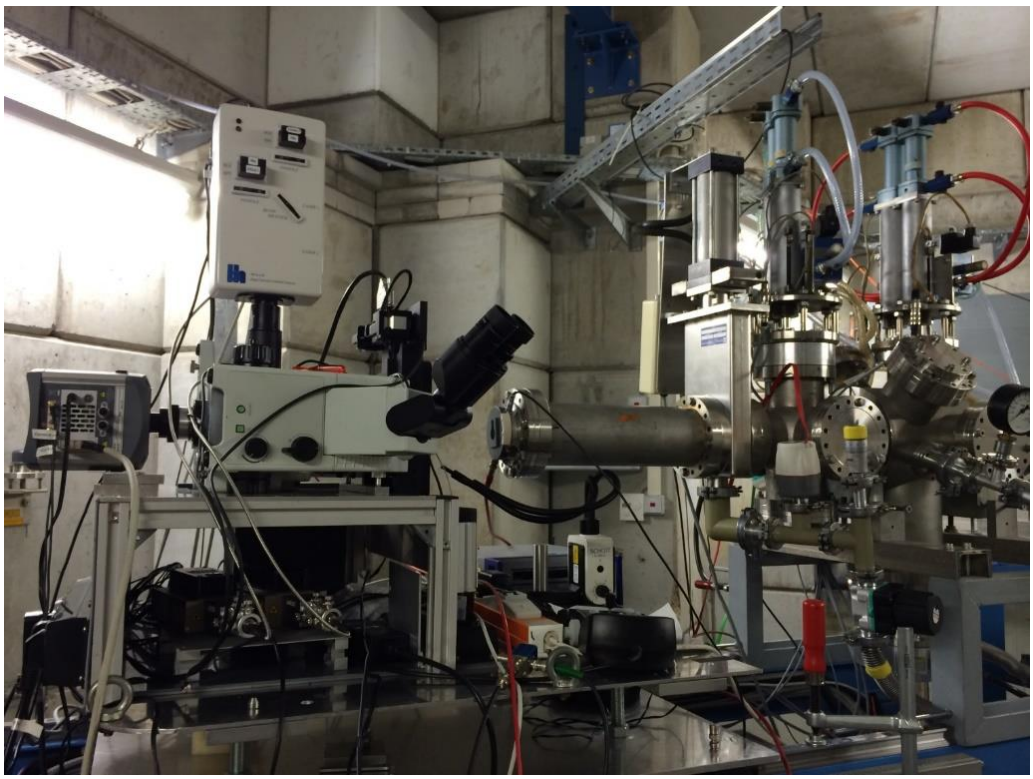

Figure 11. A photo of the FLIM setup coupled to the beamline microscope at the UNILAC accelarator. The beamline exit window is at the right side of the microscope. An EM-CCD camera is also mounted to the microscope to provide intensity based real-time images of the sample (52).

3.7. Data analysis of lifetime images

The obtained fluorescent lifetime images were analyzed using SPCImage (version 5.1 and 5.6, Becker & Hickl, Germany), ImageJ software version 1.48v (http://imagej.nih.gov/ji). Data were plotted using Origin pro software (Version 9.0.0 (32-bit) SR2 b87, Northampton, USA).

Figure 12 shows the main panel of the SPCImage data analysis software. The intensity and lifetime images are depicted in the upper left and middle of the panel, respectively. The lifetime distribution histogram of the selected ROI is shown in the upper right of the panel. Moreover, the fluorescence decay curve of the selected spot and the corresponding decay parameters are exhibited in the lower left and right, respectively. A good fit is designated by a χ^2 close to 1 and residuals showing no significant systematic variation.

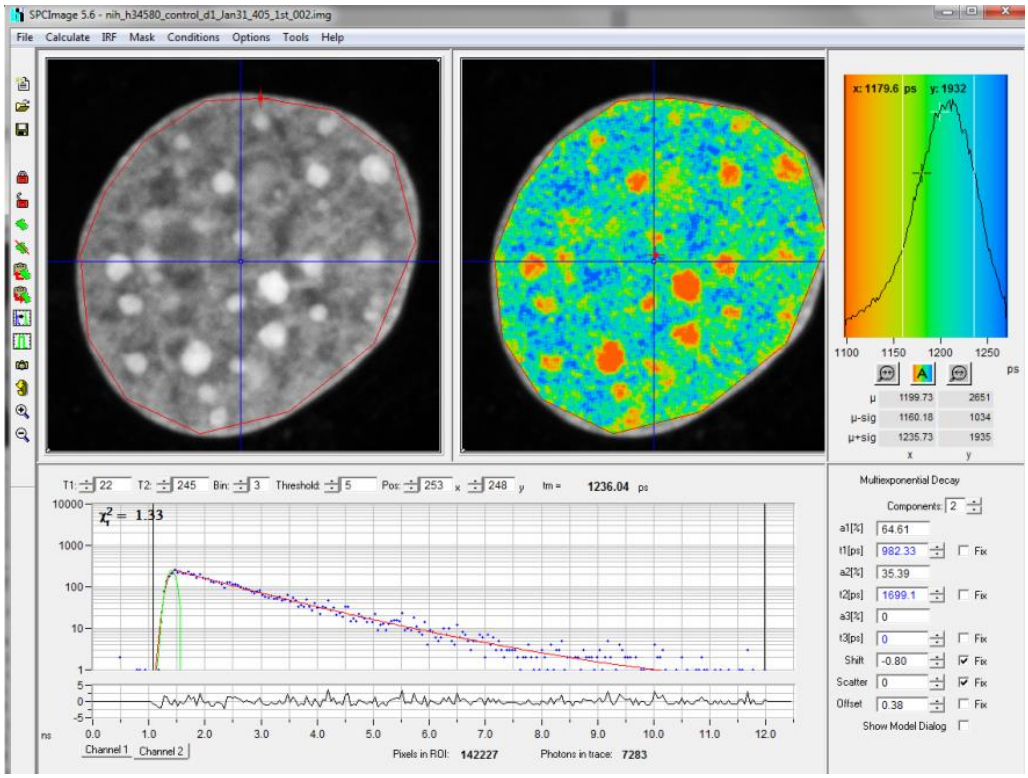

Figure 12. SPCImage panel after calculating the lifetime. The intensity image, lifetime image and lifetime distribution are shown in the upper of the panel, respectively. The fluorescence decay curve and decay parameter are presented in the lower part of the panel. The SPCImage software version was 5.6.

The fluorescence lifetime fit was analysed using Chi- square (χ^2) test, and for each of the chromatin compaction probes the best model (number of exponentials) was choosen. Figure 13 panel (a) and (b) showed an example of the decay curve of the exponential models considering the instrument response function (monoexponential (a) and biexponential (b)) in which the photon decay data (black line) and fit curves (red line) were shown. The model parameters were listed in Table 10. As seen, in the case of argolight fluorescent pattern, a double exponential function revealed a much better fit with a smaller value for χ^2 of 1.75.

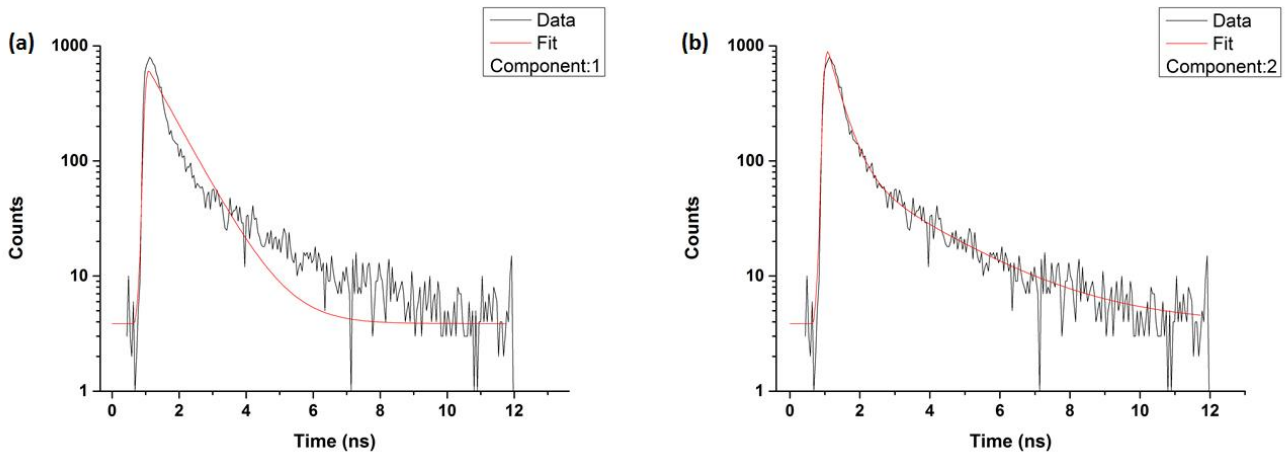

Figure 13. Fitting a decay profile with one (a) and two (b) exponential components.

	Component:1	Component:2
	(a)	(b)
χ^2	14.19	1.75
τ_1(ps)	842	359
τ_2 (ps)	-	2200
a_1	100%	92%
a_2	-	8%

Table 10. Model parameters of the lifetime analysis. τ_1, τ_2, a_1 and a_2 are lifetimes and amplitudes of the exponential components, respectively.

Images of photon numbers (intensity) as well as calculated lifetime images were exported and further processed using ImageJ software, where image segmentation and quantitative analysis were performed. To provide a quantitative description of hit chromocenter and suppress noise, radial averaging was done by using profiles and radial angle integration around the site of heterochromatic ion traversal (radial angle plot plugin, Paul Baggethun, 2002) in ImageJ.

4. Results

4.1. Physical characterization of the FLIM setup at GSI

To investigate the effect of temperature, cycling time and the reproducibility of the measurements of our FLIM system, FLIM experiments were performed using an aqueous solution of fluorescein dye. Since fluorescein is widely used in practical applications, e. g. lasers and fluorescent probes and its physical properties are well-known, it was used as standard fluorophore. Note, FLIM measurements were repeated three times either using a heated environmental chamber along with adjustable CO_2/O_2 condition for cell incubation or without it because of the influence of the temperature on measured lifetime. Figure 14 depicted the results in which not employing the heated environmental chamber and employing of it were represented by cold and warm, respectively. The measured mean lifetime values were listed in Table 11. As seen, the temprature had no impact on the readouts. Moreover, the fluorescence lifetime values listed in the table are relatively robust.

Temperature	Integration time (s)	τ_m (ps)		
Cold	20	3978± 74	3980± 75	3980± 75
Cold	60	3910± 46	3978± 39	3979± 39
Warm	20	3985± 76	3983± 77	3984± 77
Warm	60	3984± 45	3983± 45	3983± 45

Table 11. The measured fluorescence lifetime of fluorescein employing (warm)/ not employing (cold) environmental chamber.

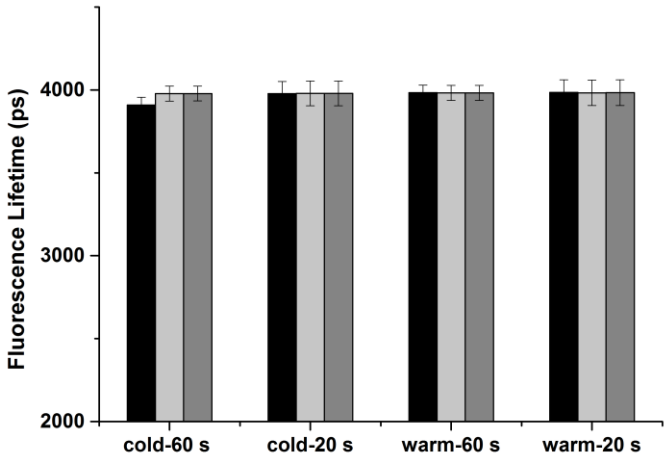

Figure 14. Robustness of the fluorescence lifetime value. Error bars indicate mean ± SD.

The spectra power of each laser was measured at 80 MHz repetition rate using a commercially available LumaSpec LS800S. Prior to the measurements, all lasers powers were manually set to have the maximum output. Figure 15 showed the measured irradiancce of the available FLIM lasers, e. g. 405 nm, 445 nm, 515 nm and 640 nm. The results confirmed the effective optical power at the corresponding wavelengths of FLIM lasers and the absence of secondary emission lines.

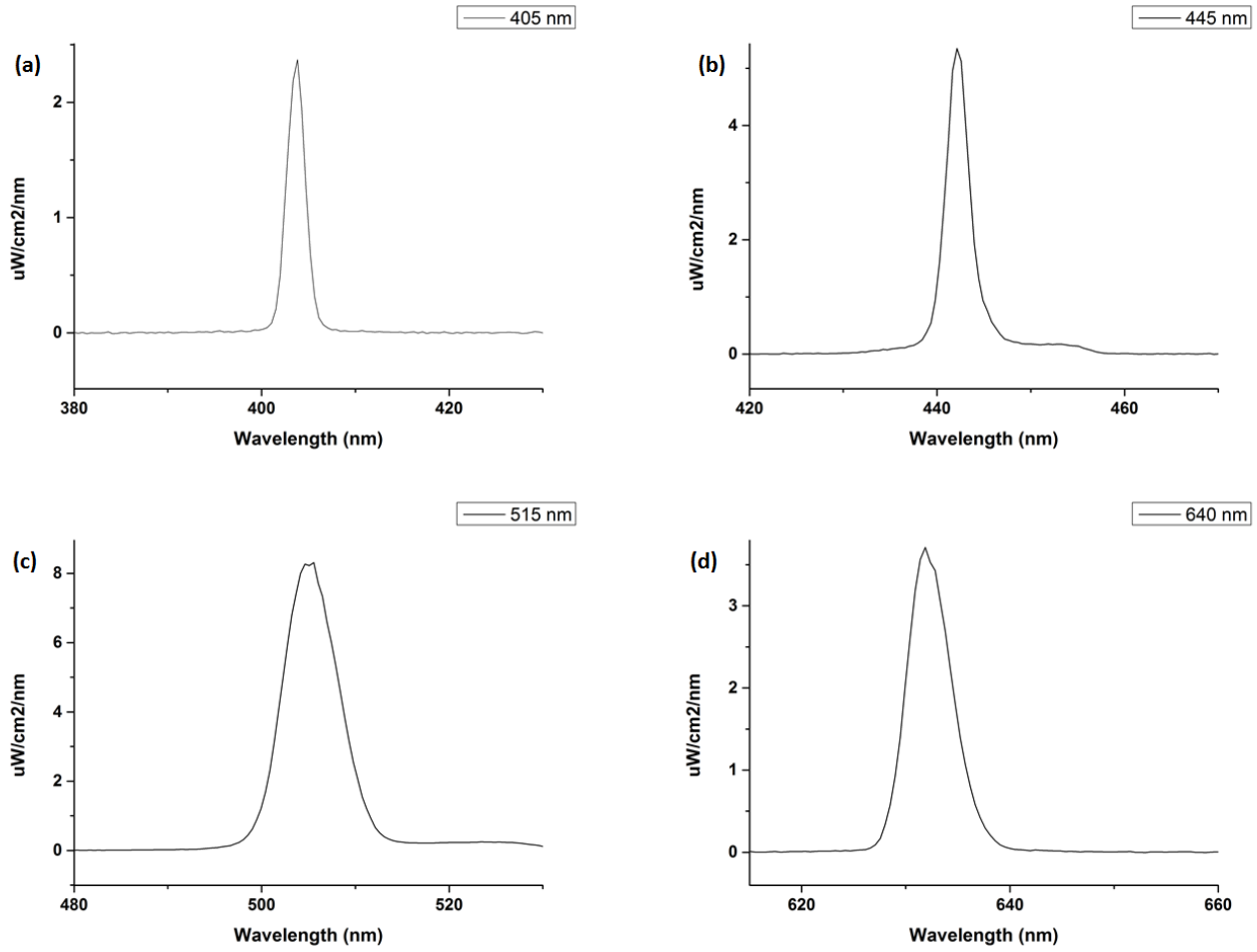

Figure 15. Emission spectra of available diode lasers of FLIM setup with different wevelength (a) 405 nm, (b) 445 nm, (c) 515 nm and (d) 640 nm.

4.2. Establishment of a FLIM based chromatin compaction assay

As mentioned earlier, radiation-induced DNA DSBs are the most important lesions regarding their impact on human health. Also, one of the major challenges in radiation biology is the incomplete knowledge about mechanisms and structural details of DNA damage repair within chromatin. While the recent studies (9; 18) suggested that radiation-induced chromatin relaxation and damage relocation might have an impact on DNA repair, the mechanism of DSB movement and its correlation to the radiation-induced chromatin decompaction are quite unclear. The drawbacks which limit the use of intensity-based chromatin decondensation measurements in living cells are the only moderate irradiation induced changes, the influence of staining variability and the intrinsic problem of not being able to discriminate between chromatin decondensation and a reduction of available dye binding sites mimicking a decompaction. Thus, a competing technique which provides a more sensitive readout in combination with an output which is independent of the intensity information and which is functional in living cells, is highly desirable. Fluorescence lifetime imaging technique seems to be a promising technique to reach the aforemetioned characteristics since it is considered to be independent of fluorophore concentration.

4.2.1. Sensitivity of newly established chromatin sensors upon modulation of chromatin compaction

Recently, Llères et al started to utilize the FLIM-FRET approach to monitor the chromatin compaction level in living cells (75). They reported a FRET based methodology in which energy is transferred between histone molecules tagged with either GFP (donor) and mCherry (acceptor) leading to a drop-off in the lifetime value of GFP. A similar approach was applied to validate the sensitivity of the FLIM setup at GSI. To assess occurance of FRET, as control, the fluorescence lifetime of the GFP in the present of mCherry was measured. A decrease in the mean lifetime of GFP was noticed from 2387 ± 40 to 2280 ± 21 ps after co-expressing mCherry, in turn, revealed that FRET between GFP (donor) and mCherry (acceptor) occured. FRET efficiency about 4 % was calculated according to Eq (1.8). Hence, the outcome proved that our FLIM setup was capable of performing FLIM-FRET measurements.

Figure 16 shows an example of the intensity and lifetime images of the HeLa H2B-2FP cell line. The fluorescence lifetime is presented in a continous pseudocolor scale ranging from 2139 to 2389 ps. The mean lifetime value of H2B-GFP in the shown nucleus in the present of mCherry was calculated to be τ_m = 2259 ± 62 ps.

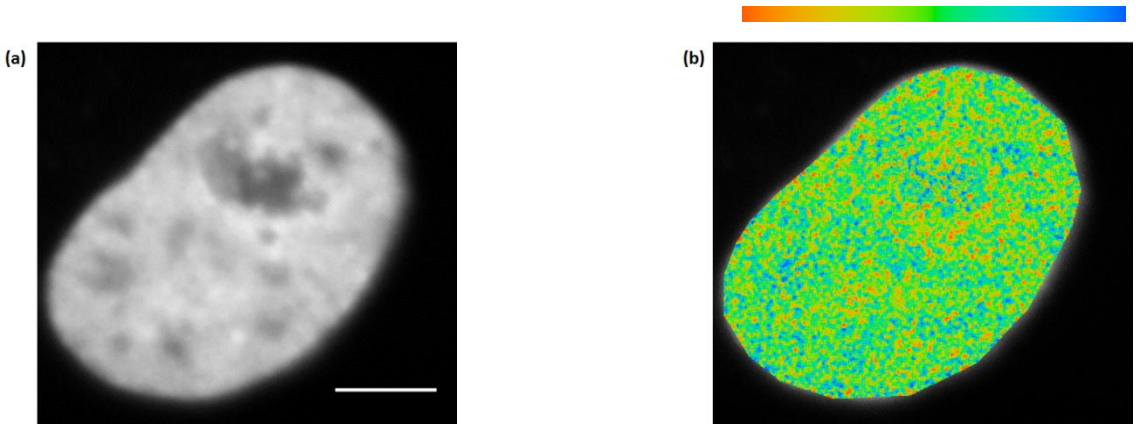

Figure 16. FLIM-FRET measurement at GSI. Intensity (left) and lifetime (right) images of H2B-GFP/mCherry in HeLa H2B-2FP stable cell. Scale bar, 5µm.

Valproic acid (VPA) is well-known histone deacetylase inhibitors (HDACi). It has been reported that VPA gives rise to inhibit cellular HDAC activity which is accompanied by modification in chromatin structure and function (80; 81; 82; 83). HDAC activity is associated with changes in gene expression and oncogenic transformation (80). The acetylation status of histones is linked to the density of the chromatin. It has been found that VPA treatment induces chromatin decompaction in the cells (81; 83). Thus, to demonstarte that our probe is indicating chromatin density changes and also to address the sensitivity of our method, FLIM measurements have been performed after 24 h VPA treatment. Treatment induced changes were quantified by calculating the mean lifetime using Eq (1.8). Figure 17 depicts the measured mean lifetime of FLIM-FRET assay for 10 nuclei. As seen in Figure 17, the mean lifetime of GFP increased to 2350 ± 40 ps leading to a decrease in FRET efficiency (1.5 %) validating the expected chromatin decompaction after VPA treatment. To achieve a more compacted chromatin state in comparison, HeLa H2B-2FP cells were treated with hyperosmolar medium (4 fold PBS) for 5 minutes and FLIM measurements were done. As expected, after 4 fold PBS treatment, chromatin in HeLa H2B-2FP cells was more condensed which gave rise to an increase of FRET efficiency to about 11 %, i. e. the mean lifetime value showed a significant reduction from 2387 ± 40 to 2130 ± 40 ps. The measured lifetime values are summarized in Table 12. Overall, it was demonstrated that our confocal FLIM setup at GSI is sensitive enough to monitor the chromatin compaction status in human cells with a high local resolution.

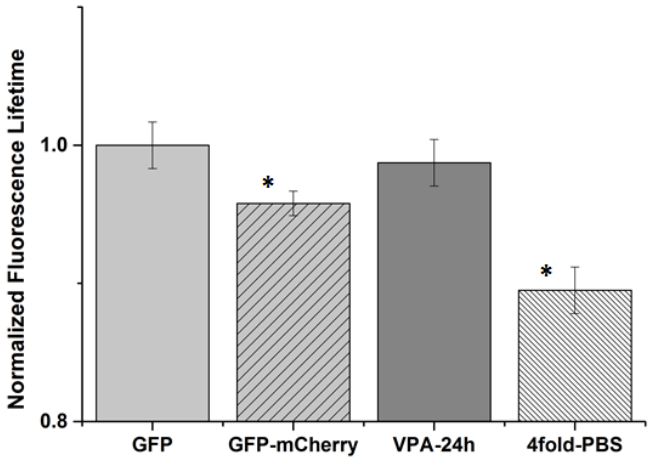

Figure 17. Modulation of the chromatin status and evaluation by FLIM-FRET assay (GFP: donor; mCherry: acceptor). Asterisks show $p < 0.05$ (using t-test) compared with control. Error bars indicate mean ± SD.

	τ_m (ps)
GFP	2387±40
GFP-mCherry	2280±21
VPA (24h)	2350±40
4 fold PBS	2130±40

Table 12. Measured fluorescence lifetime of GFP by FLIM-FRET assay (GFP: donor; mCherry: acceptor).

In contrast to human cells, murine cells contain clearly distinguishable heterochromatic chromocenters, which can be visulized by intense DNA labeling. NIH 3T3 cells have been used as a model system for our FLIM-FRET approach. Due to availability of the plasimids, the forms of histon H2B fused to either GFP (donor) or RFP (acceptor) were transiently co-expressed, which are also able to generate a FRET pair when they are in the close visinity. As control, NIH 3T3 cells experessing H2B-GFP only were imaged. The intensity and lifetime images of GFP in the presence of RFP were acquired. The global decrease in the mean lifetime of H2B-GPF (donor) in the presence of H2B-RFP from 2387 ± 40 to 2350 ± 19 ps was calculated. A small drop-off in the mean lifetime of the donor indicates FRET interaction between the two tagged forms of histone H2B. A FRET efficiency of ~ 4 % was calculated according to the Eq (1.8). In The lifetime contrast of condensed areas becomes evident, compared to the more spatially-homogeneous lifetime distribution after expression of H2B- GFP alone. To demonstrate that this FRET pair is indicating chromatin density changes and to address its sensitivity, NIH H2B-2FP cells have been exposed with VPA for 1 h or 24 h for chromatin decompaction or, to induce chromatin compaction, have been treated with hypertonic medium (4 fold PBS).

The mean lifetime value of the GFP increased to 2390 ± 31 ps proving the expected chromatin decompaction upon treatment with VPA. The chromatin compaction upon osmolarity changes was detected by a significant reduction of the lifetime to 2200± 69 ps. The measured lifetime values are summarized in Figure 18 and Table 13. An example of FLIM-FRET based measurements of NIH H2B-2FP cells is shown in Figure 19. The induced changes in lifetime values are deflected in the lifetime distribution curves, which are shown in the right column of Figure 19.

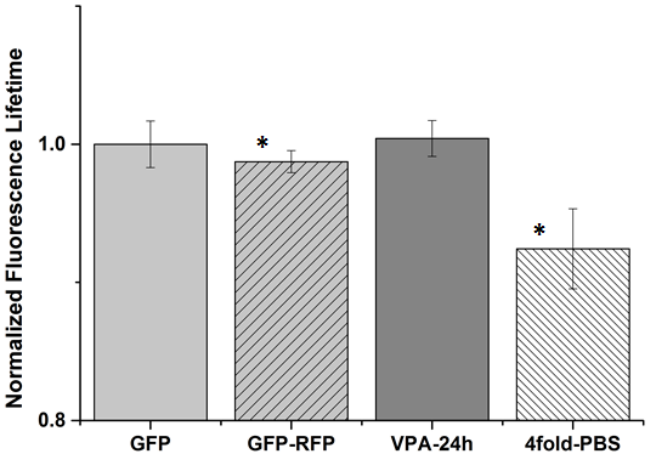

Figure 18. Modulation of the chromatin status and evaluation by FLIM-FRET assay (GFP: donor; RFP: acceptor). Asterisks show $p < 0.05$ (using t-test) compare with control. Error bars indicate mean ± SD.

	τ_m (ps)
GFP	2387±40
GFP-RFP	2350±19
VPA (24h)	2390±31
4 fold PBS	2200±69

Table 13. Measured fluorescence lifetime of GFP by FLIM-FRET assay (GFP: donor; RFP: acceptor).

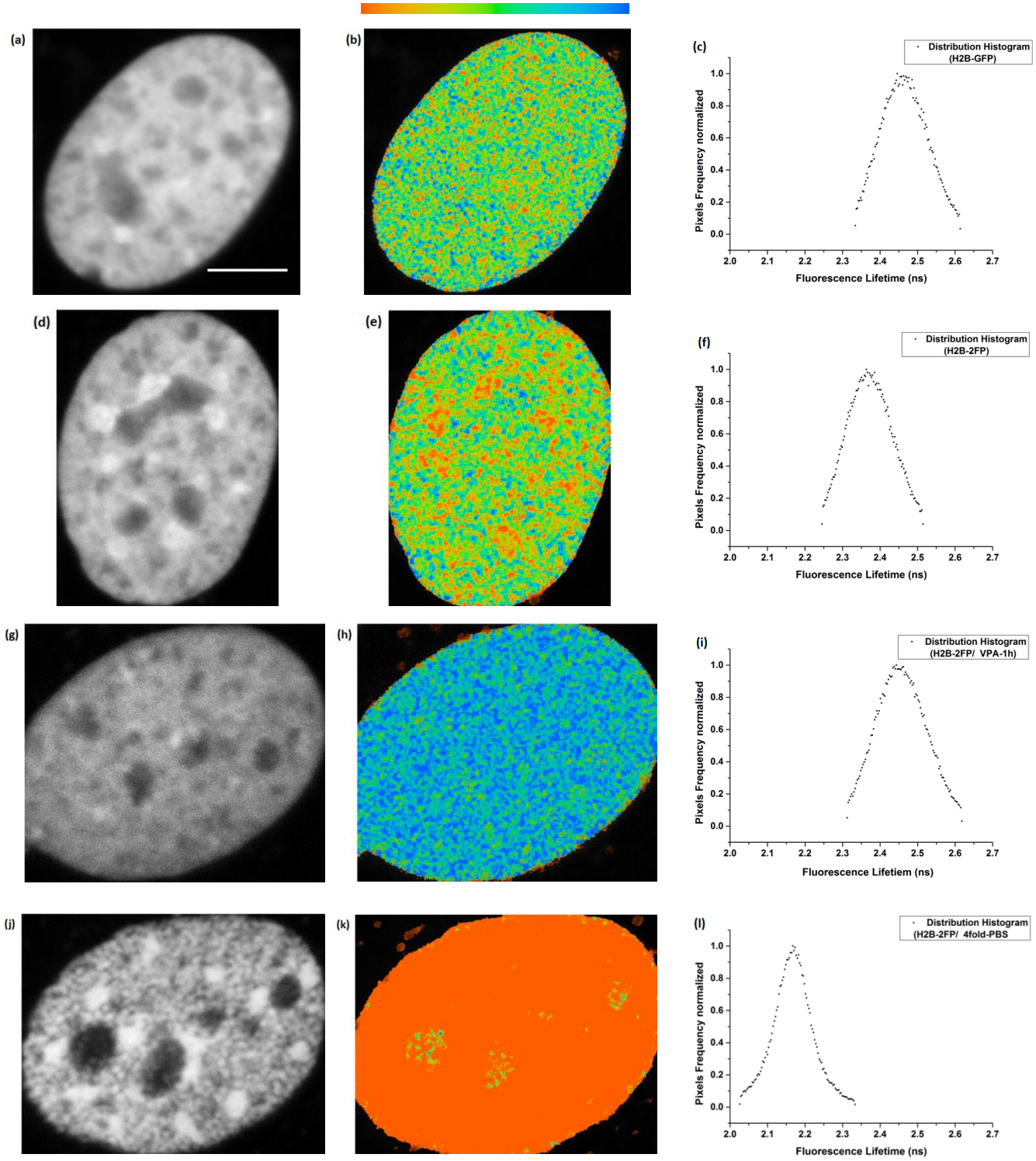

Figure 19. FLIM-FRET measurements of H2B-GFP/RFP in NIH3T3 cells. (a, b) Fluorescence intensity and lifetime of H2B-GFP without expression of H2B-RFP (2466 ± 70). (d, e) Expression of H2B-GFP together with H2B-RFP leads to a chromatin compaction dependent drop in the fluorescence lifetime of H2B-GFP due to FRET (2375 ± 67). (g, h, j and k) Modulation of chromatin compaction and H2B-GFP/RFP lifetime by VPA (2397 ± 133) (1 h) or 4 fold PBS (2168 ± 75) treatment. The spatial distribution of the fluorescence lifetimes are shown in c, f, j, l. Scale bar, 5 µm.

4.2.2. Screening of organic DNA binding dyes as potential chromatin compaction probes in living cells

So far, to assess the chromatin compaction status in the living cells, a FLIM-FRET approach with a fluorescent protein (FP) pair has been applied. It was demonstrated that the readouts were in the agreement with the published work (75). One of the drawbacks which hinder the use of FP-tagged histones as FRET pair is the limitation in dynamic range especially for decondensation measurements. An additional disadvantage of such probes is the confinement to special cellular systems or conditions, as they are relying on genetically modified cell lines or transient transfection. To eliminate these drawbacks, chromocenters were labled by cell permeable DNA dyes, e. g. Syto 16. It became evident that some showed a decreased lifetime at compacted chromatin. Figure 20 shows intensity (a) and lifetime (b) images of NIH 3T3 living cells stained with Syto 16. As seen, high intensity regions (chromocenters/heterchromatin) in the intensity image revealed a low lifetime in the lifetime image, which indicated that this probe is able to identify chromatin dense, heterochromatin regions based on lifetime information. Also, the regions showing longer lifetime reflect the non-condensed area. It is worth to highlight that, the discrimination between lifetimes of the condensed and non-condensed areas is critical for the quantification of the chromatin condensation status in the living cells. To quantify lifetime contrast, the intensity correlation quotient (ICQ; - 0.5< ICQ< 0.5) was calculated. To obtain well distinguishable signals, the ICQ value must be in the range of - 0.5< ICQ<0. The clear lifetime contrast between condensed and non-condensed areas with Syto 16 labeling yielded a ICQ value of - 0.18 calculated by using Image J.The intensity and lifetime correlation of the Syto 16 is shown as scatter plot in right column of Figure 20. ICQ values of organic dyes showing a lifetime contrast and thus might serve as potential chromatin compaction probes are summarized in Table 18.

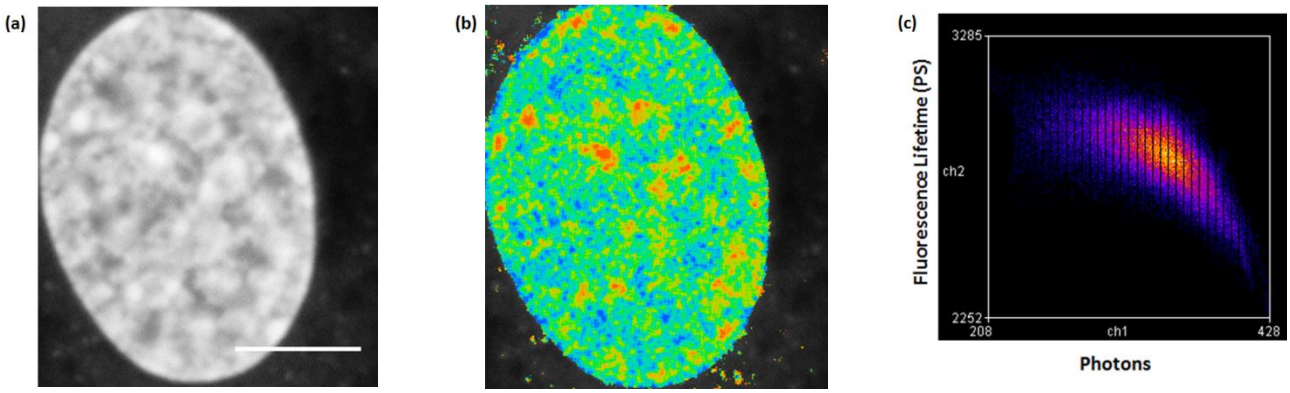

Figure 20. The intensity and lifetime images of NIH 3T3 living cells stained with Syto 16. (a) Intensity image (b) lifetime image and (c) scatter plot. The fluorescence lifetime is depicted in the continous pseudocolor scale ranging from 2424 to 3181 ps. Scale bar, 5 µm.

As Syto 16 was rather photolabile, alternative DNA dyes were screened for their ability to serve as sensitive and promising chromatin compaction probes. To inspect their intracellular distribution (DNA/RNA staining, eu-/heterochromatic staining), the distribution of lifetimes, photostability, dye uptake and excitability by

available lasers, FLIM measurements were done for a variety of dyes. Example of tested DNA probes in living cells are listed in Table 14 and 15.

DNA dye	Ex/Em nm (maxima)	DNA dye	Ex/Em nm (maxima)
Hoechst 33342	350/461	Syto Orange 83	543/559
DAPI*	358/461	Cytrak Orange	520/615
Hoechst 34580*	392/440	Syto Orange 85	567/583
Nuclear Violet*	401/459	Syto 64	599/619
Syto Blue 41	430/454	Syto 17	621/634
Syto Blue 42	433/460	Syto 59	622/645
Syto Blue 45	455/484	Syto 60	652/678
BENA 435	435/484	Syto 61	628/645
Syto 13	488/491	Syto 62	652/676
Syto 16	488/518	Syto 63	657/673
Oxidize DHE	490/590	Vybrant Ruby	638/686
Picogreen	502/523	Draq 5	646/681
Vybrant Green	506/534	SirHoechst	652/674
Nuclear Green	503/526		
Syto Orange 81	530/544		
Syto Orange 80	531/545		
Syto Orange 82	541/560		

Table 14. List of DNA dyes which were used for DNA labeling in the living cells (84; 85; 86; 87). * These dyes can be used in fixed cells as well.

DNA dye	Ex/Em nm (maxima)
Sytox Blue	444/480
BEBO	468/492

Table 15. List of DNA dyes which were used only for DNA labeling in fixed cells (88).

Figure 21 depicts the intensity (left) and lifetime (middle) images of cell nuclei stained with cell permeable DNA dyes, e. g. Syto Blue 45 (upper row) and Nuclear Green (lower low). Also, the intensity and lifetime correlation of the DNA dyes are exhibited as scatter plot in the right column of Figure 21. The fluorescence lifetime are represented in the continous pseudocolor scales as listed in Table 17. As seen in Figure 21, there

was no lifetime contast between eu- and heterochromatic regions in cell nuclei stained by the aformentioned DNA two dyes. The large bright areas in the cell nucleus stained by Syto Blue 45 did not resemble normally observed chromocenters and most probably is due to intense RNA staining in the nucleoli. RNA binding is also indicated by a strong cytoplasmatic staining (Panel (a)). Hence, dyes like the exemplarily shown Syto Blue 45 and Nuclear Green were excluded from further investigation.

DNA dye	τ_m (ps)
Syto Blue 45	2432-3441
Nuclear Green	2272-2768

Table 16. Lifetime distribution of Syto Blue 45 and Nuclear Green which were shown in Figure 21.

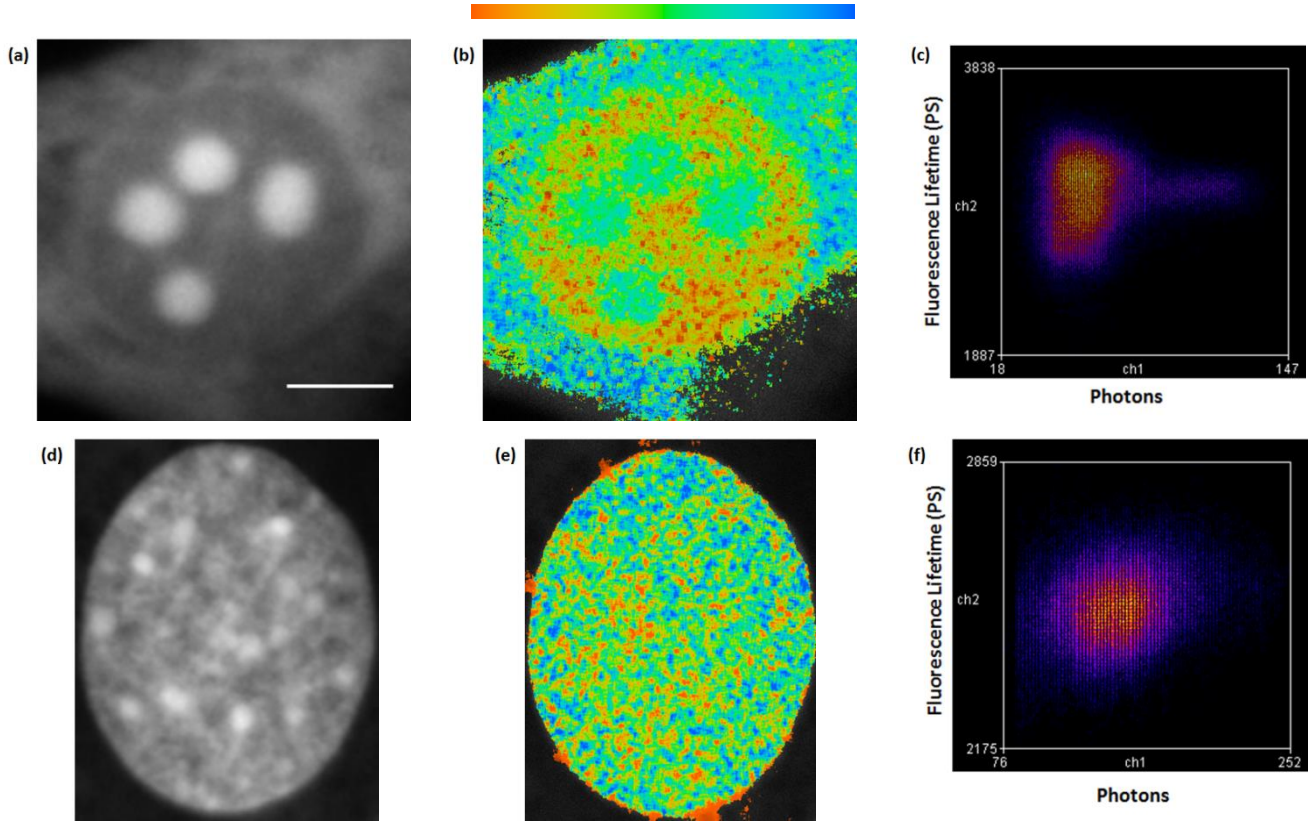

Figure 21. The intensity and lifetime images of living NIH 3T3 cells stained with Syto Blue 45 (upper) or Nuclear Green (lower). Intensity (a, d), lifetime (b, e) images and the scatter plots (c, f) are shown in the left, middle and right column, respectively. Scale bar, 5 μm.

Figue 22 shows intensity (a, d, and g) and lifetime (b, e, and h) images of the living NIH 3T3 cell nuclei stained with Nuclear Violet, Hoechst 33342 and Hoechst 34580. The bright areas in the intesity images corresponded to the shorter lifetime in lifetime images, i. e. the compacted chromatin was represented by

lower lifetime. The intensity and lifetime correlation of Nuclear Violet, Hoechst 33342 and Hoechst 34580 are exhibited as scatter plot in the right column of Figure 22 panel (c), (f) and (i), respectively. ICQ values can be found in Table 18.

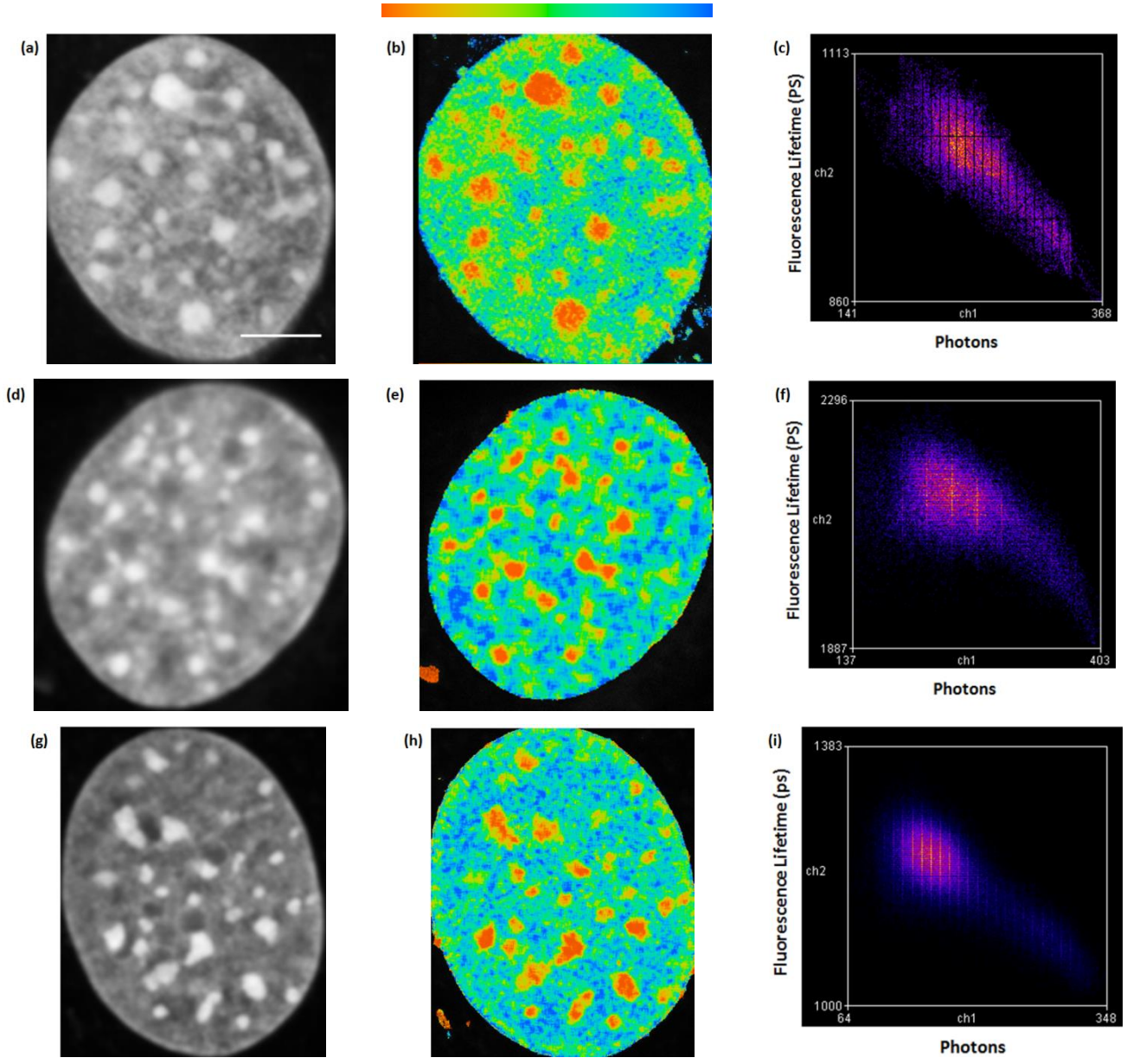

Figure 22. The intensity and lifetime images of living NIH 3T3 cells stained with Nuclear Violet (upper), Hoechst 33342 (middle) or Hoechst 34580 (lower). Intensity, lifetime images and the scatter plots are shown in the left, middle and right column of each row, respectively.

The fluorescence lifetime are shown in the continous pseudocolor scale ranging as listed in Table 17.

DNA dye	τ_m (ps)
Nuclear Violet	905-1124
Hoechst 33342	1821-2125
Hoechst 34580	1073-1204

Table 17. Lifetime distribution of Nuclear Violet, Hoechst 33342 and Hoechst 34580 which were depicted in Figure 22.

The intensity (left) and lifetime (middle) images of the living NIH 3T3 cells nuclei stained with Syto 13 were exhibited in Figure 23. The large intermediate bright areas in the intesity image show the nucleoli staining where brighter regions around them correspond to perinucleolar heterochromatin or chromocenters showing a shorter lifetime in the lifetime image, i. e. compacted chromatin was represented by lower lifetimes. The intensity and lifetime correlation of the Syto 13 is shown as scatter plot in the right column of Figure 23.

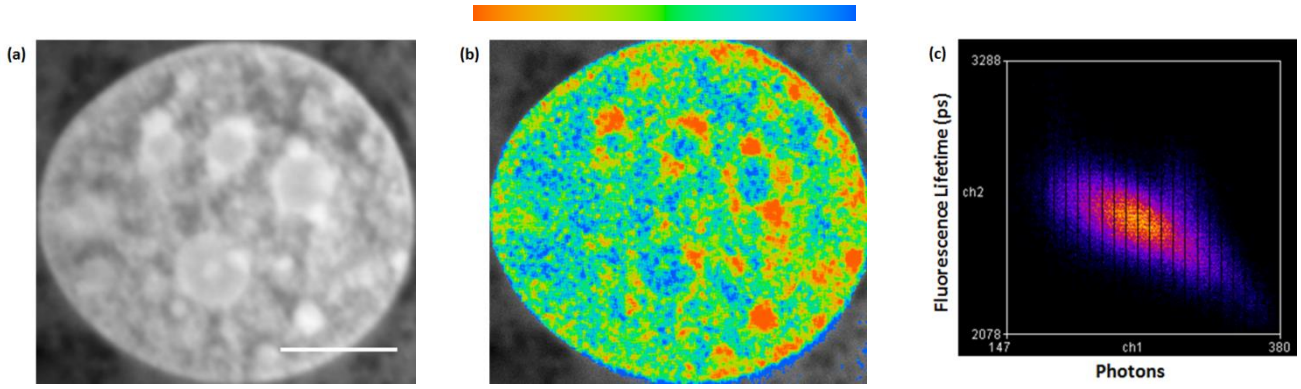

Figure 23. The intensity and lifetime images of NIH 3T3 living cells stained with Syto 13. (a) Intensity image (b) lifetime image and (c) scatter plot. The lifetimes are represented in a continous pseudocolor scale ranging from 2312-2814 ps. Scale bar, 5µm.

The investigations revealed that lifetime contrast between condensed and non-condensed regions was pronounced in the samples which were labled by Syto 16, Nuclear Violet, Hoechst 33342, Hoechst 34580, Syto 13 (see Table 18). The readouts of the investigation of potent chromatin compaction probes as well as the results for DNA characterization using FLIM-TCSPC are summerized in Table 18. The mean lifetime values were calculated from the nucleus area. Hence, among various listed DNA probes in Table 14 and 15, Hoechst 33342, Hoechst 34580, Nuclear Violet, Syto 13 and Syto 16 showed the potential to be used as fluorescence chromatin compaction probes in FLIM measurements. In the further evaluation of the chromatin compaction

assay using single organic DNA dyes the focus was put on Hoechst 34580 as one member of the bisbenzimide family excitabel with the violet 405 nm laser and Syto 13 (unsymmetrical substituted cyanine dye) as a green emitting dye excited at 488 nm.

Dye	τ_{mean} (ps)	ICQ	Model	τ (contrast) [+/-]	DNA vs. RNA staining [-/+/++]	$\lambda_{(Laser)}$ (nm)	Filter
Syto 16	2851 ±135	- 0.18	Single	+	+	445	528 BP/ 460 LP
Nuclear Violet	1017 ± 49	- 0.21	Double	+	++	405	450/70 BP/ 480 BP
Hoechst 33342	2006 ± 71	- 0.12	Double	+	++	405	450/70 BP/ 460 LP
Hoechst 34580	1204 ± 49	- 0.21	Double	+	++	405	450/70 BP/ 460 LP
Syto 13	2578 ± 123	- 0.19	Double	+	+	488	534/42 BP/ 520 LP

Table 18. The results for DNA probes characterization utilizing FLIM setup at GSI.

To demonstarte that organic DNA dyes, e. g. Syto 13 shows chromatin density changes and to compare the impact of the different HDACi, NIH 3T3 cells were treated with VPA or alternatively, TSA for 24 h. Similar to VPA, TSA is a pan- HDACi and it has been reported that TSA gives rise to inhibit cellular HDAC activity which is accompanied by modification in chromatin structure and function (75; 81). To induce chromatin compaction, NIH 3T3 cells were exposed to hypertonic medium (4 fold PBS). As control, the fluorescence lifetime was measured in normal medium without treatments. The mean lifetime value of Syto 13 was 2808 ± 28 ps (n= 30). Since the FLIM measurements for VPA/ TSA and 4 fold PBS have been done in different days, the lifetime values were normalized to the corresponding control values (Figure 24). After treatments with VPA, the measured mean lifetime of the Syto 13 had a significant increased to 2854 ± 34 ps (about 2% increase) (n= 31). The mean lifetime value was determined to be 2857 ± 34 ps (n=33) after addition of TSA similar to that after VPA treatment (Figure 24 panel (a)). The measured mean lifetime of Syto 13 was 2725 ± 31 ps (n= 23) upon chromatin compaction by hypertonic treatment (4 fold PBS; Figure 24 panel (b)). The drop in the mean lifetime value after 4 fold PBS was around 3 %. The outcomes supported that Syto 13 was sensitive to both chromatin decompaction and compaction. In summary, Syto 13 showed a dynamic range of 5 % lifetime changes and can therefore be used as chromatin compaction probe.

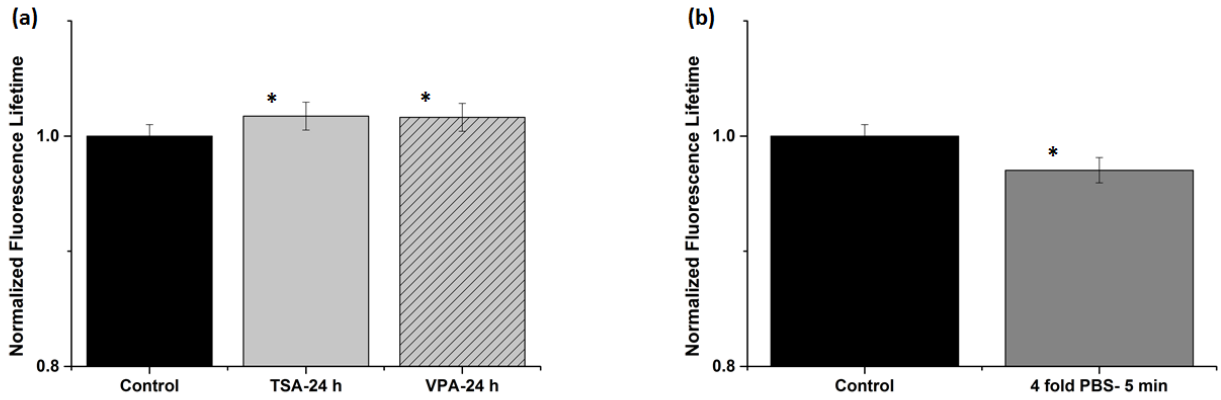

Figure 24. Modulation of the chromatin status of NIH 3T3 living cells stained with Syto 13 and evaluation by FLIM. Statistical significant changes of the lifetime of Syto 13 were observed after after VPA/ TSA (a) and 4 fold PBS (b) treatments. Asterisks show $p < 0.05$ (using t-test) compare with control. Error bars indicate mean ± SD.

Using similar procedures, FLIM measurements were carried out to analyze the dynamic range of responses of the fluorescence lifetime of Hoechst 34580 on chromatin modulation. Here, alternatively, to induce a rapid chromatin decondensation, hypoosmolar medium (0.5 PBS) was used. As control, the mean lifetime value was measured 1234 ± 10 ps (n=21). After addition of VPA, the rise in the measured mean fluorescence lifetimes of Hoechst 34580 was 1273 ± 5 ps (n= 31) which revealed the change in the lifetime value by 3 % (Figure 25 panel (a)). Whereas the treatment with the deacetylase inhibitor yielded only moderate changes in the lifetime, hypoosmolar decompaction gave rise to an enhancement of the mean lifetime value of Hoechst 34580 from 1234 ± 10 to 1428 ± 13 ps (n= 21)- corresponding to around ~ 14 % change (Panel (b)). The replacement of 0.5 PBS by normal cell medium resulted in a decrease in the mean lifetime of Hoechst 34580 again to nearly control values (1263 ± 0.8 ps) proving that the chromatin decompaction induced by hypoosmolarity was quickly reversible. Inducing a chromatin compaction by hyperosmolar medium (4 fold PBS) revealed a reduction in the lifetime of Hoechst 34580 from 1283 ± 21 ps (n=10) to 1202 ± 30 ps (n=7) (Panel (c)). The observed change was around 7 % and thus more pronounced with respect to Syto13. It is worth to note that since the FLIM measurements for VPA/ 0.5 PBS and 4 fold PBS have been performed in different days, the lifetime values were again normalized to the corresponding control values in Figure 25. All in all, the FLIM readouts validated that Syto 13 and Hoechast 34580 can be used as chromatin compaction probes. Also, they showed higher dynamic range and sensitivity compared to fluorescence proteins.

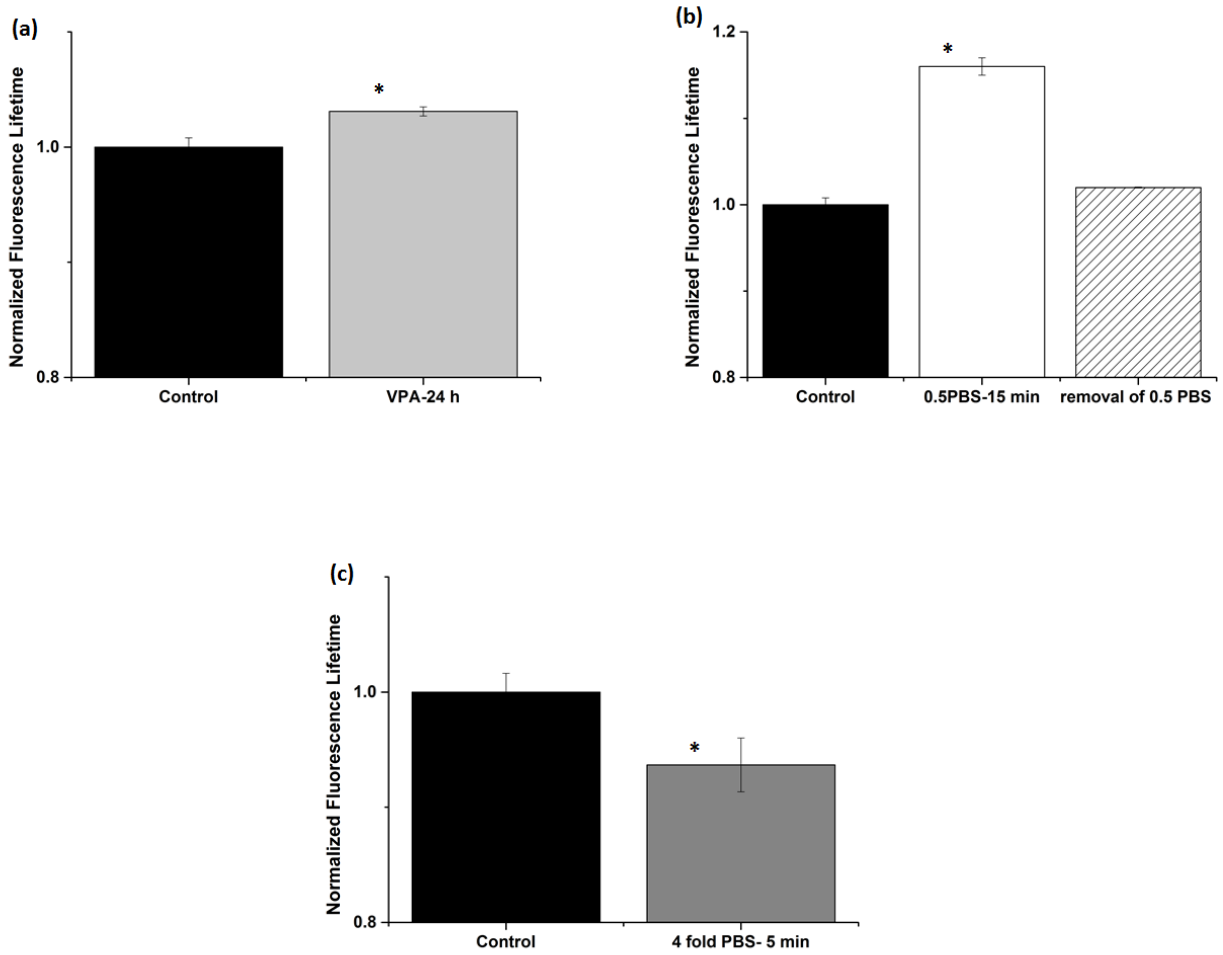

Figure 25. Manipulation of the chromatin status of NIH 3T3 living cells stained with Hoechst 34580 and evaluation by FLIM measurements. (a) Statistical significance changes of the lifetime of Hoechst 34580 after addition of VPA. (b) 0.5 PBS results in a drastic but reversible rise in the lifetime value of Hoechst 34580. (c) Statistical significance decrease of the lifetime of Hoechst 34580 after 4 fold PBS treatment. Asterisks show $p < 0.05$ (using t-test) compare with control. Error bars indicate mean ± SD.

4.2.3. Physical characterization of promising dyes and robustness of measurements

Being able to exploit FLIM measurements in living cells, it is important to understand how to choose the appropriate recording conditions. To have a reliable FLIM readout, it is known that a sufficient amount of photons in a reasonable acquisition time is a demand (24), or in other words, for a robust fitting leading to a lifetime contrast a sufficient number of photons must be collected by the FLIM detector. Although organic fluorescent dye molecules possess often higher quantum yields compared to fluorescent proteins, they are usually rapidly photobleached in the presence of the oxygen and high laser intensity (89; 90). Photobleaching has been reported to be a critical issue in the use of organic dyes in bioanalaytical applications, in particular, for measuring dynamic changes and real-time imaging applications (89). To minimize the contribution of photobleaching but accumulate enough photons within a reasonable recording time, the laser power was

adjusted to obtain count rates in the order of 10^5- 10^6 photons/s. In the used system, the laser power in FLIM scanner can be modified optically by rotating filter wheels equipped with a neutral grey density ramp in the arbitrary range 1 to 10. These wheels are located in the scanner head between fibre-coupling of the lasers and the central beamsplitter or laser combiner, respectively. It should be noted that this way of opticaly attenuation retains the laser pulse shape unchanged in contrast to a modulation of the laser power itself, which can be performed by the B&H software (24). The output power of our available lasers has been measured. For example, the measurement of the output power of the 405 nm ps diode laser after the 60x/1.2 NA water immersion objective lens of the FLIM microscope is shown in Figure 26. As seen, increasing the filter wheels from 1 to 10 showed an exponential rise in the output power of the laser in the range of 0.02 to 33.00 µW.

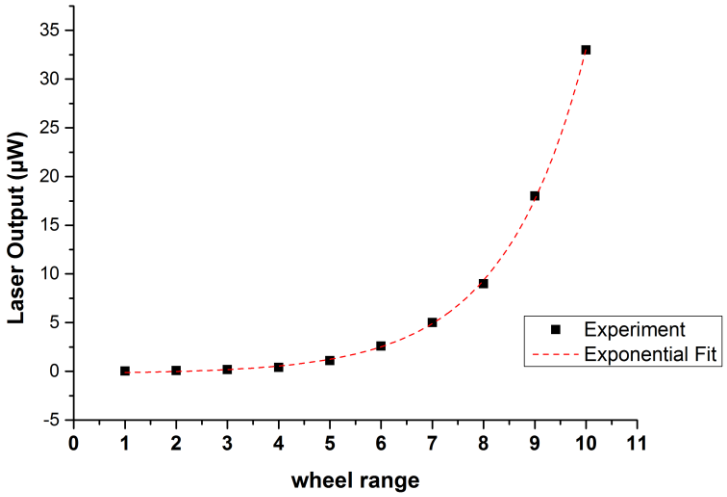

Figure 26. Output power measurement of 405 nm ps diode laser.

To study the photostability as requirement for prolonged kinetics measurements of the promising chromatin compaction probes, the repetitive recordings have been performed at scanning cycles of 10 s each using 2.60 and 9.00 µW of 405 nm laser-power. It is worth to highlight that FLIM measurement using 33.00 µW gave rise to overload the detector because of the high number of photons especially coming from bright areas (chromocenters). Figure 27 panels (a) and (b) compared the fluorescence intensity and lifetime of living NIH 3T3 cells stained with Hoechst 34580. As seen in Figure 27 panel (a), a progressive decay down to around 60 % of the initial value was observed for the 9.00 µW, as compare to 2.60 µW laser power settings, which showed around 80 % of the initial value of the fluorescence intensity of Hoechst 34580 after 10 cycles. In contrast, the fluorescence lifetime of Hoechst 34580 was only slightly affected by photobleaching (see Figure 27 panel (b)).

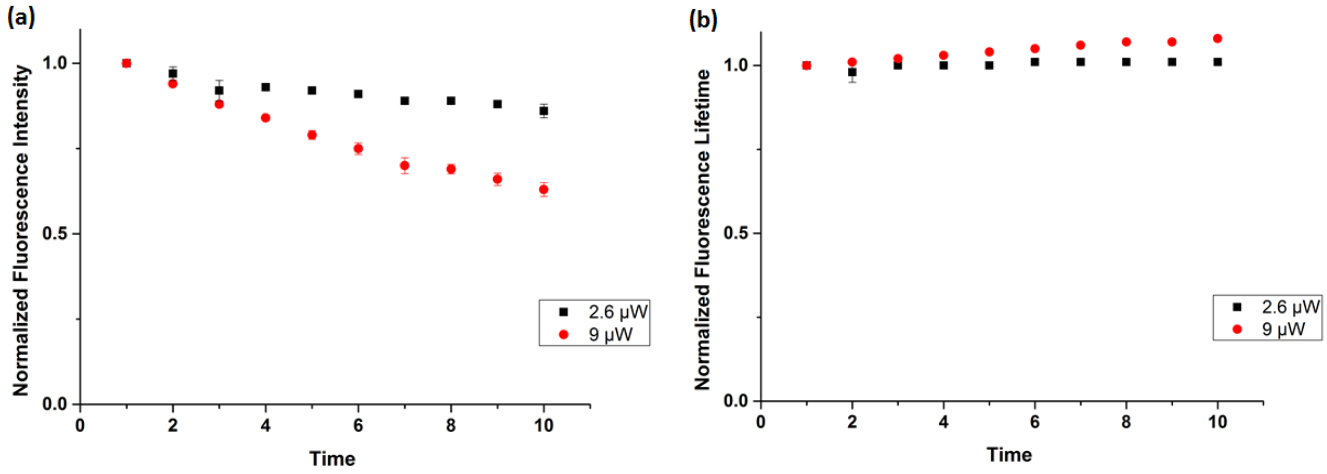

Figure 27. Photostability of Hoechst 34580 using 2.60 µW and 9.00 µW laser power. The fluorescence intensity (a) and lifetime (b) were normalized to the intensity and lifetime of the first aquisition cycle of 10 s. The horizontal axis represents number of cycles each integrating for 10 s. Number of analysed cells, n=5. Error bars represent mean ± SD.

To test also the impact of the laser setting on the lifetime contrast, FLIM measurements of living NIH 3T3 cells stained with Hoechst 34580 using 2.60 and 9.00 µW laser power setting as well as 20 s acquisition time (to have sufficient photons) have been done. The reduction of the laser power to 2.60 µW still yielded sufficient photons and did not have a significant impact on the lifetime distribution. It must be noted that, in case of insufficient numer of photons, the pinhole setting of FLIM scanner can be adapted sacrifizing depth resolution or, alternatively, the recording (cycling) time can be increased.

4.3. Application of chromatin compaction assay in radiation biology

As mentioned, the repressive environment of HC makes the processing of HC - DSBs and the maintenance of genomic stability a challenging task for the cellular repair system after a radiation insult. Previously, to address the question of heterochromatic DNA accessibility and damage recognition, the targeted single ion irradiation at the GSI microprobe was applied to generate strictly localised DSBs directly within constitutive murine HC compartments (chromocenters) (9; 18). Besides a fast damage response indicated by the recruitment of repair proteins into HC and the phosphorylation of H2AX inside the chromocenter, a fast local decondensation of the HC at the sites of ion traversal was observed, both arguing against the hypothesis of a generally limited accessibility of damage response proteins to HC. The radiation-induced decondensation is accompanied by a relocation of the induced DSBs to the adjacent euchromatin (EC) (9; 18), which might be a requirement for subsequent DNA repair. It is unknown, if the decondensation itself is the driving force for the observed damage relocation. Whereas the radiation-induced decondensation can readily be observed in fixed samples after charged particle radiation, it proved difficult to reveal these changes using intensity based measurements in living cells. Therefore, FLIM has been employed as a promising alternative technique in the present study. The present sections aim to observe chromatin decompaction after ion/X-rays irradiation utilizing FLIM-TCSPC.

4.3.1. Repositioning and targeted irradiation of offline preselected single cell nuclei

So far, using single organic DNA dyes as chromatin compaction probes in FLIM, the osmotic/ enzymatic induced chromatin changes could clearly be detected by significant changes in fluorescence lifetime values. To investigate radiation-induced chromatin decompaction in living cells based on these chromatin compaction probes characterized in the chapters before, an experiment at the GSI microprobe facility was performed. To do so, multiple repositioning between the FLIM setup and the GSI microprobe for targeted irradiation of chromocenters was necessary. In order to find conditions for revisiting individual cells, following procedure was optimized and established allowing to perform repetitive FLIM measurements.

Prior to irradiation, 4 to 12 single nuclei from the two to four field of view in a dish showing well distinguishable chromocenters in the FLIM signal of Syto 13 were selected. By the aid of a precise sample holder and coordinate transfer the nuclei were repositioned at the microprobe where the targeted irradiation with individual gold ions (4.5 MeV/u) took place. The precision of the repositioning procedure was in the order of 100 µm, limited by the mechanical accuracy of the sample holders. To correct for this imperfect repositioning, images of the selected nuclei served for identification. After targeted irradiation at the positions indicated by the red crosses, cells were transferred to the FLIM setup again, repositioned and a post-irradiation FLIM image acquired. Cells were subsequently fixed and immunostained for a DSBs marker, e.g. 53 BP1, for hit verification. The chromatin of the fixed NIH 3T3 cells was restained with 1 µM DAPI. Figure 28 panel (a) and (b) showed an example of intensity and lifetime images of the preselected nuclei before iradiation. The hit chromocenters have been shown by red crosses in panel (c). Panel (d) and (e) represented

intensity and lifetime images of preselected cell approximately 35 minutes post-irradiation, respectively. The intensity image of damage marker was depicted in the panel (g). The measured mean lifetime of Syto 13 before irradiation was 2515 ± 170 ps and was reduced to 2466 ± 153 ps after irradiation. In addition, a slight shrinkage of the nucleus could be observed. Surprisingly, high background staining of the damage marker 53BP1 precluded the hit verification (panel (g)). The absence of the hit chromocenters in DNA intensity images (also after fixation, panel (f)) points to either problems of hitting accuracy in that experiment or damage relocation due to the long time between irradiation and recording.

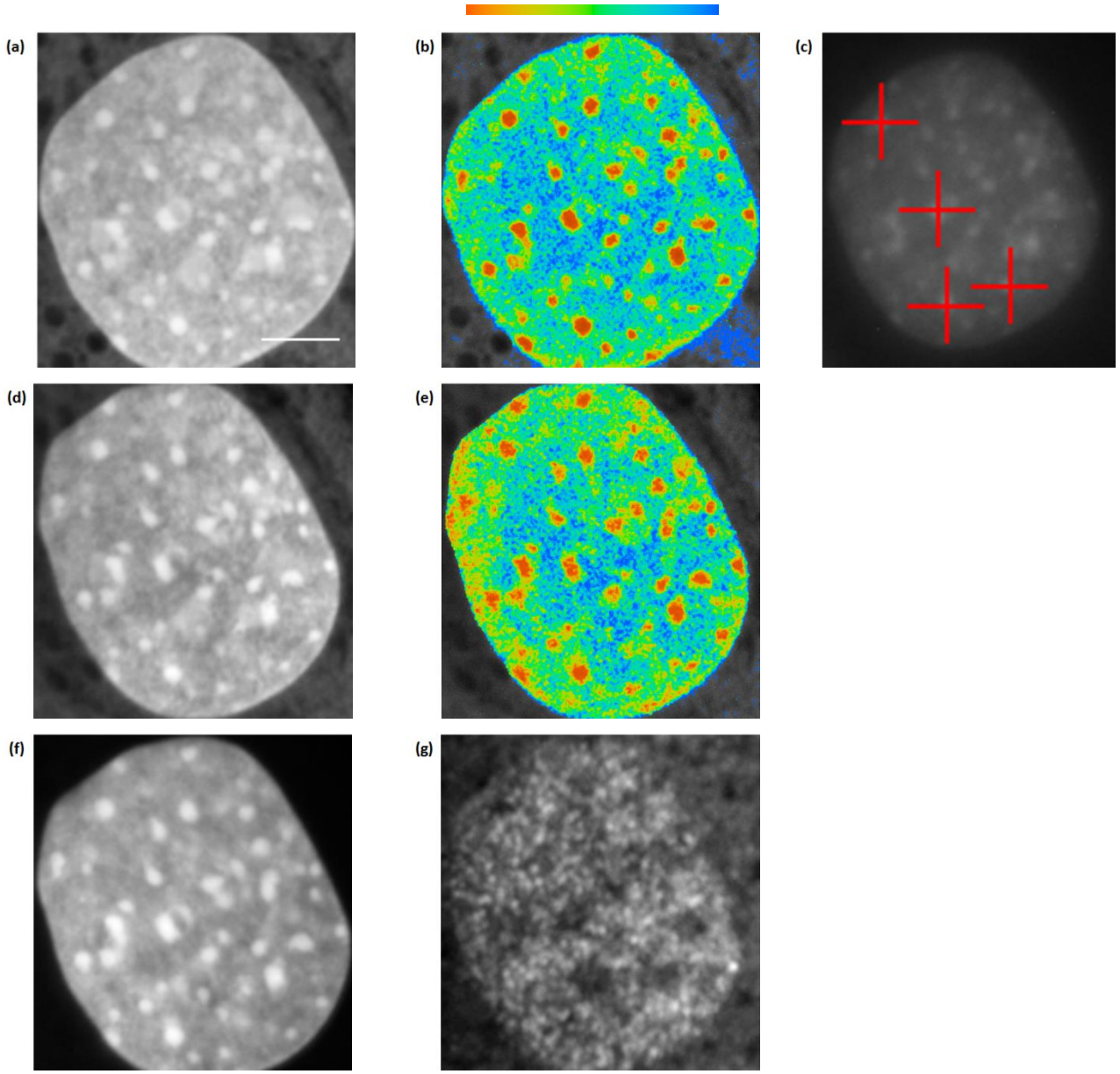

Figure 28. Fluorescence lifetime imaging of preselected and irradiated NIH 3T3 cell stained with Syto 13. Intensity (a) and lifetime (b) images of living NIH 3T3 cell before irradiation. Targeted chromocenters (red crosses) at the microprobe is shown in (c). Intensity (d) and lifetime (e) images of repositioned cell after offline irradiation using gold ions 4.5 MeV/u). (f) Intensity images of preselected cell after fixation and restaining with DAPI. Intensity image at 640 nm excitation of preselected cell after fixation and immunostaining of the repair protein 53 BP1 (Atto 647) (g). In both cases, the fluorescence lifetime were presented in the same continous pseudocolor scale ranging from 2063 to 2800 ps. Scale bar, 5µm.

Similar results were obtained by multiple repositioning between our FLIM setup and the GSI SIS accelerator. Living NIH3T3 cells (n=53) stained with Syto 13 were irradiated by xenon ions (600 MeV/ nucleon, LET: 750 keV/µm) and images of 21 nuclei were of sufficient quality to be analyzed. Figure 29 panel (a) and (b) show an example of intensity and lifetime images of a NIH 3T3 cell stained with Syto 13 before irradiation. The measured mean lifetime of Syto 13 before irradiation was 2734 ± 140 ps. As described previously, after

irradiation, cells were transferred to the FLIM setup again, repositioned and a post-irradiation FLIM image acquired (panel (c) and (d)).

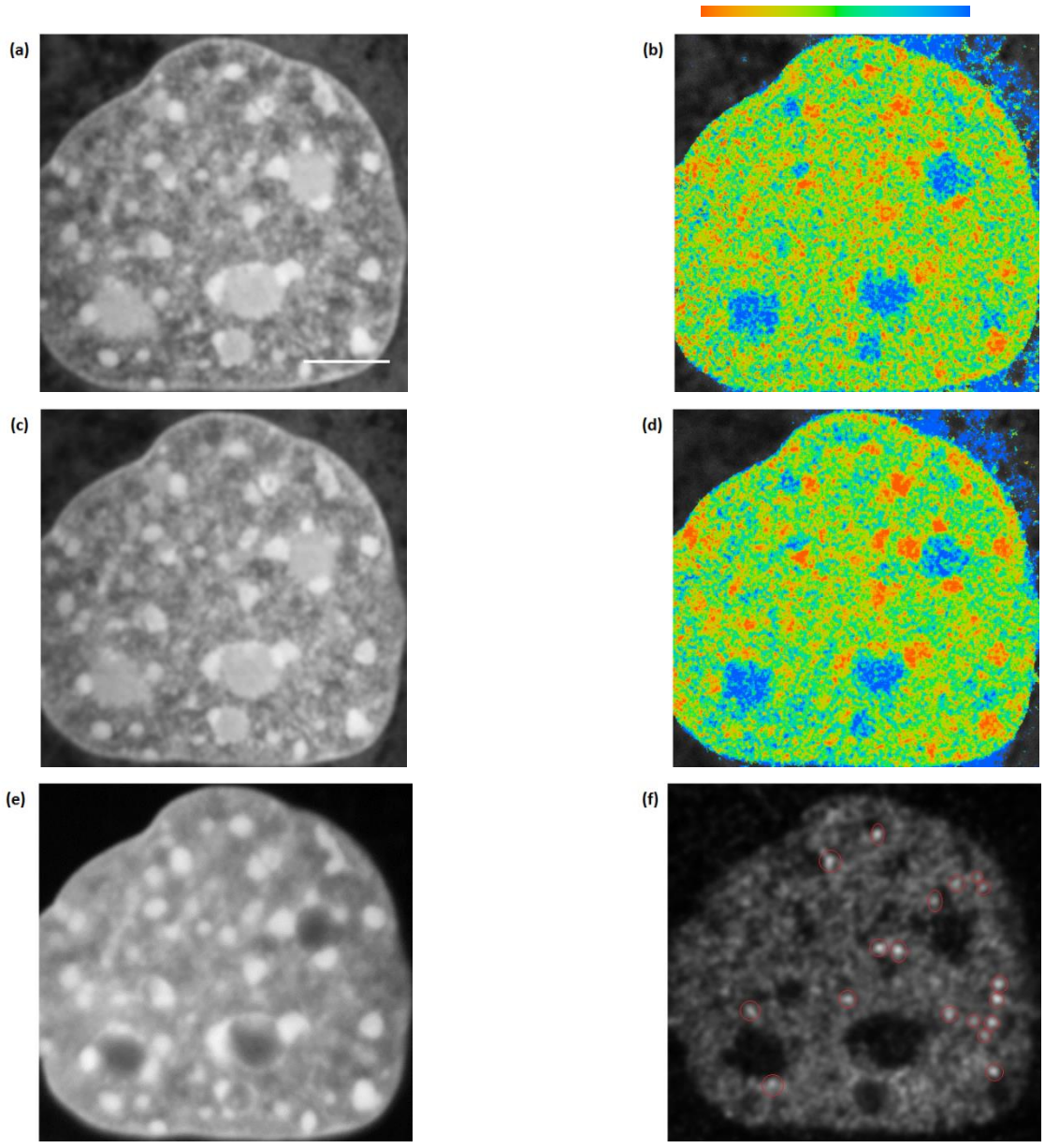

Figure 29. Fluorescence lifetime imaging of preselected and irradiated NIH 3T3 cell stained with Syto 13. Intensity (a) and lifetime (b) images of living NIH 3T3 cell before irradiation. Intensity (c) and lifetime (d) images of repositioned cell after offline irradiation using xenon ions (600 MeV/u) at the SIS accelerator. Intensity images of preselected cell after fixation and restaining of DNA with DAPI (e). Intensity image at 640 nm excitation of preselected cell after fixation and immunostaining of the repair protein 53 BP1 (Atto 647) (f). Potential sites of damage induced by ion traversals are marked by red circles. Scale bar, 5µm.

The measured mean lifetime value of Syto 13 was reduced to 2603 ± 131 ps after irradiation. The duration of aformentioned procedure was about 30 to 40 minutes. The immunostaining after post-irradiative fixation

shows 18 small 53 BP1 foci (panel (f)). The intensity image in the panel (e) showed the same nucleus which was restained with DAPI showing a similar bright nuclear staining like Syto 13 although the absence of RNA/ nucleoli staining can be observed.

4.3.2. Irradiation with heavy ions at the beamline microscope

As mentioned previously, the discrimination between lifetime of the condensed and non-condensed areas plays a fundamental role in the quantification of the chromatin condensation status in living cells. Since Nuclear Violet revealed a higher lifetime contrast and an even more pronounced ICQ value of - 0.21 (vs. - 0.19 see Table 18) with respect to Syto 13, Nuclear Violet was used as chromatin compaction probe in the following beamtime experiments. NIH 3T3 -53BP1- mCherry were stained with Nuclear Violet and irradiatied at GSI UNILAC accelator with a broad beam of carbon ions (4 MeV/nucleon, fluence: 5.10^6 cm^{-2}). 53BP1-mCherry transfection of the cells was done to detect DSBs by the generation of repair foci during and after irradiation in real time, without necessity to fix and immunostain the samples. Exemplarily, Figure 30 shows the intensity and lifetime images of Nuclear Violet in NIH 3T3 cells before and after ion irradiation. A continous pseudocolor scale ranging from 1610 to 2074 ps represents the differences in Nuclear Violet fluorescence lifetime. The mean fluorescence lifetime values of 1915 ± 108 ps and 1907 ± 105 ps were measured pre/ postirradiation. Unexpectedly, there was no indication of an ion irradiation neither in chromocenters nor in the surrounding euchromatin. Further follow-up experiments revealed that although Nuclear Violet represents a pronounced lifetime contrast between condensed and non-condensed areas, it is a very photo-toxic DNA dye which disturbs normal cellular behavior including the formation of radiation- induced formation of localized repair foci (data not shown).

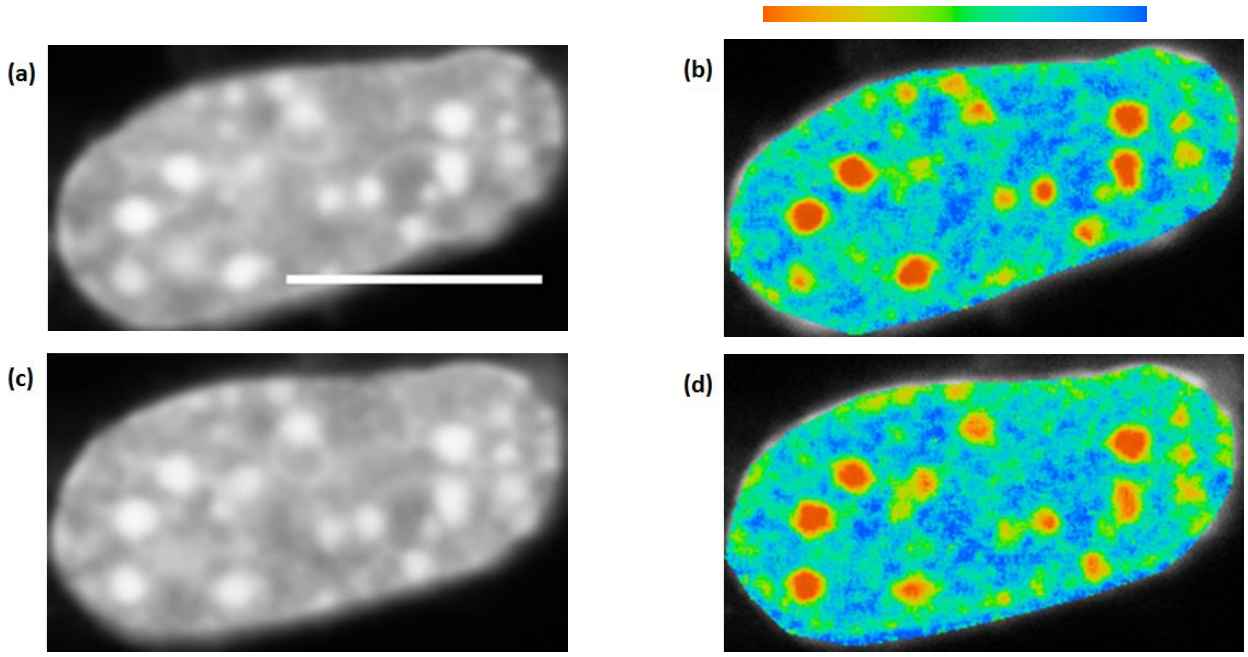

Figure 30. Intensity and lifetime images of NIH 3T3 -53BP1- mCherry cells stained with Nuclear Violet. Panel (a, b) shows FLIM measurement of nucleus before irradiation. Panel (c, d) shows FLIM measurement of the nucleus after irradiation.

4.3.3. Irradiation with heavy ions and subsequent fixation combined with FLIM measurements

So far, by applying offline and online irradiation, unfortunetly, no radiation-induced changes in the heterochromatic regions in the living cells could be detected. However, in fixed cells a fast local decondensation of the HC at the sites of ion traversal had been described after charged particle radiation (9; 18). In these studies, a depletion in the intensity of DNA bound dyes had been observed. Hence, to demonstrate the general feasibility of FLIM experiments on radiation-induced chromatin decompaction in murine cells, living NIH 3T3 cells were irradiated with uranium ions (4.7 MeV/nucleon, LET: 15000 keV/µm) and subsequently fixed, immunostained and labelled with chromatin compaction probes for subsequent FLIM measurements. Figure 31 shows two examples of FLIM recordings of NIH 3T3 ells stained with Hoechst 34580 after fixation. The intensity images are shown in the panel (a) and (d) whereas the lifetime images were depicted in panel (b) and (d). The fluorescence lifetime is depicted in the continous pseudocolor scale ranging from 1170 to1472 ps. The intensity images of Alexa 514 coupled secondary antibody bound to XRCC1 as radiation damage marker are shown in panels (c) and (f). An ion traversal could be unambiguously identified inside a chromocenter (red rectangular). As shown in Figure 31, Hoechst 34580 signals were depleted at the site of a heterochromatic ion hit. The decrease in Hoechst 34580 intensity corresponds to a pronounced local raise in the lifetime. The ion hit site was marked by repair protein XRCC1 and immunustained with Alexa 514.

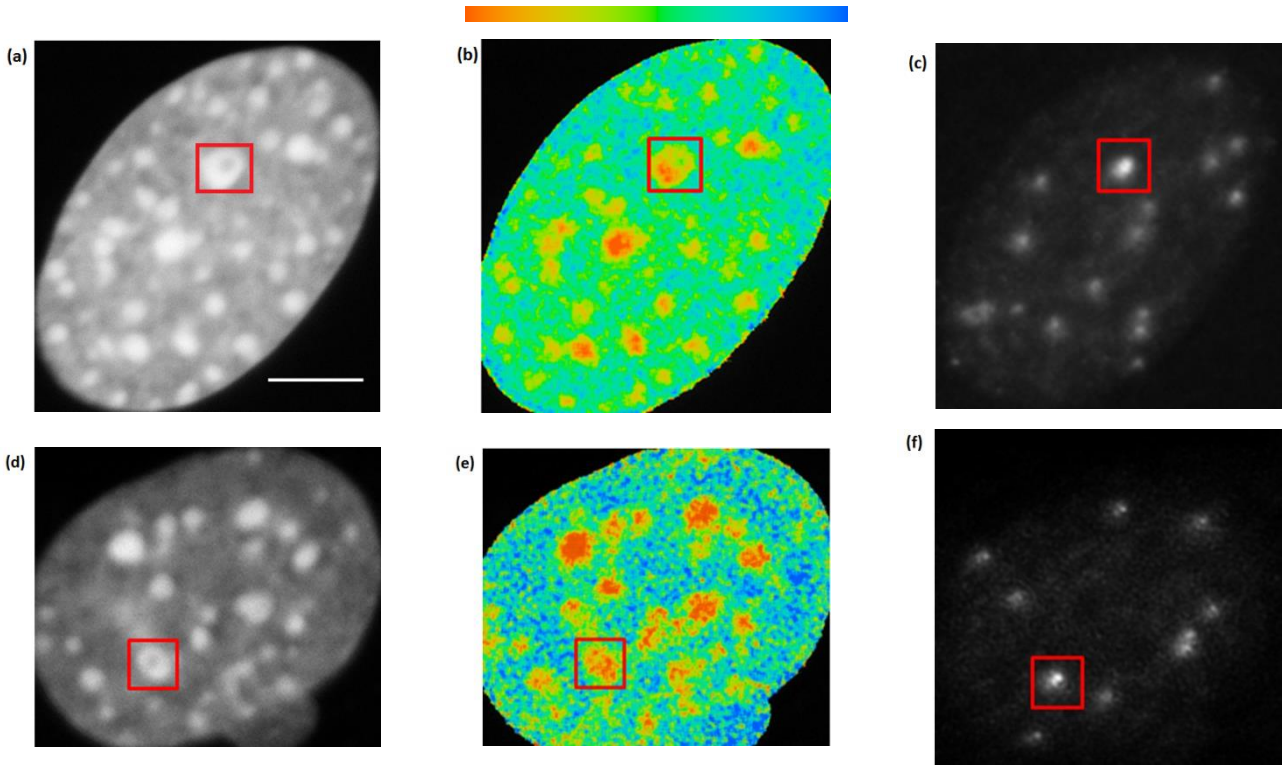

Figure 31. Decompaction of heterochromatic DNA in NIH 3T3 chromocenters traversed by heavy charged particles ions. Intensity and lifetime images of ion hit chromocenters of fixed NIH 3T3 cells stained with Heochst 34580 are depicted in pannel (a, d) and pannel (b, e), respectively. Intensity images of ion hit site marked by repair protein, XRCC1 and immunostained with Alexa 514 are shown in pannel (c, f). The heterochromatic ion hit chromocenter enclosed in the solid red rectangular (52; 91). Scale bar, 5µm.

To assess quantitavely, profiles in form of radial angel integration around of the site of the heterochromatic ion traversal were calculated. Figure 32 shows the quantitative analysis of hit chromcenter (shown in panels (a), (b) and (c)) in which the pronounced peak in fluorescence lifetime (~ 1230 ps) goes along with the local depletion in heterochromatic fluorescence intensity (52).

Consistent with aforementioned readouts, quantitative assessment of the ion hit chromocenter in Figure 31 (lower row), revealed a raise in fluorescence lifetime (~ 1270 ps) in parallel with the local depletion in the heterochromatic fluorescence intensity. Therefore, in fixed cells at least shortly after irradiation, the depletion in the intensity goes along with an increase in the lifetime demonstrating that single organic dyes in combination with FLIM detection can be used to address radiation induced chromatin changes.

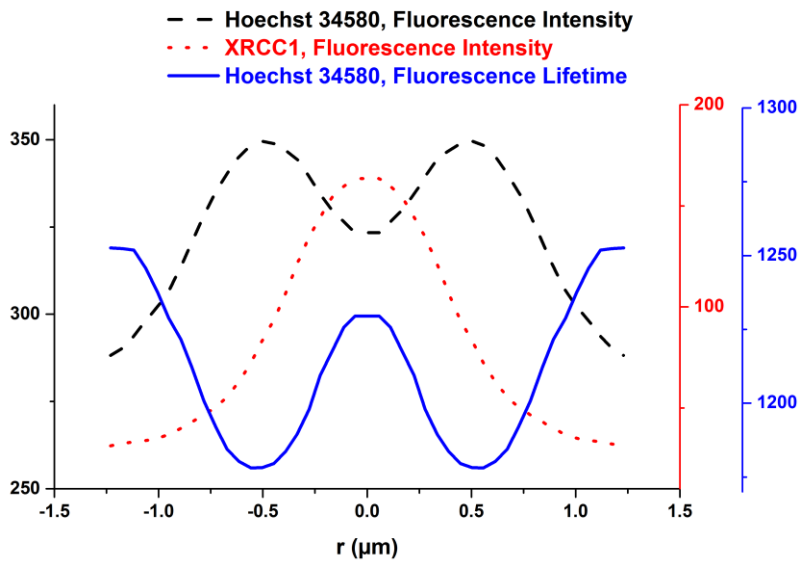

Figure 32. Quantitative assessment of the ion hit chromocenter. (Shown in the upper row of Figure 31). Intensity and lifetime profiles depict depleted DNA staining intensity and the raise in lifetime (intensity: dash; lifetime: solid) at the damage site marked by XRCC1 (dot) (52).

4.3.4. Irradiation with X-rays in combination with live cell FLIM measurements

After the successful demonstration of radiation-induced chromatin relaxation after post-irradiative fixation utilizing FLIM, the online broad beam irradiation experiments should be repeated using the adapted protocols. However, unfortunetly, the lack of beamtime excluded further investigations. As alternative and to monitor chromatin compaction changes induced by sparsely ionizing radiation in living cells, the FLIM setup was coupled to a 35 kV X-rays tube.

As repetitive measurements could lead to a minor change in the fluorescence lifetime, two subsequent FLIM measurements were carried out for each nucleus also in unirradiated controls. The FLIM measurement procedure can be summarized as follows: NIH 3T3 cells nuclei were randomly selected and the coordinats of them were stored (Figure 33 panel (a)). Afterwards, the lifetime images were recorded. The quantitative change of repetitive FLIM recordings on the fluorescence lifetime of Hoechst 34580 is shown in panel (b). The mean fluorescence lifetime value was 1228 ± 55 ps (n=50) in the first compared to 1241 ± 42 ps (n=50) in the second measurement. As absolut lifetime values varied between different dishes/days (data not shown) presented lifetime changes were normalized to the fluorescence lifetime of the first round. The result validated that the repetitive FLIM measurements only had a minor impact (< 0.5 %) on the measured fluorescence lifetime under the applied conditions, which was a prerequisit for monitoring small radiation induced changes.

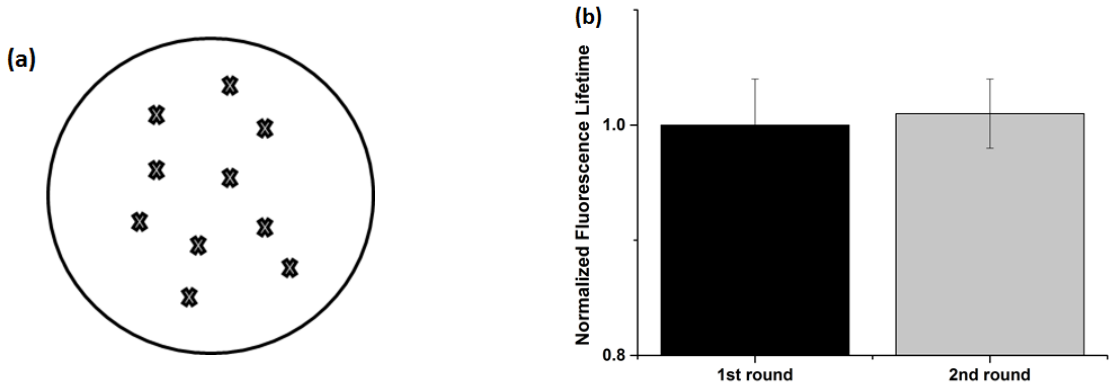

Figure 33. Successive FLIM measurements of NIH 3T3 living cells stained with Hoechst 34580. Panel (a) randomly selected living NIH 3T3 cells seeded in the glass bottom petri dish. Panel (b) represents the mean values of the fluorescence lifetime of Hoechst 34580 normalized to the lifetime of the control nuclei from two independent experiments (n=50). Error bars indicate mean ± SD.

To determine the additional changes introduced by ionizing radiation, selection and pre-irradiation FLIM imaging of different NIH 3T3 nuclei stained with Hoechst 34580 was done as described above. Following an irradiation of 10 Gy X-rays (35 kV, dose rate of 1 Gy/s), repositioning and FLIM recording of the preselected nuclei were performed. The recordings were done 1 to 20 minutes post-irradiation. A comparison of the nuclear wide mean fluorescence lifetime values of Hoechst 34580 for pre and post irradiated nuclei using t-test revealed a significat difference ($p < 0.05$) from 1205 ± 32 to 1228 ± 35 ps (Figure 34).

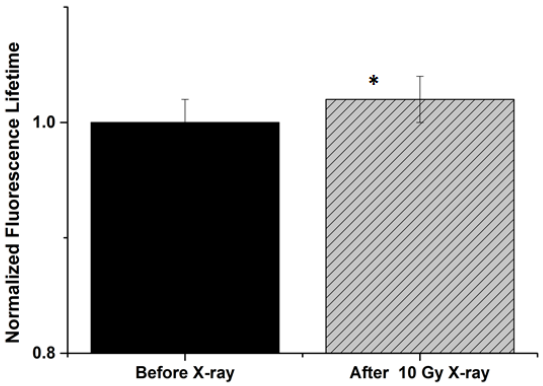

Figure 34. 10 Gy X-rays irradiation of NIH 3T3 living cells. A significant increase in the lifetime of Hoechst 34580 was shown. Data represented the mean value of the fluorescence lifetime of Hoechst 34580 normalized to the lifetime of the pre-irradiated nuclei from two independent experiments (n=48). Asterisk shows $p < 0.05$ (using t-test) compare with pre-irradiated nuclei. Error bars indicate mean ± SD.

Figure 35 shows exemplarily an example of NIH 3T3 cells nuclei before and after 10 Gy X-rays. Whereas the intensity images (panels (a) and (c)) did not show any major changes in the chromatin structure, the fluorescence lifetime of Hoechst 34580 (panels (b) and (d)) indicated by pseudocolor coding revealed that the observed shift from 1182 to 1239 ps after 10 Gy X-rays irradiation was not arising from locally confined changes, but rather effect the whole nucleus globally. This observation was also supported by the shift of the whole lifetime distribution shown in Figure 36.

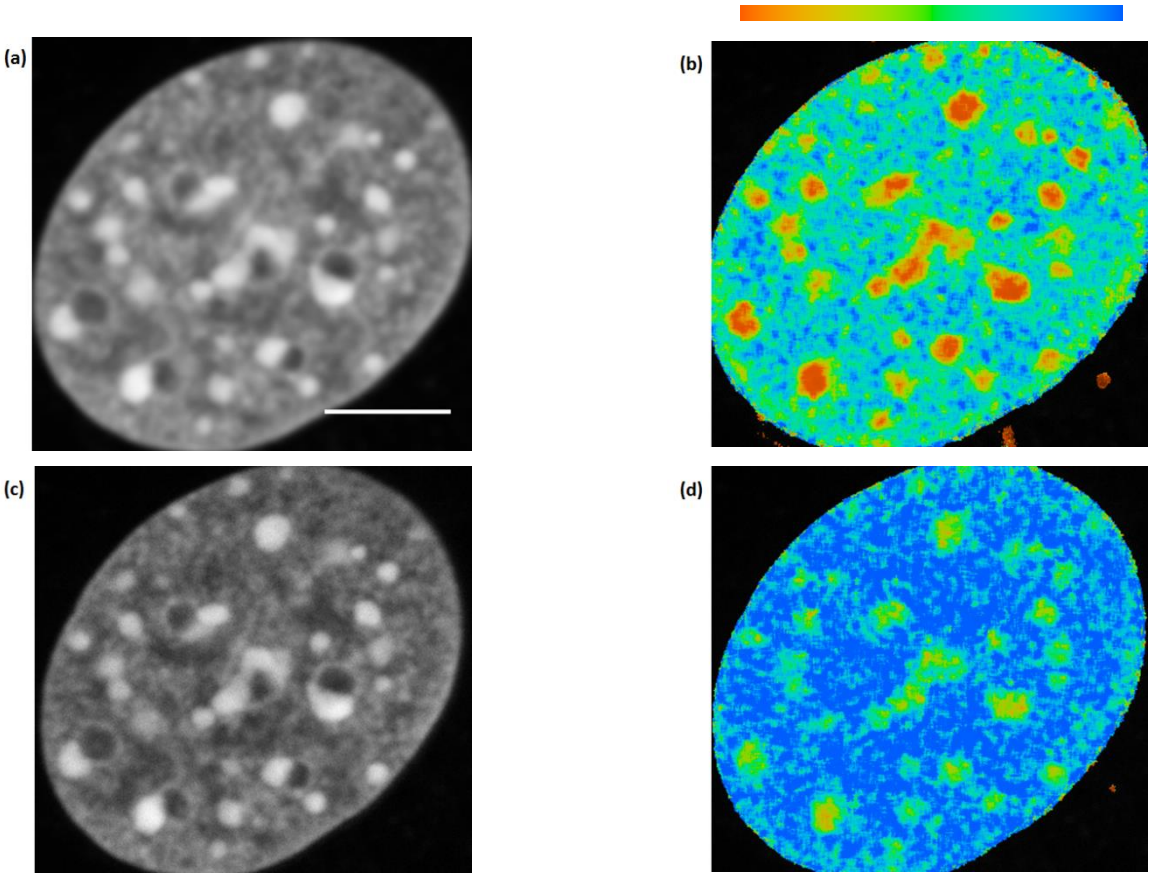

Figure 35. Intensity and lifetime images of NIH 3T3 living cells (a) before and (b) after 10 Gy X-rays irradiation. The lifetime image (panel (b)) indicates a global shift in the lifetime of the Hoechst 34580. Scale bar, 5µm.

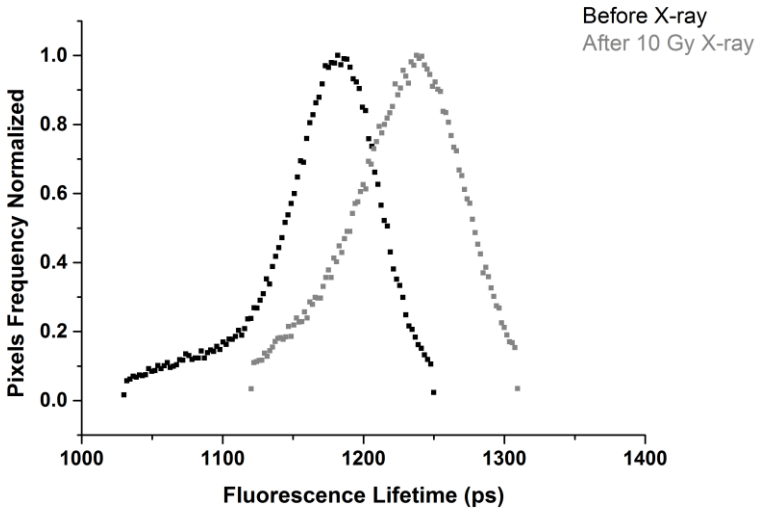

Figure 36. The mean lifetime distribution curve of Hoechst 34580 for pre-iradiated nucleus (black) and post-irradiated nucleus (gray). The shift of the whole lifetime distribution (gray) validates the global radiation-induced changes in chromatin structure.

4.3.5. Other applications of the chromatin compaction assay

It has been spaculated that the non-cycling G_0-phase cells likely possess a state of more condensed chromatin with respect to the proliferating G_1-phase cells (92; 93). So, to address if any chromatin compaction lifetime change can be observed in non-cycling G_0 cells compared to cycling cells in G_1, our newly eshtablished chromatin compaction probe has been employed in normal human fibroblasts under different cultivation conditions. FLIM measurements of normal human diploid human fibroblasts (AG1522D) nuclei stained with Hoechst 34580 were carried out. Figure 37 shows the quantitative changes of fluorescence lifetime values of Hoechst 34580 for cycling G_1 vs. non-cycling G_0 cells. A reduction of the mean lifetime value of 10 days seeded G_1 cells (n= 49, intermediate state) and more pronounced for non-cycling G_0 cells (n= 84) was observed compared to G_1 cells (n= 19) seeded 3 days before the measurement.The reduction of the lifetime values of Hoechst 34580 between 3 days seeded G_1 cells (n= 19) and non-cycling G_0 cells (n= 84) was significant. The measured mean lifetime values of Hoechst 34580 were listed in Table 19.

Cell Cycle	τ_m (ps) ± SD
cycling growing G_1 cells (3 days)	1189 ± 34
cycling growing G_1 cells (10 days)	1157 ± 58
non-cycling G_0 cells (21-days)	1151 ± 39

Table 19. The summary of measured mean lifetime values of Hoechst 34580 in cycling G_1 and non-cycling G_0 cells. Errors represent mean ± SD.

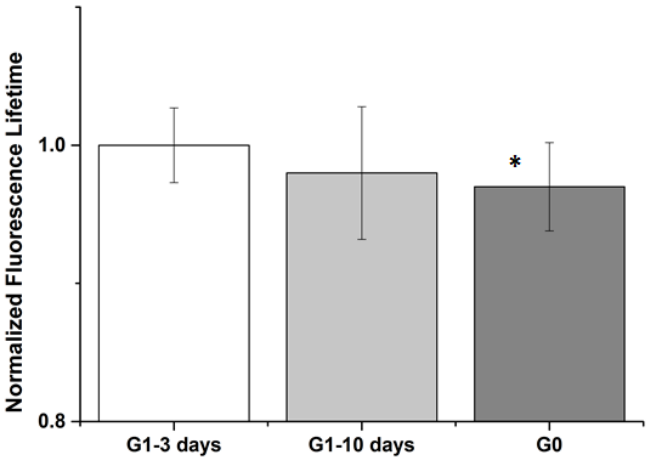

Figure 37. Comparison of the mean lifetime values of Hoechst 34580 in cycling G_1 and non-cycling G_0 cells using our newly established chromatin compaction assay. Asterisk shows significance at $p< 0.05$ (using t-test) compared to cycling G_1 cell (3 days) nuclei. Error bars indicate mean ± SD.

Besides, in an independent FLIM experiment of AG1522D stained with Hoechst 34580, the mean lifetime values of 3 days seeded G_1 cells (n= 55) and 10 days seeded G_1 cells (n= 55) were compared (Table 20) to confirm, that the 10 days culture already shows a transitional state towards chromatin compaction in resting cells. As seen in Figure 38, the result showed the significant reduction of mean lifetime values of Hoechst 34580 from 3 days seeded G_1 cells to 10 days showing the transition towards quiescence.

Cell Cycle	τ_m(ps)± SD
cycling growing G_1 cells (3 days)	1149 ± 25
cycling growing G_1 cells (10 days)	1137 ± 26

Table 20. The summary of measured mean lifetime values of Hoechst 34580 in cycling growing G_1 (3 and 10 days). Errors represent mean ± SD.

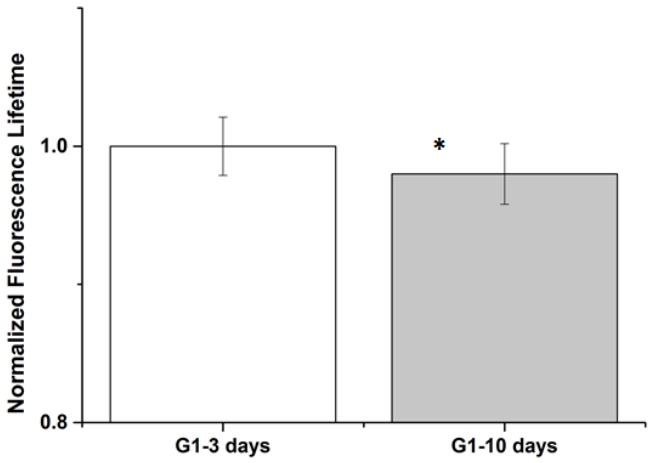

Figure 38. Comparison of mean lifetime values of Hoechst 34580 in 3 days and 10 days seeded cycling growing G_1 cells using our newly established chromatin compaction probes. Asterisk shows $p< 0.05$ (using t-test). Error bars indicate mean ± SD.

Using our FLIM setup, a small (3.2 %) but significant change in the mean lifetime of the compaction sensor in resting G_0 cells versus cycling human fibroblasts cells in the G_1 phase of the cell cycle has been demontrated. Moreover, to check for different chromatin compaction in interphase nuclei during the cell cycle of proliferating cells, FLIM measurements of U2OS-G_1/S-GFP NBS1-mCherry cells (human osteosarcoma cells), have been performed. This cell line includes a marker to discriminate G_1 and S/G_2-phase cells. The readout of mean lifetime values of chromatin bound Hoechst 34580 showed a small but significant difference between G_1-phase (n=46) compared to S/G_2-phase (n=36) nuclei (Figure 39). Measured values are summarized in Table 21.

Cell Cycle	τ_m(ps)± SD
G_1	1169± 33
S/G_2	1183± 31

Table 21. The summary of measured mean lifetime values of Hoechst 34580 in G_1 and G_2 cells. Errors represent mean ± SD.

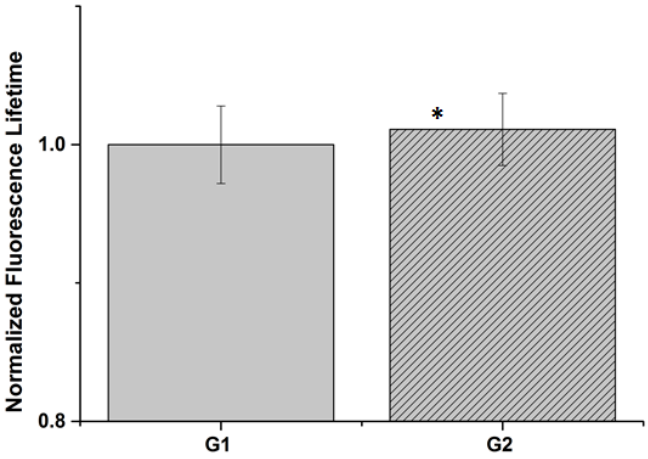

Figure 39. Comparison of the mean lifetime values of Hoechst 34580 in cycling growing G_1 and G_2 cells using the newly established chromatin compaction assay. Asterisk shows significance $p < 0.05$ (using t-test). Error bars represent mean ± SD.

5. Discussion

Many regulated biological processes in the nucleus like gene expression/ transcription, differentiation, senescence and even in the development of human cancer are governed by chromatin compaction (94). Thus, the necessities to develop and improve a method to study the chromatin compaction arise from its widespread roles in biology and human diseases. So far, different approaches have been used to elucidate chromatin structure, e.g. nuclease digestion assay (95; 96), DNA denaturation using Acridine Orange in fixed cells (97) or intensity based measurements (98). Meanwhile, especially recently also fluorescence lifetime imaging microscopy has been employed to study chromatin structure by other groups (38; 66; 75; 76; 99; 100).

A number of studies have addressed the protective role of chromatin compaction on radiation-induced double strand breaks (101; 102; 103; 104). Using UV laser microirradiation, a rapid chromatin decondensation at the sites of laser microirradiation-induced DNA damage has been verified (105; 106). Moreover, several experimental indications of radiation-induced chromatin decondensation have been found (107; 108; 109). Recently, the observation of the remarkable depletion in the intensity of the DNA dye, 4', 6-Diamidin-2-phenylindol (DAPI), at heterochromatic ion hits after fixation indicating a local decondensation of the densely packed heterochromatin (9). Attempts undertaken to measure the dynamics of this chromatin decondensation in living mouse cells based on the drop in the intensity of the live cell DNA stain Hoechst 33342 after broad beam or targeted irradiation revealed a time course of seconds to minutes post-irradiation. The duration of this radiation-induced DNA decondensation indicates a yet undefined biological process distinct from a direct radiation-induced physico-chemical alteration of the molecular structure of the DNA which might be necessary to open up the space for subsequent recruitment of further repair factors and repair (9; 18). The mentioned studies (9; 18) relied on the strictly localized dose deposition of low energy charged particles (14; 15) as well as the pronounced DNA staining of heterochromatic pericentromeric repeats, which are organized in so called chromocenters in the murine cell system, in turn, allowing an easy identification of heterochromatin in the microscope.

However, this intensity based chromatin decondensation measurements in living cells suffer from only moderate irradiation induced changes, the influence of staining variability and the intrinsic problem of not being able to discriminate between chromatin decondensation and a reduction of available dye binding sites mimicking a decompaction. Thus, a more sensitive readout, which is independent of intensity information and functional in live cell measurements, is highly desirable. As fluorescence lifetime is considered to be unsusceptible to variations in staining intensity or changes in dye concentration, this method was investigated in this thesis as an alternative approach of chromatin decondensation measurement. The FLIM system was integrated in an existing setup, which can be coupled to an external X-rays source (Figure 9) or directly used at the GSI beamline (Figure 11). This new tool should allow to address the spatiotemporal dynamics of heterochromatic decondensation processes during irradiation with higher sensitivity and (together with molecular biological measurements) to pinpoint the biological mechanism and consequences of this radiation induced chromatin changes in future studies.

5.1. Comparision of genetically encoded FRET sensors and single organic dyes in live cell measurements

To assess the sensitivity of chromatin sensors upon modification of chromatin compaction, the FLIM-FRET assay was applied to the HeLa$^{H2B\text{-}2FP}$ cell line. A preivious study demonstrated a decrease in the lifetime of H2B-GFP in the present of these cells co-expressing H2B- mCherry due to the occurance of FRET (75). The FLIM-FRET measurements with the GSI setup are in accordance with these published results as a significant decrease in the measured mean lifetime in the case of coexpression of H2B-GFP and H2B-mCherry in the HeLa$^{H2B\text{-}2FP}$ cells compared to HeLa cells expressing pure H2B-GFP. Also, in NIH 3T3 cells transiently co-expresson of histon H2B fused to either GFP or RFP showed resonance transfer indicated by a reduced lifetime of GFP compared to pure H2B-GFP expression, proving that our FLIM setup is able to carry out FLIM-FRET measurements. Compared with the previous study (75) which revealed a FRET efficiency of 5 %, our finding showed FRET efficiencies of 4.4 % and 1.5 % for GFP-mCherry and GFP-RFP pairs, respectively. The difference between the obtained FRET efficiencies of HeLa$^{H2B\text{-}2FP}$ cell line and NIH $^{H2B\text{-}2FP}$ cells might be due to either a higher FRET efficiency of GFP/ mCherry over GFP/ RFP or the difference in the chromatin compaction between the species of human and mouse. An alternative explanation for this dissimilarity would be an altered expression or incorporation ratio, e. g. that the H2B-RFP is less well incorporated into nucleosomes (in heterochromatin) with respect to the H2B-mCherry pair thus leading to a lower FRET efficiency of NIH $^{H2B\text{-}2FP}$ cells compared to the HeLa$^{H2B\text{-}2FP}$ cell line.

Manipulating the chromatin density by VPA revealed a change of 1.5 % but only 0.1 % in the mean lifetime values of H2B-GFP in GFP/ mCherry and GFP/ RFP pairs, respectively. It is important to stress that the treatment with VPA, the lifetime of H2B-GFP in the presence of mCherry-H2B or RFP-H2B cannot exceed the lifetime of H2B-GFP alone (non-quenched) which restricted the dynamic range of readouts. On the other hand, an increase (4 fold PBS) in osmolarity revealed a significant change by 11 % and 8 % in the mean lifetime value of the H2B-GFP in GFP/ mCherry and GFP/ RFP pairs, respectively. Our study in the FRET pairs showed only a limited dynamic range for decompaction measurements and required either a transient transfection or stable cell lines. Further, a dependency on the expression ratio was observed which led to different amount of FRET resulting in large variability of lifetimes between individual cells, in turn, making high numbers of measurements necessary to obtain meaningfull results. From screening of organic fluorescent dyes and the characterization of their photophysical properties, Syto 16 (Figure 20), Nuclear Violet (Figure 22), Hoechst 33342 (Figure 22), Hoechst 34580 (Figure 22), and Syto 13 (Figure 23) turned out to be the most suitable ones for addressing the chromatin status. All of these were able to penetrate and label chromatin in living cells. Additionally, they showed a robust lifetime discrimination of condensed vs. non-condensed areas in NIH 3T3 cells nuclei. It has been observed that shorter lifetimes of the aforementioned DNA dyes are associated with compacted chromatin regions (chromocenters). Using cells after fixation, recent studies (66; 81), demonstrated that the distribution of the mean lifetime of DNA- labeling fluorophores like DAPI, Hoechst 33342 and PicoGreen depended on levels of the chromatin condensation which supported the application of single organic dyes as FLIM chromatin sensors.

Whereas a tendency to shorter liftime of DAPI has been observed in compacted chromatin regions of fixed NIH 3T3 cells (Figure 40 panel (b) and (d)) which is in agreement with the study of Estandarte et al (66). In living NIH 3T3 cells stained with DAPI the chromocenters were associated with longer lifetime regions (Figure 40 panel (a) and (b)) indicating a yet unknown lifetime modulating mechanism independent of just DNA compaction. In addition, the fixation procedure might have an impact on the mode of DAPI binding and thus FLIM readout. The quantitative analysis of the lifetime values of DAPI in living as well as fixed cells are listed in Table 22. In the current study, besides the differences in spatial distribution and the lifetime contrast, almost similar mean lifetime values of DAPI in both living and fixed cells have been found.

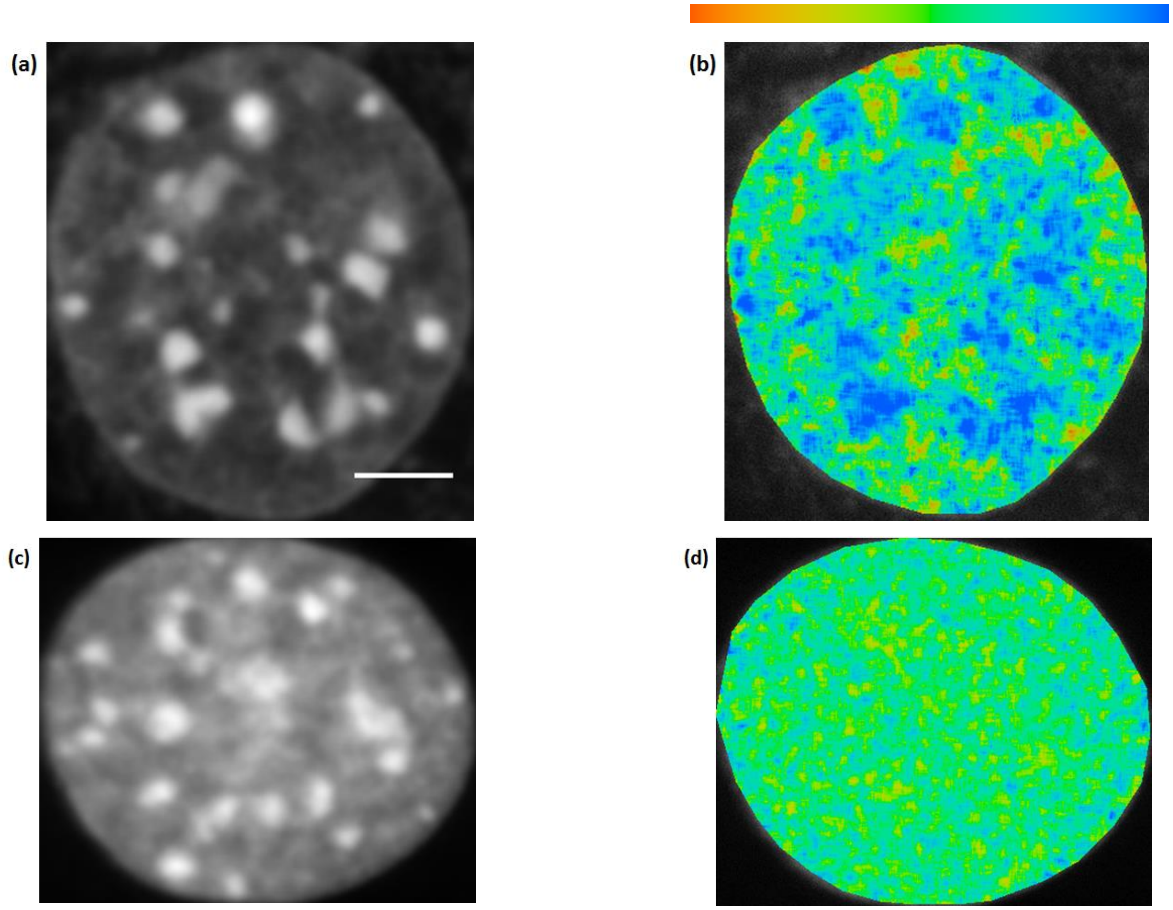

Figure 40. FLIM measurements of NIH 3T3 cells stained with DAPI. Living NIH 3T3 cell nucleus: The intensity and lifetime images are shown in panel (a) and (b). Fixed NIH 3T3 cell nucleus: The intensity and lifetime images are shown in panel (c) and (d).The lifetimes were repreasented in the continous pseudocolor scale ranging from 2200-3000 ps. Scale bar, 5μm.

	τ_m (ps) ± SD (Nucleus)	τ_m (ps) ± SD (Compacted regions)	τ_m (ps) ± SD (Decompacted regions)
Living cells	2670 ± 180	2907 ± 90	2633 ± 182
Fixed Cells	2660 ± 70	2637 ± 52	2662 ± 71

Table 22. Quantitative analysis of the lifetime of DAPI in different regions.

Several DNA dyes like Syto Blue 45 (Figure 21) did not show any direct correlation between fluorescence intensity and lifetime. However, they still might be used for studies which rely on the discrimination between DNA vs. RNA as areas containing mainly RNA (e. g. cytoplasm or nucleoli) showed a distinct lifetime compared to the DNA enriched part of the nucleus. Nuclear Violet turned out to be very (photo-) toxic so it might not be applicable in live cell studies, at least not for repetitive measurements as for a read out UV-laser light has to be applied. It still might prove usefull for fixed samples.

It has been reported that Hoechst 34580 and Hoechst 33342 are not cytotoxic DNA dyes (110). This is supported by the observation that under FLIM imaging conditions, in contrast to Nuclear Violet, no indication for a disturbed DNA damage response was observed (data not shown) The chemical structure of commertially available Hoechst 34580 and Hoechst 33342 are almost similar (110). However, Hoechst 34580 has the advantage that it can be better excited by the 405 nm laser with respect to the common Hoechst 33342 dye, which has an excitation maximum at 355 nm when complexed with DNA (86). In the present study, FLIM measurements of Hoechst 34580 showed a robust lifetime contrast between condensed and non-condensed areas whereas for the commonly used Hoechst 33342 only a smaller fraction of cells showed a pronounced contrast (Figure 41). As was stated, ICQ value has been used to quantify lifetime contrast between condensed and non condensed regions (ICQ; - 0.5< ICQ< 0.5).

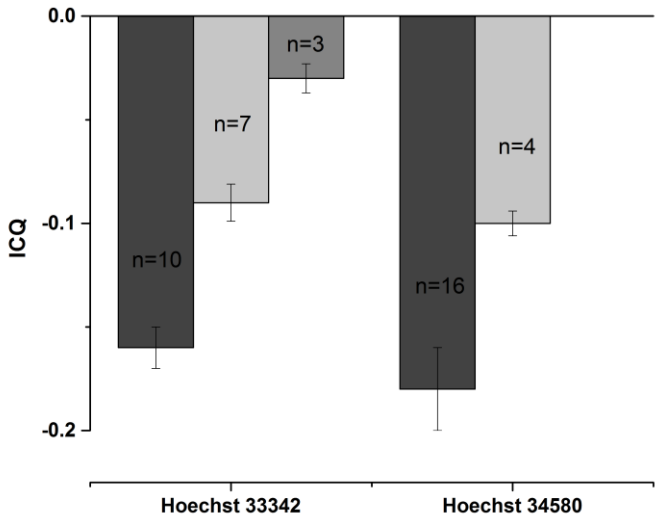

Figure 41. Quantification of the lifetime contrast of Hoechst 33342 and Hoechst 34580. The ICQ values were categorized in - 0.20 <ICQ< - 0.13, - 0.13 <ICQ< - 0.08 and - 0.08<ICQ<0. FLIM measurements of NIH 3T3 cells stained with Hoechst 34580 revealed a robust lifetime contrast between condensed and non condensed areas. The total number of evaluated cells, n=20. Error bars indicate mean ± SD.

Syto 13 showed a pronounced lifetime contrast at different compacted chromatin (ICQ: - 0.19) and is easily taken up in living cells. It is one of the promising chromatin compaction probes which can be excited using visible (488 nm) laser light, avoiding potential problems associated to UV irradiation. Syto 13 also showed DNA and RNA staining abilities, but with quite distinct fluorescence lifetime values of 2211 ± 68 ps and 2720 ± 84 ps, respectively. In agreement with this observation, distinct values of mean fluorescence lifetime of Syto 13 associated with DNA and RNA have been reported (111; 112).

Despite the observed lifetime contrast in NIH 3T3 cells, the exposure of some of the tested organic DNA dyes with chemical treatments did not revealed a significant change in fluorescence lifetime despite a induced change of chromatin structure.In turn, it can be assumed that they are not as sensitive on chromatin compaction itself compared to those showing remarkable changes upon treatment. Their lifetimes might be influenced by other – hitherto unknown- environmental factors associated with the chromocenters. Our observation showed that VPA treatment of NIH 3T3 cells stained with Syto 13 and Hoechst 34580 revealed the change of 2 % and 3 % in the mean lifetime values of them, respectively. As VPA induced hyperacetylation was shown to induce chromatin decondensation by scanning microspectrophotometry (81), it can be concluded that the observed lifetime changes reflected a global chromatin relaxation. Furthermore, deacetylase inhibition by TSA treatment of the NIH 3T3 cells stained with Syto 13 also demonstrated a change of 2 % in the mean lifetime value of the Syto 13 indicating a similar global chromatin relaxation induced by acetylation. A significant change about 15 % in the mean lifetime of Hoechst 34580 was observed following 0.5 PBS treatment. The fast as well as reversible modulation of Hoechst 34580 lifetime can be linked to chromatin decompaction induced by hypoosmolarity as described in Moscariello et al (113). Hence, we could demonstrate

that bisecting the osmolarity acts very fast and has a much larger effect on chromatin decompaction than histone acetylation. Hyperosmolarity (4 fold PBS treatment) of NIH 3T3 cells showed around 3 % and 7 % decrease in the mean lifetime value of Syto 13 and Hoechst 34580, respectively. Hence, it can be concluded that the detected decrease in the mean lifetime values represented a global chromatin compaction. The observed significant change in the mean lifetime of Hoechst 34580 supported a massive chromatin compaction which was also evident in the intensity image indicated by the generation of filamentous structures. In line with this observation, hyperosmolarity has been shown to induce chromatin condensation in live cell microscopy of stable HeLa H2B-GFP cells (98). They visualized a relative 60 % reduction of the volume of chromatin after application of 4 fold PBS (98) supporting the FLIM data of this thesis.

An important advantage which became obvious using the promising single organic dyes in murine cells was the ability to detect different compaction levels of different chromatin structures, i. e. heterochromatin and euchromatin. In contrast to especially minor grooves binding dyes, e. g. Hoechst family, fluorescence protein FRET pairs did not revealed chromocentersor showed them only very weakly even in the intensity images. This might be due to problems in incorporation of tagged histones in dense heterochromatin, but on the other hand, dyes like Hoechst with a high AT over GC preference in DNA over emphasize the heterochromatic DNA content and different binding (densities) might also influence the corresponding lifetime. Regarding a decompaction response, larger effects can be expected in these denely packed areas. In agreement with these considerations, the chromocenters revealed changes of 4.8 % compared to a global 3.1 % following VPA treatment whereas the massive influence of 0.5 PBS on lifetime was similar for both chromocenters and whole nucleus (14.9 % vs. 15.7 %). It might be conluded that the mode of applying chromatin changes (via acetylation or dilution of bivalent cations) influences the binding and lifetime of Hoechst 34580 differently in different nuclear compartments. Whereas for the H2B-FRET pairs the quenching mechnism acts via Förster resonance energy transfer, the molecular mechanism behind the lifetime dependency on chromatin compaction of the single dyes is not clear, but might be based on molecular crowding (114) leading to non-radiative quenching. However other environmental changes affecting the stability of the excited states cannot be excluded and might act differently on different dyes. Taken together, Hoechst34580 provided a dynamic range of > 20 % for compaction/decompaction measurements in the FLIM assay, which is supperior to the restricted range of the H2B FRET pairs, especially for measuring chromatin decompaction.

5.2. Physical Characterization

The robustness of the lifetime value has been tested with the use of fluorescein (See Table 1). The measured fluorescence lifetime of fluorescein was in strict agreement with measured lifetime values around 4 ns reported in previous studies (115; 116; 117) demonstrating the temporal calibration of the system.

A dependency of lifetime values of FRET pairs on expression ratio was observed which leads an large variability of the lifetime value in different cells, an issue which was not addressed in the original publication (75) and which makes either a sufficiently high number of measurements or a tight control of expression levels of measured cells necessary to obtain significant results when small changes can be expected. In contrast, Syto

13 as an organic dye yielded a robust and reproducible lifetime value showing only low variation between independent experiments (Figure 42). It is worth to highlight that, a heated environmental chamber along with adjustable CO_2/O_2 condition for cells incubation has been used. Some other parameters such as photon numbers, concentration, accurate pipeting and dye incubation have been considered. As seen in Figure 42, an approximate consistant lifetime value was obtained (2804 ± 20 (n= 9), 2806 ± 25 (n=9), 2810 ± 42 (n=11) and 2812 ± 25 (n=12) ps).

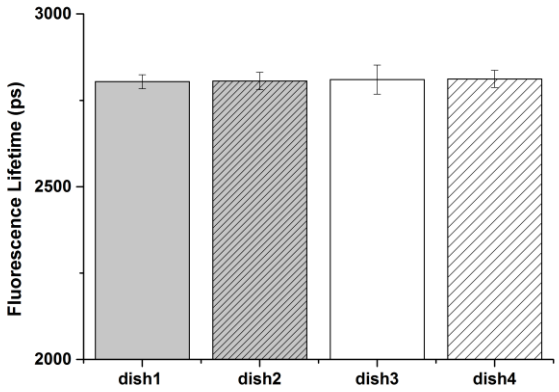

Figure 42. Robustness of the fluorescence lifetime value of Syto 13. Error bars indicate mean ± SD.

The lifetime value of Syto 13 was reported to be 3800± 300 ps (118). Although the robustness of lifetime value of Syto 13 has been observed, this value is not in agreement with the previous study. The DNA packing might differ in different cell lines, in turn; may give rise to reveal different lifetime, however in the light of the observed compaction related lifetime chages observed so far, a chang of 1 ns seems out of range. Most probable this difference arises from major differences in the employed setup based on a gated intensified CCD camera to measure lifetime in the cited study of Li et al (118).

The study of the photostability showed that by reduction of the laser power from 9.00 µW to 2.60 µW still yielded sufficient photons (count rate 10^5-10^6/s) within 20 s and the lifetime distribution width of individual nuclei was not signicantly affected and still allows the discrimination of condensed and non-condensed areas. One of the distinctive characteristics of fluorescence lifetime imaging is its independency on the non-quenched fluorescence intensity. Surprisingly, a fluorescence lifetime correlation to the recorded photon numbers became apparent in our FLIM measurements upon changing laser intensity, e. g. a global increase of the lifetime values was observed for both 2.60 µW and 9.00 µW laser power setting compared to higher laser power. At high counting rates exceeding 10 % of the laser pulse rate of 80 MHz the preferential detection of the first photon gives rise to a loss of a potential second photon in the same signal period leading to a so-called pile-up effect. This yields a deformation of the excitation decay curve and in turn, results in an underestimation of the calculated lifetime (24). The pile-up distorted τ_{meani} (intensity-weighted lifetime of the measured decay profile) can be calculated by (24)

$$\tau_{meani} \approx \tau\,(1\text{-}P/4),$$

where P is the average number of photons per laser period, τ represents fluorescence lifetime.

In addition, photon numbers are affected by counting loss, i. e. loss of recorded photons is likely to occur due to the dead time of the FLIM detection (in the order of 100 ns) even at relatively low count rates in the order of 1 MHz (24). In case of inhomogeneous samples, local count rates might exceed average values by far, leading to a reduction in intensity contrast. So, these non detected photons have to be considered in the pile-up correction for calculating the probability of having more than one initial incoming photons per laser pulse.

An exapmle of the aforementioned effects were shown in Figure 43. Table 23 listed the measured photons number and lifetime of the nucleus as well as bright areas (chromocentes) of NIH 3T3 cells stained with Hoechst 34580. As the high local count rates (5.2 MHz) due to bright areas in the detection field was observed, a pixel-wise mathematical correction of counting loss and pile-up has been applied (using the counting loss corrected incident photon rates up to 20 MHz). Figure 43 panel (a) shows the uncorrected intensity image. The impact of the counting loss correction is demonstrated in panel (b) showing a massive improvement in contrast. Panel (c) depicts the uncorrected lifetime image recorded at an average uncorrected count rate of 2 MHz. An average lifetime correction of around 1 % was calculated as well as correction values of 2 % for bright areas were determined. The corresponding lifetime image with pile-up correction is shown in panel (d). As seen in panel (d), adopting the colour LUT the compaction dependent lifetime was still clearly visible. Hence, this investigation proved that although pile-up slightly affected the calculated (absolute) lifetime, the observed chromatin compaction dependent lifetime was not introduced by this effect.

	Uncorrected image	Corrected image
Photons (nucleus)	192 ± 38	307 ± 110
Photons (chromocenters)	292 ± 22	634 ± 108
τ_i (ps) (nucleus)	1198 ± 41	1219 ± 37
τ_i (ps) (chromocenters)	1108 ± 33	1150 ± 29

Table 23. The summary of measured photons number and intensity-weighted lifetime values of Hoechst 34580 in the nucleus and bright areas shown in Figure 43.

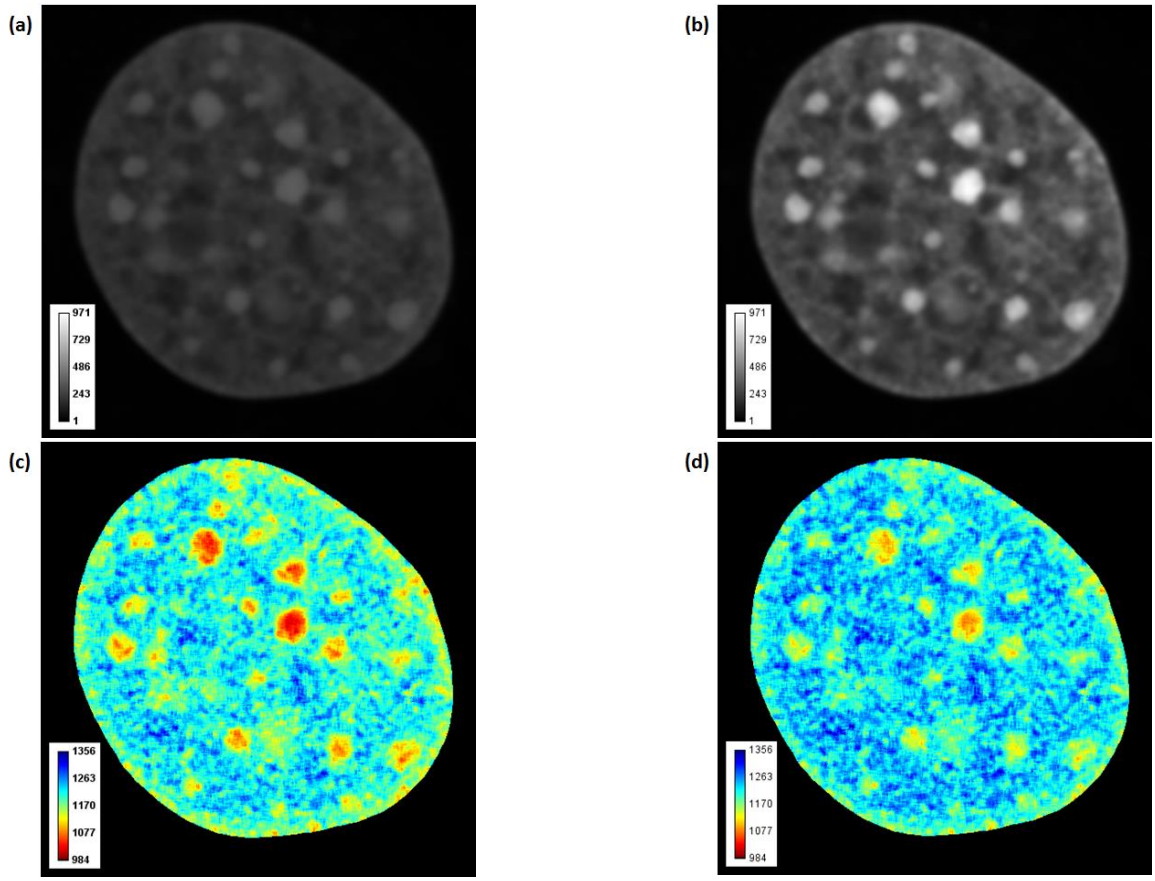

Figure 43. Confocal FLIM images of NIH 3T3 cell nucleus stained with Hoechst 34580 at average count rate of 2 MHz. (a) uncorrected intensity image and (b) intensity image with counting loss correction. Uncorrected lifetime image and lifetime image with pile-up correction are shown in (c) and (d), respectively.

5.3. Application of the newly established chromatin compaction assay in radiation biology

In order to monitor radiation-induced chromatin relaxation in living cells, conditions for multiple repositioning between the FLIM setup and irradiation at the GSI microprobe as well as SIS accelarator were established. This procedure allows obtaining FLIM images in good qualities, but unexpectedly; no evidence of a significant radiation-induced chromatin decondensation could be observed in the evaluated images. The absence of unambiguously hit chromocenters in retrospective analysis after fixation points to issues of hitting accuracy in these experiments (microprobe), which became evident also in other unrelated experiments (data not shown). For the experimets at the SIS, assuming the requested fluence of 10^7 cm^{-2} a larger nucleus of 348 μm^2 (as in Figure 29) should have received an average of 35 particle traversals. The geometrical cross section of the chromocenters derived from the intensity image was measured to be 19 μm^2 thus around two particles could be expected to traverse chromocenters in that nucleus. However, this would also include chromocenters which are hit at the border. Considering the hits to be more centrally in chromocenters (considering 120 nm rim where a detection would not be possible) the number of traversals would be reduced by a factor of three yielding expectation values below one.

In addition, it has been reported that radiation-induced DSBs relocated to the periphery of the heterochromatin regions within less than 20 minutes (9). However, the offline irradiation procedure took around 30- 40 minutes. So, it is highly likely that the DSBs and potentially associated decompacted chromatin would have been transfered to the periphery of the chromocenters in the mentioned time interval. There, it would be indistinguishable to the similarly loose euchromatin. The lack of a proper damage signal made it difficult to assign damage site. This might be related to a failure of immunocytochemical staining on the used polyproylene film. However, stainings of good quality have been reported on that material (9). An alternative explanation could be that, during the offline irradiation cells were subjected to stress due to the limited amount of cell medium in the closed chambers, which might hinder a proper DNA damage response including the recruitment of repair proteins. A slight shrinkage of the nucleus shown in Figure 28 might indicate osmotic stress. This interpretation was supported by the observation of globally reduced lifetime values of Syto 13. To avoid these problems, the irradiation procedure including the sample transport might have to be speeded up and the chamber closed just before the irradiation.

To cirmumvent the problems mentioned above and to get access to fast radiation induced chromatin changes the FLIM system was connected to the beamline microscope for real-time measurements. The applied fluence of 5.10^6 cm^{-2} of broad beam carbon ions at the UNILAC accelerator expected to give rise to around 10 traversals per nucleus assuming a nuclear cross section of 200 μm^2. In that beamline experiment the DNA dye showing the most pronounced chromatin compaction dependent lifetime distribution, Nuclear Violet was used. Recording of FLIM images before and after irradiation with carbon ions revealed high quality images. However, no indication of the local recruitment of the damage marker protein could be observed (Figure 30). Unexpectedly, a pan-nuclear damage pattern was observed indicating a high phototoxicity of Nuclear Violet (Ex_{max}: 405 nm). Hence, a possible explanation is the UV-light (405 nm laser) during FLIM recording in combination with the photosensitizing Nuclear Violet already was sufficient to induce massive DNA damage which might have inhibited the observation of a local radiation-induced chromatin decompaction and damage marker accumulation. This phototoxicity could be demonstrated in unirradiated samples, where short UV irradiation in combination with Nuclear violet was sufficient to trigger a pan-nuclear γH2AX response (data not shown). However, this phototoxicity was not evident for other organic dyes like Syto 13 and Hoechst 34580. The high phototoxicity disqualifies Nuclear Violet for further live cell studies. However Nuclear Violet showed a pronounced lifetime contrast between condensed and non- condensed regions not only in living cells but similarly in fixed cells as well (compare Figure 30 and 44). Therefore, it was also used to probe radiation induced chromatin decompaction after fixation of targeted irradiated chromocenters of living NIH 3T3 cells at the microprobe (gold ions, 4.5 MeV/u). Similar to Hoechst 34580 (Figure 31), a fast local decondensation of the HC at the sites of targeted chromocenter stained with Nuclear Violet could be detected by an intensity depletion of Nuclear violet at the site of a heterochromatic ion hit in combination with a pronounced local raise in the lifetime (Figure 44). The site of ion hit within the chromocenter was determined by the aggregation of the damage marker ϒH2AX with the dip in the ϒH2AX signal indicating the track center. All together, Nuclear Violet still might be usefull in addressing the chromatin status in fixed cells.

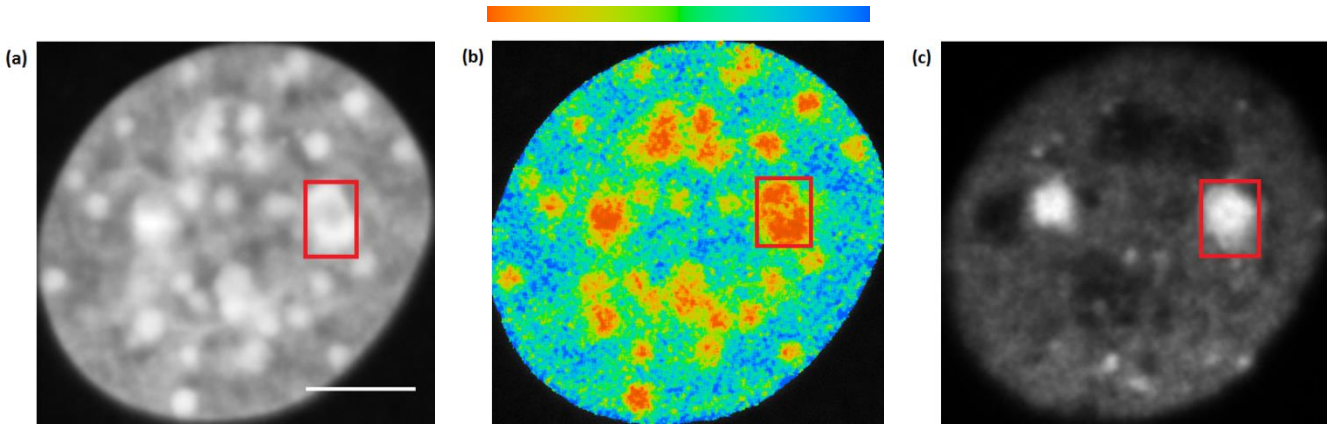

Figure 44. Decompaction of heterochromatic DNA in NIH 3T3 chromocenters targeted with single ions at the microbrobe. Intensity and lifetime images of ion hit chromocenters of fixed NIH 3T3 cells stained with Nuclear Violet are depicted in pannel (a, b), respectively. Intensity images of ion hit site marked by ϒH2AX and immunostained with Alexa 514 are shown in panel (c). The heterochromatic ion hit chromocenter enclosed in the solid red rectangular. Scale bar, 5μm.

Using cells fixed after irradiation, it was demonstrated that a single DNA dye can be successfully used to display the radiation-induced chromatin decondensation (Figure 31 and Figure 44). The occurrence of chromatin relaxation could be detected by a remarkable increase in the lifetime of Hoechst 34580 at the sites of uranium ion traversals as well as the rise in the lifetime value of Nuclear Violet in the targeted chromocenters by gold ions. The increase was locally confined to a small area around the traversing site or in targeted chromocenter go along with an intensity depletion of the DNA dyes, Hoechst 34580 and Nuclear Violet, similar to that described previously for DAPI or Hoechst 33342 (9; 18). The pronounced peak in fluorescence lifetime spatially correlating with the depletion in heterochromatic fluorescence intensity also supported the hypothesis that the observed dip in the intensity was not just a reduced binding efficiency of the dye at damage sites since the lifetime was not changing with dye concentration, but reflects the radiation induced chromatin decompaction which is most probably necessary for further damage processing and subsequent repair (119). Whereas a depletion of the dye could alternatively be explained by a destruction of the dye or a loss of binding sites for the dyes, the lifetime increase gives the evidence for the chromatin decompaction. A local chromatin decondensation has been observed 15 minutes after exposure to ϒ- rays using intensity information showing decreased DNA labelling and increased H4K9 acetylation at sites of ϒ-H2AX (108). Similarly, upon exposure to ϒ- rays a decondensation in heterochromatin regions has been shown (109). Recently, the chromatin rearrengement during DNA repair after low LET radiation exposure were quantitatively studied. In respect to a change in clustering of single molecule positions, a remarkable difference between control cells and irradiated ones had been observed in that study. Their finding was interpreted as an evidence of the radiation-induced relaxation in heterochromatin areas leading to the chromatin structure changes (120).

The main aim of the present study was to inspect radiation-induced chromatin changes in living cells. As pointed out, the successfully demonstration of radiation-induced chromatin decondensation after post-irradiative fixation using FLIM encouraged to repeat the online broad beam irradiation using one of the non-phototoxic DNA dyes. However, due the the lack of beamtime at GSI these experiments could not be performed.

As an alternative approach to irradiate living cells, the FLIM setup was coupled to a 35 kV X-rays tube and NIH 3T3 cells stained with Hoechst 34580 irradiated by 10 Gy X-rays. Interestingly, the exposure of these murine cells to 10 Gy X-rays revealed a global change by around 2 % in the lifetime values of Hoechst 34580 in post-irradiation FLIM measurements. Successive FLIM measurements without irradiation did not introduce a significant difference in the lifetime values of Hoechst 34580. Based upon previous findings (52), the detected raise in the lifetime value of the Hoechst arised most probably from a global chromatin decompaction induced by this relatively large dose, which gives rise to around 350 DSBs (121) and many more SSBs and other DNA lesions. At 2 Gy the decompaction dependent increase in the lifetime value was no longer significant. However in contrast to the obeservations by Falk et al (108) for Topro3 staining in combination with ^{60}Co ϒ- rays no local dye depletion was evident after X-rays in Hoechst 34580 stained samples.

5.4. Potential biological application of the newly established chromatin compaction assay

It could be demonstrated, that our newly established chromatin compaction assay based on FLIM measurements can also be applied to inspect chromatin compaction in proliferation studies. Our findings revealed a change by around 3.3 % in the mean lifetime of Hoechst 34580 in non- cycling G_0 cells versus cycling human fibroblasts (AG1522D) cells in the G_1 phase of the cell cycle. Hence, the results (Figure 37-38) supported the hypothesis of a more condensed state of chromatin in G_0 which was proposed in the literature (92; 93). Additionally, FLIM measurements of the U2OS-G_1/S-GFP cells stained with Hoechst 34580 also showed that a change by around 2.7 % in the mean lifetime values of Hoechst 34580 in the G_1 phase compared to the G_2 phase of the cell cycle which was indicated by a cytoplasmatic staining of the genetically expressed cell cycle marker. An interpertation of the observed increase in the mean lifetime of Hoechst 34580 in G_2 cells might be the compaction in early G_1 phase during transition from M-Phase or a decompaction of heterochromatin for replication in late S-phase.

6. Concluding remarks

The work performed during this thesis has been devoted to both the establishment and characterization of a chromatin compaction assay employing fluorescence lifetime imaging microscopy as well as its application in mainly radiation biology. In the first part, the sensitivity of our setup using a FLIM-FRET approach based on coexpression of labelled histones was inspected. A comparison between our findings with previous investigation validated the sensitivity of the FLIM setup at GSI. However, the dependency of the fluorescent protein- tagged hitones on the cellular system as well as the small dynamic range of chromatin decompaction reponse of them encouraged to use cell permeable DNA labling organic dyes as an alternative approach. Thus, to find out sensitive and promising chromatin compaction probes a variety of single organic dyes covering the UV and visible regions of the spectrum were screened. The obtained data revealed some of these dyes showing a decreased lifetime at compacted chromatin similar to or even exceeding that of the FLIM-FRET sensors. Thus, further characterization of their behavior and response were done indicating Syto 13 and Hoechst 34580 as promising chromatin compaction probes because of their higher dynamic range response to osmotic as well as enzymatic induced chromatin changes.

The second part of the work focused on monitoring radiation-induced chromatin decompaction in living cells. Various approaches to detect chromatin relaxation after irradiation were used. By off-line irradiation conditions for multiple repositioning between the FLIM setup and the GSI irradiation facilities were established. However, unexpectedly; no evidence of ion-induced chromatin decondensation could be detected in living cells in the limited amount of experiments that could be performed. The absence of traversed chromocenters in the measured nuclei evident after inspection of postirradiative fixation and staining for DSB marker points to either issues of hitting accuracy or insufficinet fluences to obtain a detectable number of traversed chromocenters. Furthermore, due to the time needed to perform the off-line procedure, it can be speculated that DSBs might be transferred to the periphery of the chromocenters. However presently it can not be ruled out, that the fixation procedure intensifies the radiation induced chromatin opening.

In addition at least one of the promissing organic dyes Nuclear Violet turned out to be very phototoxic in combination with the UV excitation light necessary for the FLIM readout, rendering it useless for measuring changes in living cells. Using Hoechst 34580 but also Nuclear Violett, a local chromatin decondensation at sites of heterochromatic ion traversals indicated by a notable enhancement in the lifetime value could be demonstrated in nuclei fixed after irradiation. This main result provides evidence that the previously observed dip in the intensity of DNA stains at sites of ion traversals was not just due to a reduced binding efficiency of the dye at damage sites. Using X-rays, a global chromatin decompaction could be demonstrated in living cells proving the applicability of this approach as a live cell assay. While a lot remains to be explored, taken together the findings provide the proof of a chromatin relaxation induced by ionizing radiation.

In the last part it was shown that the chromatin compaction assay can also be successfully applied in other fields of biology, e. g. by addressing different chromatin compaction in different cell cycle phases or in resting versus cycling cells. It might in future also be used to monitor chromatin changes associated with cellular differentiation and senescence or the development of cancer. Also, the uptake and influence of certain drugs

influencing the chromatin status and applied as chemotherapeutics in cancer therapy like histone deacetylase inhibitors (80; 122) can be studied using the FLIM based chromatin compaction assay in future.

7. Appendix

The available emission filters of the FLIM setup are listed in Table (A.1). The emission spectra of them were measured and shown in Figure (A.1) to (A.14).

Emission Filter	Provider	Emission Filter	Provider
450/70 BP	AHF	460 LP	AHF
534/42 BP	Semrock	519 LP	Semrock
700 BP	AHF	520 LP	AHF
528 BP	Semrock	590 LP	AHF
545/30 BP	Semrock	514 NOTCH	Semrock
607/70 BP	Semrock	473 NOTCH	AHF
409 LP	2000	480/40 HQ	2000

Table A.1. List of available emission filters for our FLIM setup. The spectra of the filter were measured and shown in Figure (A.1) to (A.14). BP represents band pass filter and LP refers to long pass.

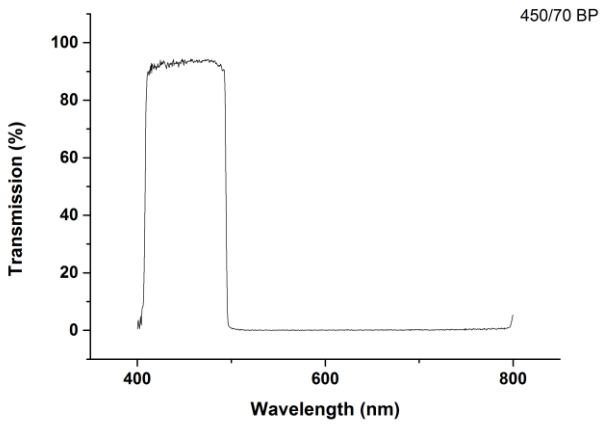

A. 1. The emission spectra of 450/70 BP.

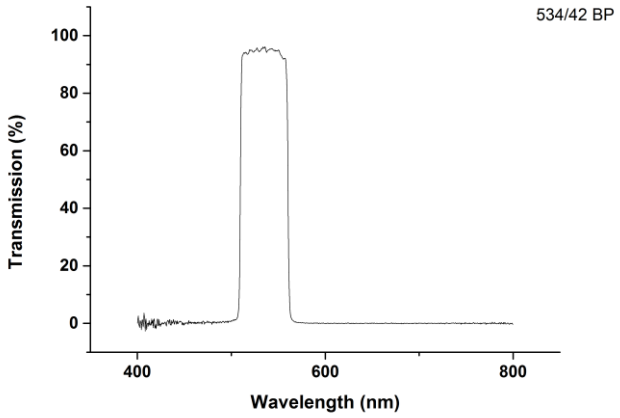

A. 2. The emission spectra of 534/42 BP.

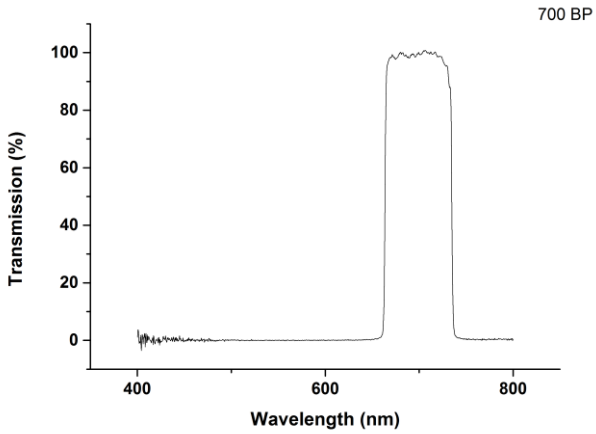

A. 3. The emission spectra of 700 BP.

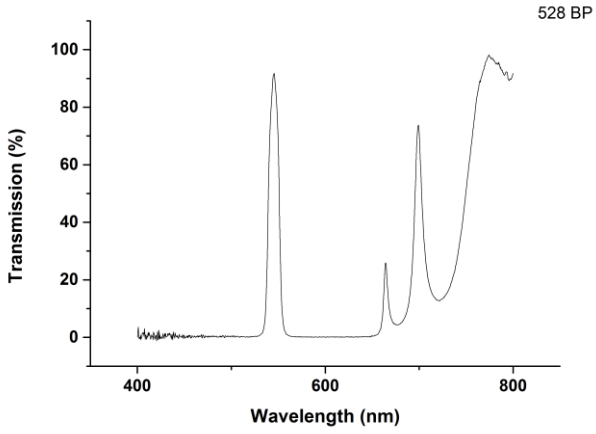

A. 4. The emission spectra of 528 BP.

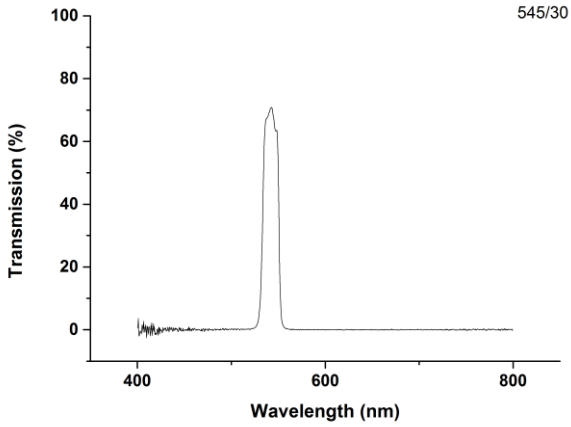

A. 5. The emission spectra of 545/30 BP.

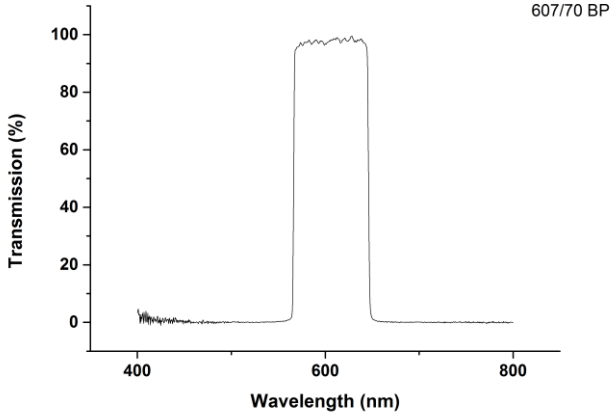

A. 6. The emission spectra of 607/70 BP.

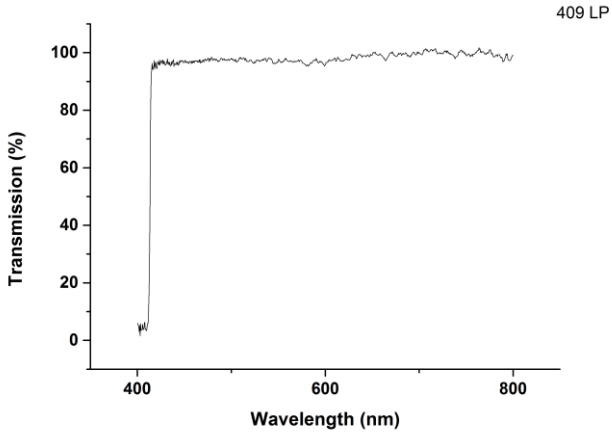

A. 7. The emission spectra of 409 LP.

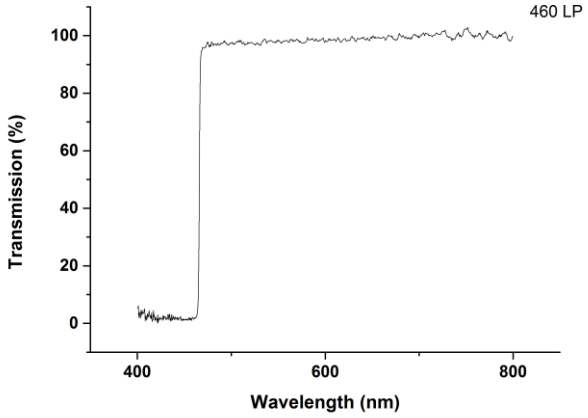

A. 8. The emission spectra of 460 LP.

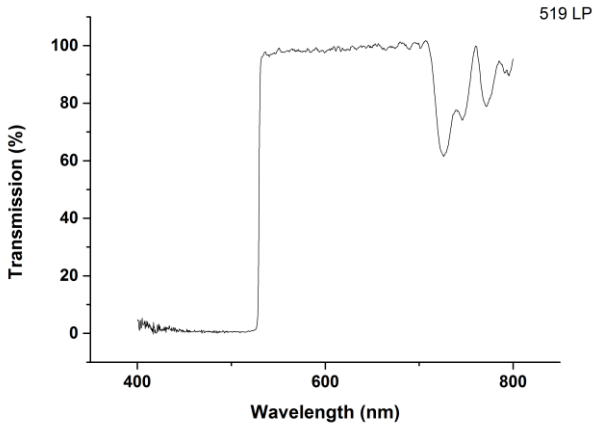

A. 9. The emission spectra of 519 LP.

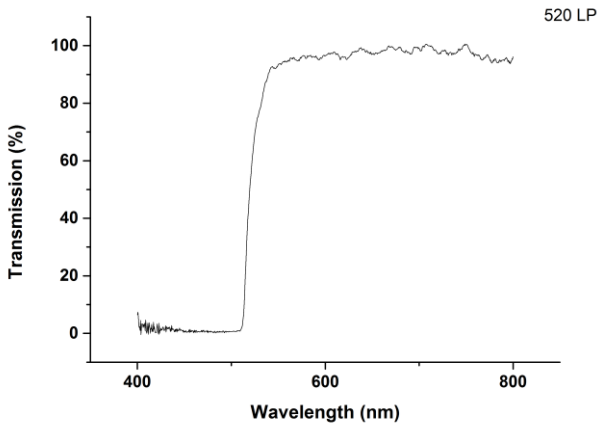

A. 10. The emission spectra of 520 LP.

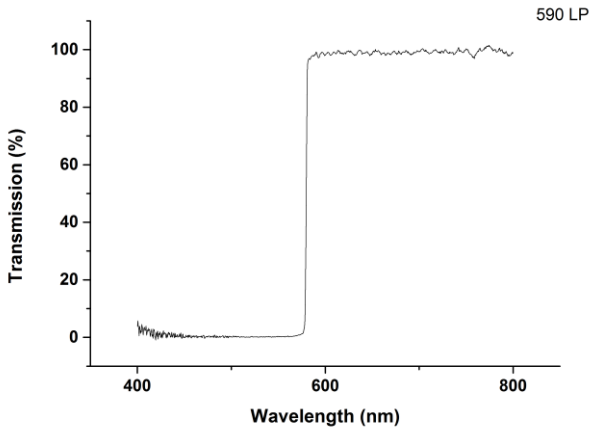

A. 11. The emission spectra of 590 LP.

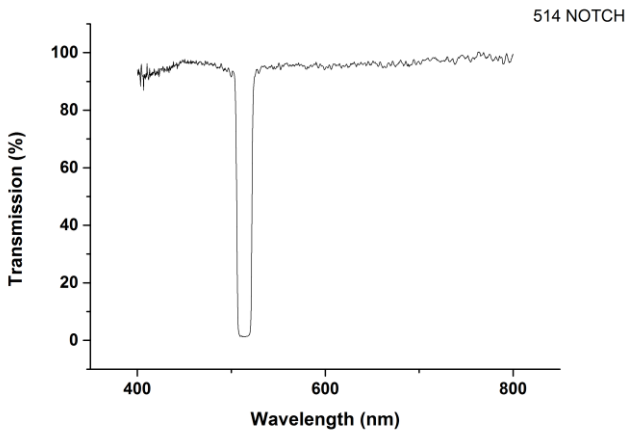

A. 12. The emission spectra of 514 NOTCH.

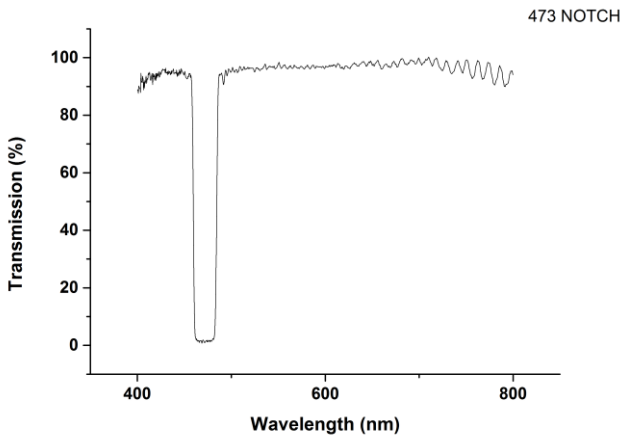

A. 13. The emission spectra of 473 NOTCH.

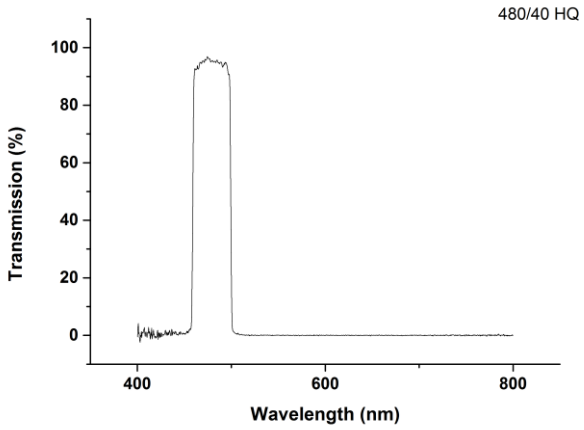

A. 14. The emission spectra of 480/40 BP.

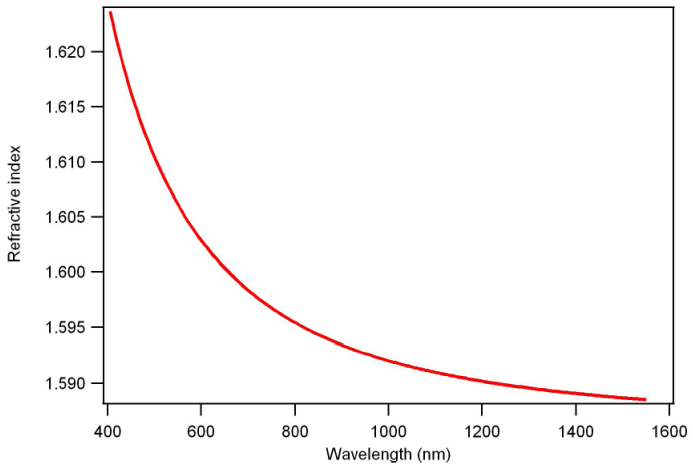

A. 15. Dispersion of the refractive index of the Argolight's glass (Figure is reproduced from (123)).

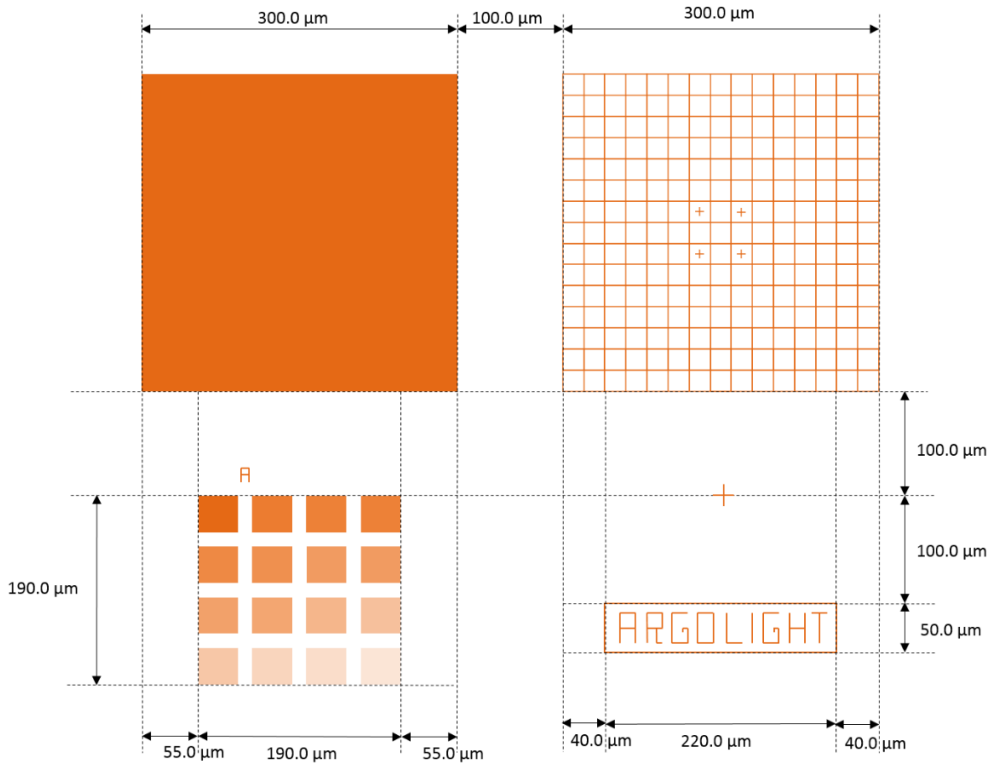

A. 16. The examples of the Argolight's fluorescent patterns (Figure is reproduced from (123)).

	1	2	3	4	5
Row A	15 µm	6 µm	4 µm	1 µm	0.5 µm
	Green/orange/ far red thin rings	Blue throughout/ green ring	Blue/green/red/ far red	Blue/ green/red/ far red	Blue/green/red/ far red
Row B (intensity series)	6 µm	6 µm	6 µm	6 µm	6 µm
	Green	Green	Green	Green	Green
	100 % intensity	33 % intensity	10 % intensity	3 % intensity	0. 7 % intensity

A. 17. Listed configuration of FocalCheck fluorescence microscope test slide #1 (124).

List of figures

Abbreviations

FLIM	Fluorescence Lifetime Imaging Microscopy
FRET	Förster Resonance Energy Transfer
TCSPC	Time Correlated Single Photon Counting
LET	Linear Energy Transfer
IRF	Instrument Response Function
DNA	Deoxyribonucleic acid
RNA	Ribonucleic Acid
DSB	Double Strand Break
HC	Heterochromatin
EU	Euchromatin
FRAP	Fluorescence Recovery After Photobleaching
CW	Countinous Wave
IC	Internal Conversion
ISC	Inter System Crossing
VR	Vibrational Relaxation
bh	Becker & Hickl
LP	Long Pass
BP	Band Pass
ICQ	Intensity Correlation Quotient
FD	Frequency Domain
ROI	Region Of Interest
eGFP	Enhanced Green Fluorescence Protein
GFP	Green Fluorescence Protein
RFP	Red Fluorescence Protein
DAPI	4', 6-Diamidin-2-phenylindol
VPA	Valproic Acid
TSA	Trichostatin
HDACi	Histone Deacetylase Inhibitor

Bibliography

1. Chromatin domains and the interchromatin compartment form structurally defined and functionally interacting nuclear networks. H. Albiez, M. Cremer, C. Tiberi, L. Vecchio, L.r Schermelleh, S. Dittrich, K. Küpper, B.Joffe, T. Thormeyer, J. v Hase, S. Yang, K. Rohr, H. Leonhardt, I. Solovei, C. Cremer, S. Fakan, T. Cremer. s.l. : Chromosome Research, 2006, Bd. 14, S. 707–733.
2. Dynamic genome architecture in the nuclear space: regulation of gene expression in three dimensions. C. Lanctôt, T. Cheutin, M. Cremer, G. Cavalli, T Cremer. 2007, Nature, Bd. 8, S. 104-115.
3. Geomorphometric assessment of spatial sediment connectivity in small Alpine catchments. M. Cavallia, S. Trevisanib, F. Comitic, L. Marchi. 2013, Geomorphology, Bd. 188, S. 31–41.
4. A permissive chromatin structure is adopted prior to site-specific DNA demethylation of developmentally expressed genes involved in macronuclear differentiation. A. Bulic, J. Postberg, A. Fischer, F. Jönsson, G. Reuter, H J Lipps. 2013, Epigenetics & Chromatin, Bd. 6:5.
5. The paradox of functional heterochromatin. P. Dimitri, N. Corradini, F. Rossi, F Verni. 2005, BioEssays, Bd. 27, S. 29–41.
6. Constitutive heterochromatin: a surprising variety of expressed sequences. P. Dimitri, R. Caizzi, E Giordano, M C Accardo, G. Lattanzi, G. Biamonti. 2009, Chromosoma, Bd. 118, S. 419–435.
7. Genomic instability in mice lacking histone H2AX. A. Celeste, S. Petersen, PJ. Romanienko, O. Fernandez-Capetillo, HT Chen, OA. Sedelnikova, B. Reina-San-Martin, V. Coppola, E. Meffre, MJ. Difilippantonio. 2002, Science, Bd. 296, S. 922–927.
8. Increased ionizing radiation sensitivity and genomic instability in the absence of histone H2AX. C H. Bassing, K F. Chua, J. Sekiguchi, H. Suh, S R. Whitlow, J C. Fleming, B C. Monroe, D N. Ciccone, C. Yan, K. Vlasakova. 2002, Proceedings of the National Academy of Sciences, Bd. 99, S. 8173–8178.
9. DNA double-strand breaks in heterochromatin elicit fast repair protein recruitment, histone H2AX phosphorylation and relocation to euchromatin. B. Jakob, J. Splinter, S. Conrad, K. Voss, D. Zink, M. Durante, M. Löbrich, G. Taucher-Scholz. 2011, Nucleic Acids Research, S. 1–11.
10. Function of chromatin structure and dynamics in DNA damage, repair and misrepair: g-rays and protons in action. L. Ježková, M Falk, I. Falková, M. Davıdková, A. Bacıková, L. Stefancıková, J. Vachelová, A. Michaelidesová, E. Lukásova, A. Boreyko, E. Krasavin, S. Kozubek. 2013, Applied Radiation and Isotopes, Bd. 83, S. 128-136.
11. Chromatin structure and radiation-induced DNA damage: From structural biology to radiobiology. C. Lavelle, N. Foray. 2014, The International Journal of Biochemistry & Cell Biology, Bd. 49, S. 84–97.
12. Histone Modifications and DNA Double-Strand Break Repair after Exposure to Ionizing Radiations. C R. Hunt, D. Ramnarain, N. Horikoshi, P. Iyengar, R K. Pandita, J W. Shay, T K. Pandita. 2013, Radiation Research, Bd. 179, S. 383–392.
13. Nuclear dynamics of radiation-induced foci in euchromatin and heterochromatin. I. Chiolo, T. Tang, W. Georgescu, SV. Costes. 2013, Mutation Research, Bd. 750, S. 56-66.
14. Microscopic visualization of a biological response to charged particle traversal. G. Taucher-Scholz, B. Jakob, B. Becker, M. Scholz. 2003, Nuclear Instruments and Methods in Physics Research B, Bd. 209, S. 270–276.

15. Interaction of heavy ions with nuclear chromatin: Spatiotemporal investigations of biological responses in a cellular environment. B. Jakob, G. Taucher-Scholz. 2006, Nuclear Instruments and Methods in Physics Research B, Bd. 245, S. 292–297.
16. Chromatin dynamics during DSB repair. M. Falk, E. Lukasova, B. Gabrielova, V. Ondrej, S. Kozubek. 2007, Biochimica et Biophysica Acta, Bd. 1773, S. 1534–1545.
17. DDB2 promotes chromatin decondensation at UV-induced DNA damage. MS. Luijsterburg, M. Lindh, K. Acs, MG. Vrouwe, A. Pines, H v Attikum, L. Mullenders, NP. Dantuma. 2012, The Journal of Cell Biology, Bd. 197, S. 267–281.
18. Species conserved DNA damage response at the inactive human X chromosome. I. Müller, B. Merk, KO. Voss, N. Averbeck, B. Jakob, M. Durante, G. Taucher-Scholz. 2013, Mutation Research, Bd. 756, S. 30-36.
19. Double-Strand Breaks in Heterochromatin Move Outside of a Dynamic HP1a Domain to Complete Recombinational Repair. I. Chiolo, A. Minoda, SU. Colmenares, A. Polyzos, SV. Costes, GH. Karpen. 2011, Cell, Bd. 144, S. 732–744.
20. Spatio-Temporal Dynamics of Chromatin Containing DNA Breaks. MJ. Kruhlak, A. Celeste, A. Nussenzweig. 2006, Cell Cycle, Bd. 5:17, S. 1910-1912.
21. Localization of Antigen in Tissue Cells: II. Improvements in a Method for the Detection of Antigen by Means of Fluorescent Antibody. Coons, A. H. 1949, Journal of Experimental Medicine, Bd. 91, S. 1-13.
22. Photophysical processes in single molecule organic fluorescent probes. E M S. Stennett, M A. Ciuba, M. Levitus. 2014, The Royal Society of Chemistry, Bd. 43, S. 1057--1075.
23. The physics and biology of fluorescence microscopy fluorescence microscopy. Wouters., FS. 2006, Contemporary Physics, Bd. 47, S. 239 – 255.
24. Becker., W. The bh TCSPC handbook. Berlin : Becker & Hickle GmbH, 2014.
25. Optical Imaging of Calcium Transients in Neurons and Pharyngeal Muscle of C. elegans. R. Kerr, V. Lev-Ram, G. Baird, P. Vincent, RY. Tsien, and W R. Schafer. 583-594 : s.n., 2000, Neuron, Bd. 26, S. 583-594.
26. Monomeric fluorescent timers that change color from blue to red report on cellular trafficking. F V. Subach, O M. Subach, IS. Gundorov, K S. Morozova, K D. Piatkevich, A M. Cuervo, and V V. Verkhusha. 2009, Nature Chemical Biology, Bd. 5, S. 118-126.
27. Lateral mobility in membranes as detected by fluorescence recovery after photobleaching. J. Yguerabide, J a. Schmidt, E E. Yguerabide. 1982, Biophysical Journal, Bd. 40, S. 69-75.
28. Energy migration and fluorescence. 1946. Förster, T. 2012, Journal of Biomedical Optics, Bd. 17, S. 011002.
29. Accuracy and precision in quantitative fluorescence microscopy. Waters., J C. 2009, The Journal of Cell Biology, Bd. 185, S. 1135-1148.
30. Fluorescence microscopy. Conchello., J W. Lichtman and J a. 2005, Nature Methods, Bd. 2, S. 910-915.
31. Lakowicz., J R. Principles of Fluorescence Spectroscopy. Boston : Springer US, 2006.
32. Lifetime-selective fluorescence imaging using an rf phase sensitive camera. J R. Lakowicz, K W. Berndt. 1991, Review of Scientific Instruments, Bd. 62, S. 1727.
33. Quantitative pH Imaging in Cells Using Confocal Fluorescence Lifetime Imaging Microscopy. R. Sanders, A. Draaijer, H. Gerritsen, P. Houpt, Y. Levine. 1995, Analytical Biochemistry, Bd. 227, S. 302-308.

34. Fluorescence lifetime imaging of intracellular calcium in COS cells using Quin-2. J R. Lakowicz, H. Szmacinski, K. Nowaczyk, W J. Lederer, M S. Kirby, M L. Johnson. 1994, Cell Calcium, Bd. 15, S. 7-27.
35. Fluorescence lifetime imaging of free and protein-bound NADH. J R. Lakowicz, H. Szmacinski, K. Nowaczyk, M L. Johnson. 1992, Proceedings of the National Academy of Sciences, Bd. 89, S. 1271-1275.
36. Monitoring Cellular Metabolism with Fluorescence Lifetime of Reduced Nicotinamide Adenine Dinucleotide. V V. Ghukasyan, F j. Kao. 2009, The Journal of Physical Chemistry C, Bd. 113, S. 11532-11540.
37. Quantitative Comparison of Different Fluorescent Protein Couples for Fast FRET-FLIM Acquisition. S. Padilla-Parra, N. Auduge, H. Lalucque, J C. Mevel, M. Coppey-Moisan, M. Tramier. 2009, Biophysical Journal, Bd. 97, S. 2368–2376.
38. Active cytoskeletal force and chromatin condensation independently modulate intranuclear network fluctuations. ST. Spagnol, KN. Dahl. 2014, The Royal Society of Chemistry, Bd. 6, S. 523-531.
39. A. Periasamy, RM. Clegg. FLIM Microscopy in Biology and Medicine. Boca Raton: Chapman and Hall/CRC, 2009.
40. The potential of optical proteomic technologies to individualize prognosis and guide rational treatment for cancer patients. MT. Kelleher, G. Fruhwirth, G. Patel, E. Ofo, F. Festy, PR. Barber, SM. Ameer-Beg, B. Vojnovic, C. Gillett, A. Coolen, G Kéri, PA. Ellis, T. Ng. 2009, Targeted Oncology, Bd. 4, S. 235–252.
41. Applying fluorescence lifetime imaging microscopy to evaluate the efficacy of anticancer drugs. S. Kawanabe, Y. Araki, T. Uchimura, I. Imasaka. 2015, Methods and applications in Fluorescence, Bd. 3, S. 025006.
42. Rapid diagnosis and intraoperative margin assessment of human lung cancer with fluorescence lifetime imaging microscopy. M. Wang, T. Tang, X. Pan, L. Yao, X. Wang, Y. Jing, J. Ma, G. Wang, L. Mi. 2017, BBA Clinical, Bd. 8, S. 7-13.
43. Fluorescence lifetime imaging microscopy in life sciences. JW. Borst, A. Visser. 2010, Measurement Science and Technology, Bd. 21, S. 102002.
44. Alpen, E L. Radiation Biophysics. San Diego: Academic Press, 1990.
45. Effects of Ion Radiation on Cells and Tissues. Scholz, M. 2003, Advances in Polymer Science, Bd. 162, S. 97-155.
46. Chromatin higher-order structure and dynamics. C L. Woodcock, R P. Ghosh. 2010, Cold Spring Harbor Perspectives in Biology, Bd. 2, S. a000760.
47. Chromatin dynamics and the repair of DNA double strand breaks. Y. Xu, B D. Price. 2011, Cell Cycle, Bd. 10, S. 261-267.
48. The Biology of Chromatin Remodeling Complexes. . C R. Clapier, BR. Cairns. 2009, The Annual Review of Biochemistry, Bd. 78, S. 273–304.
49. Megabase chromatin domains involved in DNA double-strand breaks in vivo. E P. Rogakou, C. Boon, C. Redon, W M. Bonner. 1999, The Journal of Cell Biology, Bd. 146, S. 905-9016.
50. Radiation-Induced HPRT Mutations Resulting from Misrejoined DNA Double-Strand Breaks. K. Rothkamm, K. Gunasekara, S A. Warda, A. Krempler, M. Löbrich. 2008, Radiation Research Society, Bd. 169, S. 639–648.
51. Repairing DNA damage in chromatin. A M. Gontijo, C M. Green, G. Almouzni. 2003, Biochemie, Bd. 85, S. 1133-1147.

52. Upgrading the GSI beamline microscope with a confocal fluorescence lifetime scanner to monitor charged particle induced chromatin decondensation in living cells. E. Abdollahi, G. Taucher-Scholz, M. Durante, B. Jakob. 2015, Nuclear Instruments and Methods in Physics Research B, Bd. 365, S. 626-630.

53. Fluorescence lifetime imaging (FLIM): Basic concepts and some recent developments. K. Suhling, L M. Hirvonen, J M. Levitt, P H. Chung, C. Tregidgo, A. Le Marois, D. Rusakov, K. Zheng, S. Ameer-Beg, S. Poland, S. Coelho, R. Henderson, N. Krstajic. 2015, Medical Photonics, Bd. 27, S. 3-40.

54. Kubistscheck., U. Fluorescence Microscopy: From Principles to Biological Applications. Weinheim: Wiley-Blackwell, 2013.

55. Advanced Fluorescence Microscopy Techniques—FRAP, FLIP, FLAP, FRET and FLIM. H C. Ishikawa-Ankerhold, R. Ankerhold, G P C. Drummen. 2012, Molecules, Bd. 17, S. 4047-4132.

56. Fluorescence lifetime imaging – techniques and applications. Becher, W. 2012, Journal of Microscopy, Bd. 247, S. 119–136.

57. Fluorescence-lifetime imaging techniques for microscopy. C Y. Dong, T. French, P T. So, C. Buehler, K M. Berland, E. Gratton. 2003, in Methods in Cell Biology, Bd. 72, S. 431-464.

58. Molecular rotor measures viscosity of live cells via fluorescence lifetime imaging. M K. Kuimova, G. Yahioglu, J a. Levitt, K. Suhling. 2008, Journal of the American Chemical Society, Bd. 2008, S. 6672-6673.

59. Temperature dependence of fluorescence lifetimes of trans-stilbene. M. Sumitani, N. Nakashima. 1977, Chemical Physics Letters, Bd. 5, S. 183-185.

60. Intracellular temperature mapping with a fluorescent polymeric thermometer and fluorescence lifetime imaging microscopy. K. Okabe, N. Inada, C. Gota, Y. Harada, T. Funatsu, S. Uchiyama. 2012, Nature Communications, Bd. 3, S. 705.

61. Sulforhodamine Nanothermometer for Multiparametric Fluorescence Lifetime Imaging Microscopy. J. Jenkins, S M. Borisov, D B. Papkovsky, R I. Dmitriev. 2016, Analytical Chemistry, Bd. 88, S. 10566−10572.

62. A FRET-Based Calcium Biosensor with Fast Signal Kinetics and High Fluorescence Change. M. Mank, D F. Reiff, N. Heim, M W. Friedrich, A. Borst, O. Griesbeck. 2006, Biophysical Journa, Bd. 90, S. 1790−1796.

63. Fluorescence lifetime imaging microscopy: spatial resolution. . P. Bastiaens, A. Squire. 1999, Trends in Cell Biology, Bd. 9, S. 48-52.

64. In vivo multiphoton microscopy of NADH and FAD redox states, fluorescence lifetimes, and cellular morphology in precancerous epithelia. M C. Skala, K M. Riching, A. Gendron-Fitzpatrick, J. Eickho, K W. Eliceiri, J G. White, and N. Ramanujam. 2007, Proceedings of the National Academy of Sciences, Bd. 104, S. 19494-19499.

65. Use of Fluorescence Lifetime Imaging Microscopy (FLIM) as a Timer of Cell Cycle S Phase. I A. Okkelman, R I. Dmitriev, T. Foley, D B. Papkovsky. 2016, PLoS ONE, Bd. 11, S. e0167385.

66. The use of DAPI fluorescence lifetime imaging for investigating chromatin condensation in human chromosomes. A K. Estandarte, S. Botchway, C. Lynch, M. Yusuf, I. Robinson. 2016, Nature Scientific Reports, Bd. 6, S. 31417.

67. Fluorescence Lifetime Imaging Microscopy (FLIM). E B. van Munster, T W J. Gadella. 2005, Advances in biochemical engineering/ biotechnology, Bd. 95, S. 143–175.

68. B. Herman, V E C. Frohlich, J R. Lakowicz, T J. Fellers, M W. Davidson. Fluorescence Resonance Energy Transfer (FRET) Microscopy. [Online] Microscopy Resource Center, 2012. [Zitat vom: 07. 05 2017.] http://www.olympusmicro.com.

69. A Guide to Fluorescent Protein FRET Pairs. B T. Bajar, E S. Wang, S. Zhang, M Z. Lin, J. Chu. 2016, Sensors, Bd. 16, S. 1488.

70. Protein folding studied by single-molecule FRET. B. Schüler, W A. Eaton. 2008, Current Opinion in Structural Biology, Bd. 18, S. 016-026.

71. Fluorescence resonance energy transfer microscopy as demonstrated by measuring the activation of the serine/threonine kinase Akt. J A. Broussard, B. Rappaz, D J. Webb, C M. Brown. 2013, Nature Protocols, Bd. 8, S. 265-281.

72. Instruments, Lamber. Frequency-Domain FLIM for Beginners. [Online] Lamber Instruments. [Zitat vom: 01. 07 2017.] http:// www.lambertinstruments.com.

73. Innovating lifetime microscopy: a compact and simple tool for life sciences, screening, and diagnostics. Esposito, A., et al., et al. s.l. : Journal of Biomedical Optics, 2006, Bd. 11.

74. Fluorescence resonance energy transfer determinations using multiphoton fluorescence lifetime imaging microscopy to characterize amyloid-beta plaques. B J. Bacskai, J. Skoch, G A. Hickey, R. Allen, B T. Hyman. 2003, Journal of Biomedical Optics, Bd. 8, S. 368–375.

75. Quantitative analysis of chromatin compaction in living cells using FLIM–FRET. D. Llères, J. James, S. Swift, D J. Norman, A I. Lamond. 2009, The Journal of Cell Biology, Bd. 187, S. 481–496.

76. Quantitative FLIM-FRET Microscopy to Monitor Nanoscale Chromatin Compaction In Vivo Reveals Structural Roles of Condensin Complexes. D. Llères, A P. Bailly, A. Perrin, D G. Norman, D P. Xirodimas, R. Feil. 2017, Cell Reports, Bd. 18, S. 1791–1803.

77. Fluorescence Lifetime Imaging by Time-Correlated Single-Photon Counting. W. Becker, A. Bergmann, M A. Hink, K. König, K. Benndorf, C. Biskup. 2004, Microscopy Research and Technique, Bd. 63, S. 58–66.

78. Fluorescence lifetime imaging by multi-dimensional time correlated single photon counting. Becker, W. 2015, Medical Photonics, Bd. 27, S. 41—61.

79. Live Cell Imaging of Heavy-Ion-Induced Radiation Responses by Beamline Microscopy. Jakob, B., et al., et al. s.l. : Radiation Research, 2005, Bd. 163.

80. Histone Deacetylase Inhibitor and Demethylating Agent Chromatin Compaction and the Radiation Response by Cancer Cells. G. Bar-Sela, K M. Jacobs, D. Gius. 2007, The Cancer Journal, Bd. 13, S. 1.

81. Changes in Chromatin Structure in NIH 3T3 Cells Induced by Valproic Acid and Trichostatin A. M B. Felisbino, M S V. Gatti, M L S. Mello,. 2014, Journal of Cellular Biochemistry, Bd. 115, S. 1937–1947.

82. Real-Time Imaging of Histone H4K12–Specific Acetylation Determines the Modes of Action of Histone Deacetylase and Bromodomain Inhibitors. T. Ito, T. Umehara, K. Sasaki, Y. Nakamura, N. Nishino, T. Terada, M. Shirouzu, B. Padmanabhan, S. Yokoyama, A. Ito, M. Yoshida. 2011, Chemistry and Biology, Bd. 18, S. 495–507.

83. Trichostatin-A induces differential changes in histone protein dynamics and expression in HeLa cells. J. Rao, D. Bhattacharya, B. Banerjee, A. Sarin, GV. Shivashankar. 2007, Biochemical and Biophysical Research Communications, Bd. 363, S. 263–268.

84. Syto dyes and histoproteins-myriad of applications. Tarnok, A. 2008, International Society for Advancement of Cytometry, Bd. 73A, S. 477-479.

85. BENA435, a new cell-permeant photoactivated green fluorescent DNA probe. A. Erve, Y. Saoudi, S. Thirot, C. Guetta-Landras, J-C. Florent, C-H. Nguyen, D S. Grierson, A V. Popov. 2006, Nucleic Acids Research, Bd. 34, S. e43.

86. Violet Laser Diodes as Light Sources for Cytometry. H M. Shapiro, N G. Perlmutter. 2001, Cytometry, Bd. 44, S. 133–136.

87. SiR–Hoechst is a far-red DNA stain for live-cell nanoscopy. G. Lukinavicius, C. Blaukopf, E. Pershagen, A. Schena, L. Reymond, E. Derivery, M. Gonzalez-Gaitan, E. D'Este, S W. Hell, D W. Gerlich, K. Johnsson. 2015, Nature Communications, Bd. 6, S. 8497.

88. A new minor groove binding asymmetric cyanine reporter dye for real-time PCR. M. Bengtsson, H J. Karlsson, G. Westman, M. Kubista. 2003, Nucleic Acids Research, Bd. 31, S. e45.

89. Development of organic dye-dopped silica nanoparticles in a reverse microemulsion. X. Zhoa, R P. Bagwe, W. Tan. 2004, Advanced Materials, Bd. 16, S. 173-176.

90. Highly bright and photostable cyanine dye-doped silica nanoparticles for optical imaging: Photophysical characterization and cell tests. I. Miletto, A. Gilardino, P. Zamburlin, S. Dalmazzo, D. Lovisolo, G. Caputo, G. Viscardi, G. Martra. 2010, Dyes and Pigments, Bd. 84, S. 121–127.

91. E. Abdollahi, N. Özgün-Korkusuz, M. Durante, G. Taucher-Scholz, B. Jakob1. Detection of chromatin decondensation induced by charged particle irradiation using Fluorescence Lifetime Imaging Microscopy. Darmstadt : GSI Scientific Report, 2014.

92. Comparison of the repair of potentially lethal damage after low- and high-LET radiation exposure, assessed from the kinetics and fidelity of chromosome rejoining in normal human fibroblasts. C. Lio, T.Kawata, G. Zhou, Y. Furusawa, R. Kota, A. Kumabe, S. Sutani, J. Fukada, M. Mishima, N. Shigematsu, K. George, F. Cucinotta. 2013, Journal of Radiation Research, Bd. 54, S. 989–997.

93. Enhanced fidelity for rejoining radiation-induced DNA double-strand breaks in the G2 phase of Chinese hamster ovary cells. I. Krüger, k. Rothkamm, M. Löbrich. 2004, Nucleic Acids Research, Bd. 32, S. 2677-2684.

94. Epigenetic Reprogramming in Cancer. M L. Suvà, R. Riggi, B E. Bernstein. 2013, Science, Bd. 339, S. 6127.

95. Studies in Heterochromatin DNA: Accessibility of Late Replicating Heterochromatin DNA in Chromatin to Micrococcal Nuclease Digestion. M T, Kuo. 1979, Chromosoma, Bd. 70, S. 183 - 194.

96. HAT2 mediates histone H4K4 acetylation and affects micrococcal nuclease sensitivity of chromatin in Leishmania donovani. P K. Jha, M. Imran Khan, A. Mishra, P. Das, K K. Sinha. 2017, PLoS ONE, Bd. 15, S. e0177372.

97. Chromatin condensation and sensitivity of DNA in situ to denaturation during cell cycle and apoptosis - a confocal microscopy study. J. Dobrucki, Z. Darzynkiewicz. 2001, Micron, Bd. 32, S. 645-652.

98. Chromatin condensation modulates access and binding of nuclear proteins. R M. Martin, M C. Cardoso. 2010, The FASEB Journal, Bd. 24, S. 1066-1072.

99. Modulation of Higher Order Chromatin Conformation in Mammalian Cell Nuclei Can Be Mediated by Polyamines and Divalent Cations. A. Visvanathan, K. Ahmed, L. Even-Faitelson, D. Lleres, D P. Bazett-Jones,A I. Lamond. 2013, PLoS ONE, Bd. 8, S. e67689.

100. Spatially Resolved Quantification of Chromatin Condensation through Differential Local Rheology in Cell Nuclei Fluorescence Lifetime Imaging. S T. Spagnol, K N. Dahl. 2016, PLoS ONE, Bd. 11, S. e0146244.

101. Influence of Chromatin Structure on the Induction of DNA Double Strand Breaks by Ionizing Radiation. M C. Elia, M O. Bradley. 1992, Cancer Research, Bd. 52, S. 1580-1586.

102. Variationi n Radiation-InducedF ormationo f DNA Double-StrandB reaks as a Functiono f ChromatiSnt ructure. R L, Warters, B W. Lyons. 1992, Radiation Research, Bd. 130, S. 309-318.

103. Chromatin Structure and Radiation-induced DNA Strand Breaks in Human Cells: Soluble Scavengers and DNA-bound Proteins Offer a Better Protection Against Single- than Double-strand Breaks. J. Nygren, M. Ljungman, M. Ahnström. 1995, International Journal of Radiation Biology, Bd. 68, S. 11-18.

104. Chromatin Compaction Protects Genomic DNA from Radiation Damage. H. Takata, T. Hanafusa, T. Mori, M. Shimura, Y. Iida. K. Ishikawa, K. Yoshikawa, Y. Yoshikawa, K. Maeshima. 2013, PLoS ONE, Bd. 8, S. e75622.

105. Changes in chromatin structure and mobility in living cells at sites of DNA double-strand breaks. M J. Kruhlak, A. Celeste, G. Dellaire, O. Fernandez-Capetillo, W G. Müller, J G. McNally, D P. Bazett-Jones, A. Nussenzweig. 2006, The Journal of Cell Biology, Bd. 172, S. 823–834.

106. Poly(ADP-ribosyl)ation-dependent Transient Chromatin Decondensation and Histone Displacement following Laser Microirradiation. H. Strickfaden, D. McDonald, M J. Kruhlak, J-F Haince, J P H. Th'ng,M. Rouleau, T. Ishibashi, G N. Corry, J. Ausio, D A. Underhill, G G. Poirier, M J. Hendzel. 2016, Journal of Biological Chemistry, Bd. 291, S. 1789–1802.

107. Dynamics of DNA Double-Strand Breaks Revealed by Clustering of Damaged Chromosome Domains. J A. Aten, J. Stap, P M. Krawczyk, C H. van Oven, R A. Hoebe, J. Essers, R. Kanaar. 2004, Science, Bd. 303, S. 92.

108. Chromatin dynamics during DSB repair. M. Falk, E. Lukasova, B. Gabrielova, V. Ondrej, S. Kozubek,. 2007, Biochimica et Biophysica Acta, Bd. 1773, S. 1534–1545.

109. Radiation Induced Chromatin Conformation Changes Analysed by Fluorescent Localization Microscopy, Statistical Physics, and Graph Theory. Y. Zhang, G. Máté, P. Müller, S. Hillebrandt, M. Krufczik, M. Bach, R. Kaufmann, M. Hausmann, D W. Heermann. 2015, PLoS ONE, Bd. 10, S. e0128555.

110. Discovery of DNA dyes Hoechst 34580 and 33342 as good candidates for inhibiting amyloid beta formation: in silico and in vitro study. N Q. Thai, N-H Tseng, M T. Vu, T T. Nguyen, H Q. Linh, C-K Hu, Y-R Chen,M S Li. 2016, Journal of Computer-Aided Molecular Design, Bd. 30, S. 639–650.

111. Fluorescence Lifetime Imaging Microscope Consisting of a Compact Picosecond Dye Laser and a Gated Charge-Coupled Device Camera for Applications to Living Cells. T. Uchimura, S. Kawanabe, Y. Maeda, T. Imasaka. 2006, Analytical Science, Bd. 22, S. 1291-1295.

112. In Situ Activity of Suspended and Immobilized Microbial Communities as Measured by Fluorescence Lifetime Imaging. P. Walczysko, U. Kuhlicke,S. Knappe,C. Cordes, T R. Neu. 2008, Applied and Enviornmental Microbiology, Bd. 74, S. 294–299.

113. Effects of chromatin decondensation on alternative NHEJ. Moscariello, M. und Iliakis, G. s.l. : DNA Repair, 2013, Bd. 12.

114. Molecular crowding affects diffusion and binding of nuclear proteins in heterochromatin and reveals the fractal organization of chromatin. A L. Bancaud, S. Huet, N. Daigle, J. Mozziconacci, J. Beaudouin, J.Ellenberg. 2009, The EMBO Journal, Bd. 28, S. 3785-3798.

115. Relationship between Absorption Intensity and Fluorescence Lifetime of Molecules. Strickler, S J. und Berg, R A. s.l. : The Journal of Chemical Physics, 1998, Bd. 98.

116. Quantitative fluorescence lifetime spectroscopy in turbid media: comparison of theoretical, experimental and computational methods. Vishwana, K. und Pogue, B. s.l. : Physics in Medicine and Biology, 2002, Bd. 47.

117. Fluorescence Quantum Yields and Their Relation to Lifetimes of Rhodamine 6G and Fluorescein in Nine Solvents: Improved Absolute Standards for Quantum Yields. Magde, D., Wong, R. und Seybold, P G. 4, s.l. : Photochemistry and Photobiology, 2002, Bd. 75.

118. Use of a fluorescence lifetime imaging microscope in an apoptosis assay of Ewing's sarcoma cells with a vital fluorescent probe. X. Li, T. Uchimura, S. Kawanabe. 2007, Analytical Biochemistry, Bd. 367, S. 219–224.

119. The Heterochromatic Barrier to DNA Double Strand Break Repair: How to Get the Entry Visa. A A. Goodarzi, P A. Jeggo. 2012, International Journal of Molecular Sciences, Bd. 13, S. 11844-11860.

120. Combining Low Temperature Fluorescence DNA-Hybridization, Immunostaining, and Super-Resolution Localization Microscopy for Nano-Structure Analysis of ALU Elements and Their Influence on Chromatin Structure. M. Krufczik, A. Sievers, A. Hausmann, J-H Lee. 2017, International Journal of Molecular Sciences, Bd. 18, S. 1005-1021.

121. A review of dsb induction data for varying quality radiations. K M. Prise, G. Ahnstroem, M. Belli, J. Carlsson, D. Frankenberg, J. Kiefer, M. Löbrich, B D. Michael, J. Nygren, G. Simone. 1998, International Journal of Radiation Biology, Bd. 74, S. 173-184.

122. Histone deacetylases and their inhibitors in cancer, neurological diseases and immune disorders. J K. Falkenberg, R W. Johnstone. 2014, Nature Reviews Drug Discovery, Bd. 13, S. 673–691.

123. Argolight. Description-Patterns customization. [Online] Argolight. [Zitat vom: 01. 07 2017.] http://argolight.com.

124. Fluorescent microspheres for calibrating microscopes and flow cytometers. [Online] Thermo Fisher Scientific . [Zitat vom: 15. 06 2017.] www.thermofisher.com.

Acknowlegement

Foremost, I would like to express my sincere gratitude to my principle reviewer, Professor Marco Durante for giving me the opportunity to work with such an interesting project. My especial appreciation and thanks go to my supervisor Dr. Burkhard Jakob for his countinous encouragements, supports, advices, insights and fruitful discussions during these years. I appriciate his patience during my graduation. Besides, I place on record, my sense of gratitude to Professor Gisela Taucher-Scholz to give me the opportunity to grow as researcher in her group.

I am very thankful to Dr. Michael Scholz for his valuable scientific comments during my Grk-PhD meetings. Sincere gratitude to all the staff in the biophysics department especially molecular radiobiology and imaging group. I would like to thank Dr. Kay-Obbe Voss as well as Rayees Khan. My special thanks also go to dear Tatyana Syzonenko and Dr. Anja Heselich not only for scientific discussions but also their kindness and understanding. I also would like to thanks Nadine Erbeldinger for the fruitful discussions.

I would like to thanks DFG-GrK for funding support and giving me the chance of being a scholar of radiation biology graduate college 1657.

I am especially thankful to my dear friends, Maria Diddona-Schnellbächer, Roland Schnellbächer, Vanessa Schnellbächer and Ornella Schnellbächer who play the role of my family in Germany. I am also warmly appreciative of Amir Mofidi for his helps, supports and many enjoyble memories that he made for me.

And last but not least, my special appreciation goes to my family: mom, dad, my brothers, Amir and Arman and my sister, Afrouz for encouragement and supporting me spiritually in whatever I pursue. Without you, it would all be pointless.

Curriculum Vitae Elham Abdollahi Mirzanagh

Personal details	
Date of Birth	1st. April 1978
Place of Birth	London
Nationality	Iranian

Education	
Since 2014	PhD student, Physics department atTechnical University of Darmstadt, Darmstadt, Germany Advisors: Prof. Marco Durante, Prof. Barbara Drossel • Research for the PhD in Biophysics division at GSI Helmholzzentrum für Schwerionenforschung GmbH
2011- 2014	MSc Physics, Physics department at Umeå University, Umeå, Sweden Advisor: Prof. Ove Axner
1997-2002	BSc Physics, in Physics department at Uromiyeh University, Uromiye, Iran
1992-1996	Mathematics and Physics, Ghods High School, Tehran, Iran

Achievments	
2016	First poster awarded by DPG/ENTRIA physics school
2014	Awarded with the scholarship for PhD study by DFG-funded Graduate collage 1657
2013	Travel award for SPIE symposium by SPIE

Working expeience	
2003-2009	Senior Technician, Department of production, Fan Azarakhsh Co. (Medical Device-Hearing Aids), Tehran, Iran Tasks: Supervisor of in the ear hearing air team Production, Analysis, and repair of hearing instrument Responsible for Risk Management System